

Dissertation
submitted to the
Combined Faculties of the Natural Sciences and Mathematics
of the Ruperto-Carola-University of Heidelberg, Germany
for the degree of
Doctor of Natural Sciences

Put forward by
Giulia Vannoni
born in: Florence, Italy
Oral examination: 27th November, 2008

Diffusive Shock Acceleration in Radiation Dominated Environments

Referees:

Prof. Dr. Werner Hofmann

Prof. Dr. Felix Aharonian

Abstract

In this work I describe a numerical method developed, for the first time, for the study of Diffusive Shock Acceleration in astrophysical environments where the radiation pressure dominates over the magnetic pressure. This work is motivated by the overwhelming evidence of the acceleration of particles to high energy in astrophysical objects, traced by the non-thermal radiation they emit due to interactions with the gas, radiation fields and magnetic fields. The main objective of this work is to create a generic framework to study self-consistently the interaction of acceleration at shocks and radiative energy losses and the effect such an interplay has on the particle spectrum and on the radiation they emit, in the case when energy losses determine the maximum achievable energy. I apply the developed method to electrons accelerated in three different types of sources: a Supernova Remnant in the Galactic Centre region, a microquasar, and a galaxy cluster. In all three cases the energy losses due to the interaction of electrons with radiation dominate over synchrotron cooling. I demonstrate that there is a strong impact due to the changing features of the inverse Compton scattering from the Thomson to the Klein-Nishina regime, on both the spectrum of accelerated electrons and their broadband emission. I also consider proton acceleration in galaxy clusters, where the particles lose energy during acceleration due to the interaction with the Cosmic Microwave Background radiation. The secondary products from pair production and photomeson processes interact with the same photon field and the background magnetic field, producing broadband electromagnetic radiation from radio to gamma-rays.

Kurzfassung

In dieser Arbeit wird eine numerische Methode zur Berechnung der diffusen Schockbeschleunigung in astrophysikalischen Objekten vorgestellt. Dabei werden zum ersten Mal Umgebungen betrachtet, in denen der Strahlungsdruck über den magnetischen Druck dominiert. Dies ist motiviert durch zahlreiche Hinweise auf Beschleunigung von Teilchen zu den höchsten Energien in Objekten mit starken Strahlungsfeldern: hochenergetische Teilchen reagieren mit Gas, Strahlungsfeldern und magnetischen Feldern und senden nicht-thermische elektromagnetische Strahlung aus. Der Schwerpunkt dieser Arbeit ist die selbstkonsistente Beschreibung der Wechselwirkung zwischen Schockbeschleunigung und Strahlungsverlusten für den Fall, dass der Energieverlust der Teilchen die maximal erreichbare Energie bestimmt. Insbesondere der Einfluss dieser Wechselwirkung auf das Teilchen- und Strahlungsspektrum werden betrachtet. Die entwickelte Methode wird auf die Elektronenbeschleunigung in drei verschiedenen Quelltypen angewandt: Supernova Überreste im galaktischen Zentrum, Mikroquasare und Galaxienhaufen. In allen drei Quelltypen ist der Energieverlust der Elektronen dominiert durch die Wechselwirkung von Elektronen mit anderen Strahlungsfeldern, nicht durch Synchrotronstrahlungsverluste. Es wird gezeigt, dass die Änderung der inversen Compton-Streuung beim Wechsel vom Thompson in das Klein-Nishina Regime einen starken Einfluss sowohl auf die beschleunigten Elektronen als auch das emittierte Photonenspektrum hat. Desweiteren wird die Beschleunigung von Protonen in Galaxienhaufen betrachtet, bei der die Protonen Energie durch Wechselwirkung mit den Photonen der kosmischen Hintergrundstrahlung verlieren. Die sekundären Teilchen, erzeugt durch Paarproduktion und Photon-Meson-Prozessen, interagieren mit den selben Photonenfeldern und dem magnetischen Hintergrundfeld und erzeugen eine Strahlungsspektrum vom Radio-Bereich bis zur γ -Strahlung.

“Now it’s closing time . . .”

Contents

Introduction	I
1 The Observational Framework	1
1.1 High Energy Particles and Non-thermal Radiation	1
1.2 Supernova Remnants	7
1.3 Microquasars	9
1.4 Clusters of Galaxies	10
2 Diffusive Shock Acceleration	13
2.1 Plasma Equations	13
2.2 Collisionless Shock Waves	18
2.3 Diffusive Shock Acceleration	23
2.3.1 The Bell Approach	25
2.3.2 The Transport Equation	29
2.4 The Maximum Energy	32
3 DSA in Presence of Energy Losses	37
3.1 Electromagnetic Interactions	38
3.2 Proton-photon Interactions	44
3.3 Including Energy Losses in DSA, the Status of the Art	48
4 The Model	53
4.1 The Numerical Method	54

5	Electron Acceleration Under Dominant IC Losses	59
5.1	Photon Spectra	60
5.2	Results	61
5.3	Applications	66
5.3.1	SNR in the Galactic Centre	66
5.3.2	Microquasars	71
5.3.3	Clusters of Galaxies	74
6	Proton Acceleration in Galaxy Clusters	79
6.1	Primary and Secondary Particle Spectra	81
6.2	Radiation spectra	86
7	Conclusions	89
A	Appendix	93
	Bibliography	I

Introduction

The presence of suprathermal high energy particles is observed in a huge variety of astrophysical objects, from Galactic sources like Supernova Remnants, binary systems or pulsar nebulae, to active galaxies and large structures like clusters of galaxies. They are traced via the non-thermal radiation they emit in the interaction with the gas and the photon and magnetic fields.

In order to explain the observed suprathermal distributions of particles, several acceleration mechanisms have been proposed. One of the major, widely accepted and theoretically well developed is Diffusive Shock Acceleration (DSA) (Axford et al., 1977; Krymsky, 1977; Bell, 1978; Blandford & Ostriker, 1978). In the framework of this model, charged particles are accelerated by repeatedly crossing a collisionless shock in the presence of magnetic turbulence. Remarkably, the spectrum generated by such a mechanism is a power law whose spectral index value is basically independent of all the details of the system like the velocity of the shock (provided that we deal with a strong shock, i.e. Mach number $\gtrsim 10$), the value of the magnetic field and the details of diffusion and of injection in the accelerator. The maximum energy particles can achieve, on the other hand, is strongly sensitive to the specific radiative and non radiative mechanisms which limit acceleration (e.g. Hillas, 1984; Lagage & Cesarsky, 1983b). Therefore, the cut-off energy of the spectrum of both particles and radiation and the spectral shape around that energy carry precious information on the acceleration mechanism as well as on the characteristics of the environment it occurs in (an overview of DSA and the problem of the maximum energy is given in Chapter 2). In this respect, non-thermal radiation not only represents the way to identify the sources of high energy particles, but it is also a probe of the specific

characteristics of the acceleration process and the source environment.

In the present work we are interested in the case where radiative energy losses limit the acceleration. In this scenario, the two processes (acceleration and energy losses) have to be included in a self-consistent model in order to correctly evaluate the effect they have on the spectrum of high energy particles and consequently on the radiation they emit. An accurate description is crucial when trying to interpret observations and get an insight on the actual physics that acts in different objects.

Several approaches to the problem of particles acceleration at shocks in the presence of radiative losses can be found in the literature (Bulanov & Dogiel, 1979; Webb et al., 1984; Heavens & Meisenheimer, 1987; Zirakashvili & Aharonian, 2007), and we briefly present them, together with some details on energy loss mechanisms, in Chapter 3. However, they all deal with the specific case of synchrotron cooling of electrons. In this work we present a numerical method that takes into account the presence of energy losses in the framework of DSA in a self-consistent and general fashion. The species of particles involved, the type of losses and the energy and spatial dependence of the diffusion coefficient can be chosen to be of any kind. Moreover, the calculation is time dependent.

In particular, we apply our method to the case, never studied in detail before, of acceleration taking place in a radiation dominated environment (i.e. where the photon energy density is much bigger than the magnetic one). In the case of electrons, this implies a predominance of inverse Compton (IC) losses over synchrotron ones. Interestingly, for high energy particles the scattering process enters the Klein-Nishina (KN) regime where the shape of the cross-section differs considerably from the simple Thomson one appropriate for synchrotron losses. In this case, the shape of the energy losses is complex and the modification it produces on the simple power law acceleration spectrum requires an accurate calculation. We demonstrate that the inverse Compton losses of electrons, in the Klein-Nishina regime, lead to spectra of ultra-relativistic electrons which may significantly differ from the classical Diffusive Shock Acceleration solution in the Thomson regime. The most prominent feature is the appearance of a pronounced pile up in the spectrum around the cut-off energy. When looking at the radiation emitted by the particles, the pile up feature is

reproduced in the synchrotron distribution, which no longer follows a simple power law below the cut-off, as in the case of dominant Thomson losses. On the other hand, the hardening in the electron spectrum is barely visible in the IC spectrum since the effect of the KN cross-section on the scattering process itself compensates the opposite action on the electron spectrum (Vannoni et al., 2008).

Our calculation has a value *per se*, since such a general and self-consistent approach had never been tried before and the results could not be anticipated on the basis of general arguments. But the interest is not purely academic. As we will show, our method can be applied to a variety of environments where shocks are present and the radiation energy density exceeds that of the magnetic field, such as Supernova Remnants (SNR) in regions of enhanced radiation density like the inner Galactic Centre, binary systems in which particles are accelerated in the intense photon field of a bright star, and extended systems like clusters of galaxies where the dominant energy loss channel for electrons is represented by the interaction with the Cosmic Microwave Background (CMB) radiation.

This last class of objects is very interesting also from another point of view: the dimensions of the system are such that high energy protons are confined in their volume for cosmological times (Völk et al., 1996; Berezhinsky et al., 1997). Due to this special feature galaxy clusters are suitable sources for very high energy protons (e.g. Hillas, 1984). At the outer boundary of the system, shock waves can form between the hot cluster gas and the cold external material falling onto the structure. Such accretion shocks are, in principle, able to accelerate particles for the cluster lifetime that is estimated to be of the order of the Hubble time. If this is the case, then the energy losses induced by the presence of the CMB radiation via pair and pion production have time scales shorter than the accelerator lifetime and become the limiting mechanism for proton acceleration (Norman et al., 1995; Kang et al., 1997). In this case we calculate the cut-off energy and the shape of the spectrum at high energies self-consistently and at different epochs and show that the resulting spectrum differs from the simple assumption, usually adopted, of a pure power law distribution with an exponential cut-off. We find that, given realistic values of the magnetic field and the shock velocity, the cut-off is determined by the process of

pair production, while pion production is negligible. The secondary electron and positron spectra are calculated numerically. Once produced, the pairs cool rapidly in the background radiation and magnetic field. We calculate the effect of energy losses on the particle spectrum and derive the broadband radiation emitted via synchrotron and IC, taking into account the effects of the transition of the IC process from the Thomson to the Klein-Nishina regimes (Vannoni et al., in preparation).

The main pieces of observational evidence on the ubiquitous presence of high energy particles and non-thermal radiation in astrophysical objects are presented in Chapter 1. We demonstrate how such evidence favour DSA in many cases and introduce the observational support for the presence of shocks based on observations of non-thermal radiation. In Chapter 2 we review collisionless non-relativistic shock waves and the basic characteristics of astrophysical plasmas. We also present the theory of Diffusive Shock Acceleration in its double formulation, the single particle approach (Bell, 1978) and the statistical approach (Blandford & Ostriker, 1978). The last Section is dedicated to the issue of the maximum energy achieved by acceleration. In Chapter 3 we present the physical processes responsible for particle energy losses at acceleration sites, namely synchrotron and inverse Compton radiation for electrons and proton-photon interaction. We will also overview the previous theoretical approaches to the problem of including energy losses in the framework of DSA. Chapter 4 is devoted to present the numerical method developed in this work. The details of the calculation can be found in the Appendix. The main results of this work are presented and discussed in Chapter 5 and 6. Chapter 7 is dedicated to our conclusions.

Chapter 1

The Observational Framework

The presence of high energy particles in the Universe is ubiquitous. We observe them directly at Earth (the so-called Cosmic Rays (CRs)) and in many astrophysical sources by means of the non-thermal radiation they produce in the interaction with the source environment. In this Chapter we briefly overview such observations. We also present the basic characteristics of the three classes of objects to which we apply our calculation in the following: Supernova Remnants, microquasar and clusters of galaxies.

1.1 High Energy Particles and Non-thermal Radiation

One of the most interesting, yet puzzling, features of Cosmic Rays is their energy spectrum. As we can see (Fig. 1.1), it spans over 10 decades in energy, up to energies far beyond any human built accelerator. The spectrum presents two main features around 10^{15} eV and $10^{18.5}$ eV, the so-called knee and ankle, respectively. Below the knee, the particle distribution follows a power law of index $\delta \sim 2.7$. Above the knee, the spectrum steepens and it can be approximated with a power law distribution of index close to 3, up to the ankle where it hardens to $\delta \sim 2.6$. CRs are believed to be of Galactic origin up to energies around the knee and of extragalactic origin in the ultrahigh energy part of the spectrum, above the ankle. There is no consensus on the

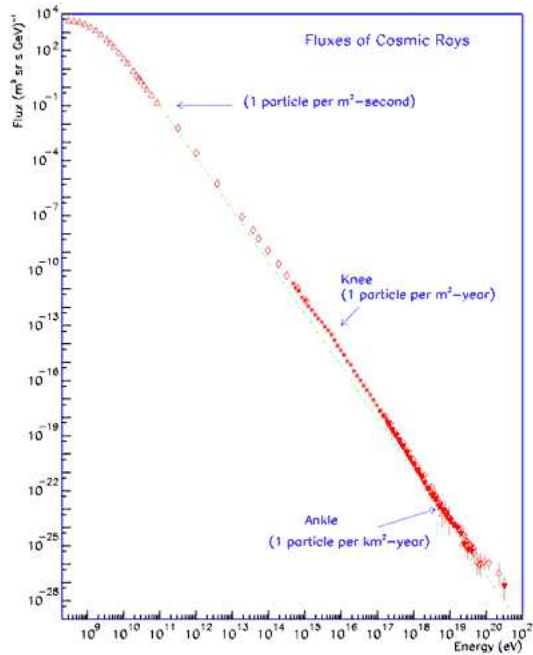


Figure 1.1: Cosmic Ray spectrum. Data compiled by S. P. Swordy as in Swordy (2001).

transition point between the two components and the origin of the particles between 10^{15} eV and $10^{18.5}$ eV is a topic of strong debate. For a detailed treatment we refer to the textbooks by Ginzburg & Syrovatskii (1964); Gaisser (1990); Longair (1997) and Schlickeiser (2002). Here after are reported the observed features, relevant in the framework of this work, of the bulk of the Cosmic Ray distribution, namely between 1 GeV and 10^{15} eV, and their possible interpretation.

From observations on the composition of CRs and on the disintegration that nuclei experience during propagation, together with measurements on radioactive nuclei present in the Cosmic Rays, whose decay acts like an atomic clock, the mean column density transversed by CRs during propagation in the Interstellar Medium (ISM) and the mean residence time in the Galaxy can be evaluated and they result in $X \simeq 7 \text{ g cm}^{-2}$ (at 10 GeV and decreasing with energy) and $\tau_{CR} \sim 10^7$ yr (e.g. Schlickeiser, 2002). From the values of these parameters, much bigger than the corresponding values for rectilinear propagation across the Galaxy, it has been inferred that Cosmic Rays travel in a sort of random walk from the source to the Earth. Such a behaviour is explained with diffusion in the Galactic magnetic field

(see Ginzburg & Syrovatskii, 1964). The current picture of the magnetic field in the Milky Way (we refer to Heiles, 1976; Vallée, 2004, and references therein) is of a large scale ordered component along the spiral arms whose average intensity is estimated between 2 and 4 μG (Widrow, 2002; Kulsrud & Zweibel, 2008). Superimposed to this, a diffuse turbulent component is inferred from the CRs confinement argument. The turbulent field is not easy to measure, but hints of its presence have been found by Armstrong et al., 1995. The idea of an interplay between Cosmic Rays and the ISM is supported by the fact that the different components of the medium, Cosmic Rays, magnetic field and gas, have average energy densities close to equipartition, with a value of $\sim 1 \text{ eV/cm}^3$ (e.g. Gaisser, 1990).

τ_{CR} represents the mean confinement time of Cosmic Rays in the Galaxy and has been found to have a power law dependence on energy $\tau_{CR} \propto E^{-\gamma}$ with $\gamma \simeq 0.6$ (Swordy et al., 1990). In the absence of energy losses during propagation, the variation in time of the distribution of CRs has to be equal to the injection rate of particles in the ISM. One can approximate the continuity equation as:

$$\frac{f(E)}{\tau_{CR}(E)} = Q_{inj}(E), \quad (1.1)$$

where $f(E) \propto E^{-\delta}$, with $\delta \sim 2.6 - 2.7$, is the observed particle spectrum and Q_{inj} is the one at the source, before propagation through the ISM. Thus, it is inferred that the spectrum at the source has to have a power law energy dependence of the kind:

$$Q_{inj} \sim f(E)\tau_{CR}(E) \propto E^{-\alpha}, \quad (1.2)$$

with $\alpha \sim 2 - 2.1$.

To summarise, from direct observations of Cosmic Rays it is deduced that the production spectrum must be a power law in energy of index close to 2 and that this property has to be almost universal among different sources and on a wide range of energies.

Unfortunately, it is not possible to trace the high energy particle sources directly with Cosmic Rays. The deflection of these particles in the background magnetic field is so severe that no information on the initial direction is preserved. Indeed no Cosmic Ray Astronomy is possible, except at the ultrahigh energy end of the

spectrum (where the first, promising indications of anisotropy have started to be collected (Pierre Auger Collaboration, 2007)). Therefore to identify the sources of high energy particles one has to rely on the non-thermal radiation that they produce in the interaction with the source environment via various mechanisms. Since photons do not experience any magnetic deflection and are abundantly produced by high energy particles, they are the best messengers we have to identify and study the sources.

To track the presence of accelerated particles that do not follow a maxwellian distribution of thermal gas, we are interested in those photon distributions that show suprathermal spectral tails. Typically, the energy bands relevant for non-thermal emission are radio, X-rays and gamma-rays, though it can in principle be produced in any energy band. Among the fundamental emission mechanisms, those relevant for the present work are synchrotron and inverse Compton for electrons, and proton-photon interactions for protons. Due to the much bigger mass of protons compared to electrons, electromagnetic emission for protons is negligible in almost all the situations of interest. The details of the emission mechanisms are presented in Chapter 3, for the moment we outline only their main characteristics (all the formulae below can be found e.g. in Rybicki & Lightman, 1979).

Synchrotron radiation traces the presence of electrons in combination with magnetic fields. The power emitted by an electron depends essentially on its energy and on the magnetic energy density, thus carrying information on these two quantities. To first approximation, a particle of energy E emits photons of energy:

$$\epsilon \simeq 20 \times 10^{-6} (E_{TeV})^2 (B_{\mu G}) \text{ keV},$$

$B_{\mu G}$ being the value of the magnetic field in microGauss and E_{TeV} the energy of the electron in TeV. Thus, a power law distribution of particles $E^{-\alpha}$ gives rise to a power law distribution of photons ϵ^{-p} and the two spectral indices are connected by the relation $p = (\alpha - 1)/2$. For accelerated electrons in a typical range between few GeV up to tens of TeV, the synchrotron radiation is emitted at frequencies from radio up to the X-ray band, for magnetic fields in the μG range.

The second process for electrons is inverse Compton scattering, the upscattering

of seed photons to higher energies. Assuming that IC proceeds in the Thomson regime, i.e. $\epsilon E/(mc^2)^2 \ll 1$, where E is the electron energy and ϵ the initial photon energy, the mean final energy of photons is:

$$\epsilon_f \simeq 5 (\epsilon_{meV})(E_{TeV})^2 \text{ GeV},$$

with ϵ_{meV} the initial energy of the photon in units of 10^{-3} eV and E_{TeV} the energy of the electron in TeV. As a rough approximation, we can say that a black body radiates essentially at one energy, corresponding to the peak of the planckian distribution: $\langle \epsilon \rangle = 2.7k_B T$, $k_B = 8.62 \times 10^{-5}$ eV K $^{-1}$ being the Boltzmann constant and T the temperature of the black body. To have an estimate, we can consider the CMB, the lowest temperature black body distribution present in the universe: $\langle \epsilon \rangle_{CMB} \simeq 6 \times 10^{-4}$ eV. When IC losses occur in the Thomson regime, a power law distribution of electrons is reproduced in a power law distribution of photons, similarly to the case of synchrotron cooling. But when the process enters the so-called Klein-Nishina regime ($\epsilon E/(mc^2)^2 \gtrsim 1$), a non power law behaviour appears in the radiation spectrum.

High energy protons can lose energy, in interactions either with the surrounding matter or seed photons, via pair and pion production. While neutral pions decay into two gammas, the decay of charged pions creates a population of secondary electrons. These electrons, together with the pairs directly produced by protons, can in turn emit via synchrotron or IC processes. While radio and X-ray observations reveal the presence of high energy electrons, either primary electrons or secondary from hadronic processes, and can be firmly attributed to electromagnetic processes (synchrotron and IC), gamma-ray observations can be often explained equally well via direct pion decay or IC emission of very high energy electrons.

Non-thermal radiation, and consequently high energy particles, are observed in a great variety of objects, from local sources like Supernova Remnants, pulsar nebulae and binary systems, to Active Galactic Nuclei, Mpc extended structures like galaxy clusters or cosmological extremely powerful explosions like Gamma-ray Busts. When trying to interpret such overwhelming evidence, one of the most important questions that arise is the nature of the mechanisms responsible for accelerating particles ef-

ficiently and with the observed characteristics. One of the most successful models is Diffusive Shock Acceleration. In the presence of a shock wave in a magnetised plasma, charged particles are accelerated by repeatedly bouncing off magnetic turbulence, back and forth across the shock. The wide applicability of DSA is due to three main characteristics: the resulting distribution of particles follows a power law of index ~ 2 in energy, close to the value needed to explain the inferred source spectrum of Cosmic Rays (Eq. (1.2)); the value of the spectral index is almost independent on the characteristics of the environment the shock develops in; and shock waves are observed in a large number of sources in correspondence with non-thermal radiation. One of the first evidences of the feasibility of shock acceleration mechanism was obtained in the local environment of the Solar system by satellite measurements at the Earth bow shock. Such a structure forms when the supersonic Solar wind hits the Earth magnetosphere. *In situ* measurements provide us with the direct evidence of the existence of astrophysical collisionless shocks (Ness et al., 1964) and of their capability of accelerating particles (Lee (1982) and references therein). Shock structures have been detected in the most diverse objects. In SNR there is little doubt that the strong non-thermal emission is spatially associated with the external and reverse shocks of the expanding shell (see next Section). But X-ray observations have addressed the presence of shock-like structures also in the interior of galaxy clusters, due to merger events (Forman et al., 2002) and numerical simulations have pointed out that strong shocks can form also at the external boundary of such large structures (Kang et al., 1994). One more example of different objects are radio galaxies like Cygnus A or Centaurus A. Line emission and thermal X-ray emission have shown the presence of shock waves in the highly luminous radio lobes of these galaxies (Clark & Tadhunter, 1997; Kraft et al., 2003).

There are many sources, thus, where DSA seems to be the mechanism at work. Even though the distribution of particles such a mechanism produces is almost universal, the maximum energy a source is capable of producing strongly depends on the specific characteristics of the object. The cut-off energy and the spectral shape of the distribution around that energy, both for particles and for the emitted radiation, are good indicators of the properties of the source environment. The

acceleration process can be limited by several mechanisms. One of them is particle escape: particles are confined in the acceleration region only until their characteristic propagation length does not exceed the physical dimensions of the accelerator (the so-called Hillas criterion (Hillas, 1984)). The second limitation comes from the age of the system. As we will see in Chapter 2, in the model of DSA the energy of particles grows linearly with the acceleration time. The lifetime of the accelerator, therefore, poses a limit on the maximum achievable energy (Lagage & Cesarsky, 1983b). Finally, there is one more mechanism that needs to be taken into account in this context: energy losses. In the interaction with the environment, high energy particles emit the radiation we observe. We can ideally plot acceleration versus energy losses and identify the sources in which the maximum energy is limited by the radiative cooling of particles.

In the next Section we present the basic characteristics of three of the systems where this is the case and that is, therefore, the field of application of our calculation: Supernova Remnants, clusters of galaxies and microquasars.

1.2 Supernova Remnants

SNR are the favoured candidates for Galactic CRs and one of the best studied classes of non-thermal sources. They have been detected in non-thermal radio, X-rays and gamma-rays, providing us with unambiguous evidence of the presence of relativistic electrons. The occurrence of shocks is independently confirmed by the detection of thermal X-rays from shock-heated plasma in the interior of SNR shells (e.g. Decourchelle et al., 2001; Cassam-Chenaï et al., 2004, data obtained with the satellite XMM-Newton; and Warren et al., 2005, Chandra data). The shock velocities are inferred to be $1000 \lesssim v_S < 6000$ km/s (e.g. Kirshner et al., 1987; Laming, J. Martin; Hwang, Una, 2003; Uchiyama et al., 2007; Vink, 2008). The non-thermal luminosity found in correspondence with the shock location constitutes strong evidence for the actual realisation of the DSA mechanism. The so-called historical SNR (those for which we have historical records of the date of explosion) have been studied in great detail and provide us with a quite consistent general

picture: SN 1006, named after the year of explosion, Tycho, exploded in 1572, and Kepler (1604), present prominent radio and non-thermal X-ray emission with a good morphological match (e.g. Hwang et al., 2002), interpreted as synchrotron radiation from a population of high energy electrons (Koyama et al., 1995; Bamba et al., 2003; Dickel et al., 1991; Hwang et al., 2002; Vink, 2008). From the peak in the X-ray spectrum it is possible to estimate the maximum energy of the accelerated electrons, after making assumptions on the strength of the magnetic field. Assuming a field strength close to the interstellar value of a few microGauss, maximum energies of tens to ~ 100 TeV are found (Bamba et al., 2003; Hwang et al., 2002). Noticeably though, the very high angular resolution of the Chandra satellite allowed to reveal that non-thermal X-ray emissions occurs in very narrow filamentary structures, usually called rims. Several analyses (e.g. Bamba et al., 2005) suggest that, in fact, the magnetic field in the rims may be up to a couple of orders of magnitude larger than the average ISM value. In this case the cooling length of electrons becomes short enough to explain the width of the rims. The result is very interesting because it seems in agreement with the theoretical prediction of magnetic field amplification induced by shock accelerated particles proposed by Lucek & Bell, 2000. If, on the one hand, an enhanced magnetic field implies a lower maximum energy for the electrons, on the other, it also suggests a much higher efficiency of SNR shocks as Cosmic Ray accelerators.

Similarly, X-ray rims and magnetic field amplification have been observed in Cassiopeia A (Cas A) (Vink & Laming, 2003; Berezhko & Völk, 2004), a 300 yr old SNR. Cas A and RX J1713.7-3946, an older remnant of about 1600 yr, show similar characteristics to those just described in radio and X-rays, where synchrotron emission has been observed (Baars et al., 1977; Allen et al., 1997; Favata et al., 1997, for Cas A and Ellison et al., 2001; Koyama et al., 1997; Slane et al., 1999, for RX J1713.7-3946). In addition CasA and RX J1713 have been detected also in gamma-rays with the Cherenkov telescopes HEGRA (Aharonian et al., 2001) and MAGIC (Albert et al., 2007a), and CANGAROO (Enomoto et al., 2002) and HESS (Aharonian et al., 2004), respectively. At present the Spectral Energy Distribution of these objects in the TeV band can be fit equally well both by IC emission of

electrons and pion decay generated by hadronic processes (Aharonian et al., 2006a for RX J1713.7-3946). The leptonic scenario requires a magnetic field $B \lesssim 10 \mu\text{G}$, whereas for higher values of B the hadronic scenario is favoured.

To summarise, SNR are established sources of very high energy electrons. Acceleration seems to proceed via Diffusive Shock Acceleration in magnetic fields of the order of hundreds of microGauss. The maximum energy of the electrons is determined by radiative energy losses.

1.3 Microquasars

Microquasars are galactic binary systems composed of a regular star being accreted onto a compact object (neutron star or black hole) that presents a jet.

Non-thermal emission has been observed from these objects from radio to X-rays (for a review see Mirabel & Rodriguez, 1999). Gamma-rays have also been detected from the confirmed microquasar Cygnus X-1 (Albert et al., 2007b) and from two candidates: LS 5039 (Aharonian et al., 2005) and LS I +61 303 (Albert et al., 2006). As an example, we take here the case of LS 5039, assuming that it is a microquasar, in order to highlight how these kinds of objects are interesting in the framework of our study. As discussed in Khangulyan et al. (2008), in order to explain the observed periodicity of the TeV signal (Aharonian et al., 2006b), the emission region must be inside the system, therefore at a distance from the compact object not much bigger than the separation with the companion star. Even though the system is rather complex and not yet well understood, particle acceleration can take place in the jet via different mechanisms (e.g. Bosch-Ramon & Khangulyan, 2008 for a review), at different scales. At the binary system scale, one of them is DSA in the jet.

The photon field produced by the companion star has a black body distribution at $T \simeq 3.8 \times 10^4 \text{ K}$ and provides a natural target for electrons accelerated in the jet of the compact object. The luminosity of the star is estimated in $L_* \simeq 7 \times 10^{38} \text{ erg s}^{-1}$ and the radius of the system is $R \sim 2 \times 10^{12} \text{ cm}$ (Casares et al., 2005). At distances of the order of the orbital radius, IC cooling can result in the dominant energy loss channel and the radiative cooling time scale for electrons are of the order of tens

to hundreds of seconds (Khangulyan et al., 2008). In this scenario acceleration and emission regions are very likely to coincide.

1.4 Clusters of Galaxies

Rich clusters of galaxies are the largest virialised structures in the Universe, with typical sizes of a few Mpc and masses up to $10^{15} M_{\odot}$ or more (see Sarazin, 1988 for a review). In the standard picture of cosmic structure formation, structures growth is driven by gravitational instability. This process is hierarchical, with larger systems forming later via the assembly of pre-existing smaller structures (for a thorough description see Peebles, 1980). Within this scenario, galaxy clusters form via mergers, and their age can be estimated to be of the order of 10 Gyr (e.g. Borgani & Guzzo, 2001). In addition, cold material from the surrounding environment is continuously infalling, due to gravitational attraction, and an expanding shock wave, called the accretion shock, is expected to form at the cluster boundary and carry outward the information of virialisation (Bertschinger, 1985). Numerical simulations have confirmed the appearance of so-called accretion shocks during structure formation (e.g. Kang et al., 1994).

The detection of a tenuous and diffuse synchrotron radio emission from about one third of rich clusters of galaxies (Govoni & Feretti, 2004; Carilli & Taylor, 2002) reveals the presence of a diffuse magnetic field and of a population of high energy electrons. Using exclusively synchrotron data, though, it is possible to get information only on the product of particles density and magnetic field energy density (unless adopting assumptions like equipartition). Non-thermal X-rays have also been detected from such sources and commonly interpreted as inverse Compton emission from the same population of electrons (Fusco-Femiano et al, 1999). Since IC depends on the electron density but not on the magnetic field, combining the data allows us to break the degeneracy and thus determine values of B in the range $0.1 - 1 \mu\text{G}$ (see also Enßlin et al., 2005 and references therein). If shock acceleration of electrons takes place at the accretion shock of clusters, the maximum energy is determined by radiative energy losses, since the particle escape from such an ex-

tended system and the accelerator age correspond to much longer time scales than that of energy losses.

In this particular class of objects, the evolution time scales are so long that energy losses are also the limiting mechanism for proton acceleration. It has been shown (Völk et al., 1996; Berezhinsky et al., 1997) that accelerated protons are confined in clusters for a time longer than the age of the universe, therefore being in principle able to undergo acceleration for a Hubble time, $t_{Hubble} = 1/H_0 \simeq 14$ Gyr, where H_0 is the Hubble constant. In fact clusters of galaxies seem to have all the ingredients to be very effective accelerators. It has been shown that the pair and pion production energy losses induced by the interaction of protons with the CMB radiation field limit their maximum energy to around 10^{19} eV (Norman et al., 1995; Kang et al., 1997). The secondary electrons from proton energy losses are expected to contribute at some level to the emission in the radio, X-ray and gamma-ray bands (Blasi et al., 2007).

As we have pointed out, electromagnetic radiation is of fundamental importance to track the presence of high energy particles inside sources. The association of the detection of non-thermal radiation and of shock waves is striking. Moreover, energy losses are one of the mechanisms that can be responsible in determining the maximum acceleration energy. If this is the case, the two processes need to be taken into account self-consistently. We dedicate the next two Chapters to introduce the basic ideas and mathematical treatment of the two aspects of the problem: Diffusive Shock Acceleration and radiative energy losses.

Chapter 2

Diffusive Shock Acceleration

One of the most successful theories in High Energy Astrophysics is the one connecting the origin of non-thermal high energy particles with the presence of shock waves via a mechanism known as Diffusive Shock Acceleration. To date it represents one of the major and best developed models of Cosmic Ray acceleration, invoked almost universally in sources presenting non-thermal behaviour and in explaining observations of non-thermal radiation.

In this chapter we introduce some basic concepts of plasma physics and of collisionless shock waves and then proceed to illustrate the model of DSA.

2.1 Plasma Equations

For this section we refer to the following textbooks: Landau & Lifshitz (1959); Krall & Trivelpiece (1973); Shu (1992); Vietri (2006).

The greatest part of the baryonic matter in the Universe is found in an ionised state, i.e. in the form of plasma. In a plasma the density of particles is low enough to make the direct Coulomb interactions between near-neighbours completely negligible and every particle experiences the long-range potential produced by the ensemble of all other particles.

We are specifically interested in magnetised plasmas, because, as we will see, the presence of a magnetic field is a fundamental ingredient of the acceleration

mechanism at shocks. In the presence of a generic electromagnetic field, the plasma can be described in the magnetohydrodynamic (MHD) framework. This includes self-consistently Maxwell's equations in a fluid treatment of the plasma.

We shall start off with the fluid equations. Rather than approaching the plasma with a kinetic description, it is more convenient to identify its macroscopic quantities and to study their properties. In treating a fluid it is usually preferred to adopt lagrangian coordinates, i.e. coordinates that move along the flow attached to the fluid element. The variation of such an element with time is now given by its lagrangian comoving derivative $D/Dt = \partial/\partial t + \vec{v} \cdot \nabla$.

To describe the fluid we define the distribution function $f(\vec{x}, \vec{p}, t)$, which represents the number density of particles per unit volume in phase space. It is worth noting that the unit (infinitesimal) volume is still to be considered big enough to contain a high number of particles so that the distribution function has a statistical meaning and the physical quantities are treated as continuous. By definition, the total number of particles is:

$$N = \int f(\vec{x}, \vec{p}, t) d^3x d^3p. \quad (2.1)$$

We said that the interactions between near-neighbours in a plasma can be ignored, while the effect of the long-range fields can be described by a mean potential, therefore the evolution of the distribution function is described by the collisionless Boltzmann equation, also known as the Vlasov equation:

$$\frac{\partial f}{\partial t} + \vec{v} \cdot \nabla f - \nabla \Phi \cdot \frac{\partial f}{\partial \vec{p}} = 0, \quad (2.2)$$

where $\vec{v} = \vec{p}/m$ is the particle velocity and Φ is the potential acting on the plasma. The above equation can be read simply as: the evolution of the distribution function in lagrangian coordinates is due to the external forces ($-\nabla\Phi$) applied to the fluid element.

By taking the moments of the Vlasov equation, we obtain conservation equations involving the macroscopic quantities of the plasma, which are the observables of the

system. The generic velocity moment is defined by:

$$\langle \chi_i \rangle = \frac{\int \chi_i f(\vec{x}, \vec{p}, t) d^3 p}{\int f(\vec{x}, \vec{p}, t) d^3 p}, \quad (2.3)$$

with $\chi_i = m \vec{v}^i$. Moreover it is, by definition:

$$n = \int f(\vec{x}, \vec{p}, t) d^3 p, \quad (2.4)$$

n being the number density of the fluid. The generic moment of the Vlasov equation (2.2) can be written as:

$$\int \chi_i \left[\frac{\partial f}{\partial t} + \vec{v} \cdot \nabla f + \vec{F} \cdot \frac{\partial f}{\partial \vec{p}} \right] d^3 p = 0, \quad (2.5)$$

with $\vec{F} = -\nabla \Phi$ the external forces. Since t and \vec{x} commute with operators in \vec{v} , the first term results in:

$$\int \chi_i \frac{\partial f}{\partial t} d^3 p = \frac{\partial}{\partial t} \int \chi_i f d^3 p = \frac{\partial}{\partial t} n \langle \chi_i \rangle$$

and the second term can be integrated by parts to obtain:

$$\int \chi_i \vec{v} \cdot \nabla f d^3 p = \int \nabla \cdot (\chi_i \vec{v} f) d^3 p - \int \nabla \cdot (\chi_i \vec{v}) f d^3 p = \nabla \cdot (n \langle \chi_i \vec{v} \rangle);$$

where we used the fact that $\nabla(\chi_i \vec{v})$ vanishes because χ_i is a function only of velocity. In the third term on the left-hand side of Eq. (2.5), we can reasonably assume that \vec{F} does not depend on the velocity, or better that the n -th component of the force does not depend on the n -th component of the velocity (it is the case for the Lorentz force). Therefore:

$$\int \chi_i \vec{F} \cdot \frac{\partial f}{\partial \vec{p}} d^3 p = \vec{F} \cdot \int \chi_i \frac{\partial f}{\partial \vec{p}} d^3 p = \vec{F} (\chi_i f) \Big|_{-\infty}^{+\infty} - n \vec{F} \cdot \left\langle \frac{\partial \chi_i}{\partial \vec{p}} \right\rangle.$$

If we assume that the distribution function vanishes at infinity, we finally obtain:

$$\frac{\partial}{\partial t} n \langle \chi_i \rangle + \nabla \cdot (n \langle \chi_i \vec{v} \rangle) - n \vec{F} \cdot \left\langle \frac{\partial \chi_i}{\partial \vec{p}} \right\rangle = 0 \quad (2.6)$$

as the general expression for the moment of the Vlasov equation. As we can see this is a conservation equation for the quantity $\langle \chi_i \rangle$. We define the quantity $\vec{f} = n \vec{F}$, that represents the force density.

Now we immediately obtain the equations of hydrodynamics by substituting χ_i .

$$- \chi_0 = m$$

$$\frac{\partial \rho}{\partial t} + \nabla \cdot (\rho \vec{u}) = 0 \quad \text{continuity equation} \quad (2.7)$$

where ρ is the mass density and $\vec{u} = \langle \vec{v} \rangle$ is the bulk velocity of the plasma and we shall always assume it non-relativistic.

$$- \chi_1 = m \vec{v}$$

$$\rho \frac{\partial \vec{u}}{\partial t} + \rho \vec{u} \cdot \nabla \vec{u} + \nabla P - \vec{f} = 0 \quad \text{Euler equation} \quad (2.8)$$

where we made use of the continuity equation. P represents the pressure tensor whose components are defined as $P_{ij} = \rho \langle w_i w_j \rangle$, where \vec{w} is the random component of the particle velocity as opposite to \vec{u} that represents the ordered one: $\vec{v} = \vec{u} + \vec{w}$. For an ideal fluid with no viscosity, the pressure tensor is diagonal (i.e. there are no tangential stresses).

$$- \chi_2 = m \vec{v}^2$$

$$\frac{\partial}{\partial t} \rho \langle \vec{v}^2 \rangle + \nabla \cdot (\rho \langle \vec{v}^2 \vec{v} \rangle) - \vec{f} \cdot \vec{u} = 0. \quad (2.9)$$

The above equation requires some more manipulation to read out the macroscopic quantities of interest. As we mentioned, the velocity can be split in two components: the mean velocity \vec{u} and the fluctuations \vec{w} around this value. By definition $\langle \vec{w} \rangle = 0$. Therefore we obtain:

$$\frac{\partial}{\partial t} \rho (\vec{u}^2 + \langle \vec{w}^2 \rangle) + \nabla \cdot (\rho (\vec{u}^2 \vec{u} + \langle \vec{w}^2 \rangle \vec{u} + \frac{\langle \vec{w}^2 \rangle}{3} \vec{u})) - \vec{f} \cdot \vec{u} = 0. \quad (2.10)$$

In the second last term we used again the assumption of ideal fluid: $\langle w_i w_j \rangle = \frac{\langle \vec{w}^2 \rangle}{3} \delta_{ij} = P \delta_{ij}$. In the first term in Eq. (2.10), $\rho \vec{u}^2$ is clearly twice the kinetic energy density of the bulk motion, while $\rho \vec{w}^2$ is associated with the chaotic motion, i.e. it represents twice the internal energy ϵ of the system. With these considerations in mind, we divide Eq. (2.10) by 2 and rewrite it as:

$$\frac{\partial}{\partial t} \left(\frac{\rho \vec{u}^2}{2} + \epsilon \right) + \nabla \cdot \left[\rho \vec{u} \left(\frac{\vec{u}^2}{2} + \frac{\epsilon}{\rho} + \frac{P}{\rho} \right) \right] - \vec{u} \cdot \vec{f} = 0. \quad \text{energy conservation} \quad (2.11)$$

Every time we calculated a moment we have introduced a new variable (density, velocity, pressure, internal energy). To close the set of equations we will need to assume an equation of state for the fluid.

Now that we have the general conservation equations of hydrodynamics, we move on to take into account the second ingredient of MHD, namely the Maxwell equations. For typical length scales of astrophysical interest, we can assume quasi-neutrality of the plasma, which means that there is no net electric charge. Therefore Maxwell's equations read:

$$\begin{aligned}\nabla \cdot \vec{E} &= 0; & \nabla \wedge \vec{E} &= -\frac{1}{c} \frac{\partial \vec{B}}{\partial t}; \\ \nabla \cdot \vec{B} &= 0; & \nabla \wedge \vec{B} &= \frac{4\pi}{c} \vec{j},\end{aligned}$$

where \vec{j} is the current density induced by the magnetic field. Note that here and in the following we adopt the gaussian c.g.s. unit system. From a simple order of magnitude estimation, one can see that, if we call L and τ the typical length and time scales of the electromagnetic field variation and we assume that $L/\tau \sim u$, the electric field induced by the second of the Maxwell equations (2.1) is of the order $E \sim (u/c)B$, with $u/c \ll 1$. For its time variation (i.e. the drift current that should appear in the fourth Maxwell equation) it follows that $E/(c\tau)L/B \sim E/B (u/c) \sim (u/c)^2$, second order in u/c . Therefore we neglected it.

The Lorentz force (per unit volume) is:

$$\vec{f} = \frac{\vec{j} \wedge \vec{B}}{c} \quad (2.12)$$

and from the fourth Maxwell equation:

$$\vec{f} = \frac{(\nabla \wedge \vec{B}) \wedge \vec{B}}{4\pi}. \quad (2.13)$$

To obtain the ideal MHD equations we only need one more step, which is the assumption that the conductivity of the plasma is infinite and no thermal dissipation is introduced by the presence of \vec{B} . Therefore the MHD equations, that express the conservation of mass, momentum and energy, are obtained by substituting Eq. (2.13) into Eq. (2.7), (2.8) and (2.11):

$$\frac{\partial \rho}{\partial t} + \nabla \cdot (\rho \vec{u}) = 0; \quad (2.14)$$

$$\rho \frac{\partial \vec{u}}{\partial t} + \rho \vec{u} \cdot \nabla \vec{u} + \nabla P - \frac{(\nabla \wedge \vec{B}) \wedge \vec{B}}{4\pi} = 0; \quad (2.15)$$

$$\frac{\partial}{\partial t} \left(\frac{\rho \vec{u}^2}{2} + \epsilon + \frac{B^2}{8\pi} \right) + \nabla \cdot \left[\rho \vec{u} \left(\frac{\vec{u}^2}{2} + \frac{\epsilon}{\rho} + \frac{P}{\rho} \right) + \frac{1}{4\pi} \vec{B} \wedge (\vec{u} \wedge \vec{B}) \right] = 0. \quad (2.16)$$

2.2 Collisionless Shock Waves

In the following we consider an ideal magnetised plasma as defined in the previous Section. The flow is adiabatic and the equation of state, needed to close the MHD set of equations, is of the form

$$P = K \rho^\gamma, \quad (2.17)$$

where K is a constant and γ is the adiabatic index of the gas. We assume γ to be that of an ideal non-relativistic gas, which means $\gamma = 5/3$ for a monoatomic gas. Moreover, for all astrophysical systems we will deal with in this work, the magnetic energy density is much smaller than the ram pressure of the plasma: $B^2/8\pi \ll \rho u^2$. Therefore the dynamical effect of the magnetic field on the system is negligible.

If a perturbation is induced in the plasma, it will propagate in the medium. In a magnetised plasma two characteristic velocities exist for the propagation of perturbations: the sound velocity c_s , associated with the propagation of pressure waves, and the Alfvén velocity v_A , characteristic of incompressible magnetohydrodynamic (Alfvén) waves, defined as:

$$c_s^2 = \frac{\partial P}{\partial \rho} = \gamma \frac{P}{\rho}; \quad (2.18)$$

$$v_A^2 = \frac{B^2}{4\pi\rho}. \quad (2.19)$$

In the astrophysical environments we are interested in, $v_A^2/c_s^2 = (2/\gamma)(B^2/(8\pi P)) \leq 1$ (see Vietri, 2006). Therefore, the sound velocity can be considered as the maximum speed a disturbance can propagate in the fluid.

We now consider a simple instructive example to illustrate what a shock wave is and then move to the actual case of interest. In a collisional fluid, such as air for example, the presence of an obstacle moving inside of it is felt by the fluid by means of the pressure waves that the object generates and that move away from it. If the obstacle moves inside the medium at a velocity greater than the speed of sound, the

propagation velocity of waves, the perturbation will not smoothly propagate into the fluid but more and more matter will run into the obstacle. Ahead of the obstacle a non-linear disturbance forms that grows rapidly to form a sharp discontinuity propagating at supersonic velocity in the undisturbed fluid. Such a discontinuity is called a shock wave.

Mathematically, a shock wave is a sharp discontinuity in all the macroscopic quantities of the fluid as velocity, density, pressure and temperature. In fact, the thickness of the discontinuity is finite, but much smaller than all the other length scales of the system so that we can simply neglect it. What happens at the shock surface is that the kinetic energy of the supersonic fluid is dissipated by some mechanism into thermal energy and the fluid is slowed down to a subsonic speed downstream of the shock. Therefore, if we choose a system of coordinates comoving with the shock surface (Fig. 2.1), the fluid results divided into three parts:

- upstream: in the region ahead of the shock the fluid moves towards it (now at rest) at supersonic velocity $u_1 > c_s$ and with a bulk energy density ρu_1^2 ;
- shock surface: in a very small region the ordered motion of the fluid is partially converted into a disordered motion by dissipating the kinetic energy into thermal energy, consequently heating up and slowing down the fluid. In this region entropy is not conserved. The physical dimension of the region is of the order of the length scale of the kind of interactions responsible for the dissipations.
- downstream: in the region behind the shock the fluid moves away from it at a subsonic velocity $u_2 < c_s$ because part of the kinetic energy of the ordered motion is now found in terms of thermal energy and the density, pressure and temperature of the fluid have increased. Note that in the observer rest frame, the fluid in the downstream region is still moving in the same direction as the shock but at a lower speed, therefore recessing from it in its rest frame.

In our example the dissipation would occur by collisions between the particles of the fluid. In a collisionless magnetised plasma this is not the case. The dissipation

must occur by means of electromagnetic fields. The details of the mechanism are not well understood in this case, but the general picture is that a combination of disordered and possibly transient electric and magnetic fields are responsible for the randomisation of the velocities of particles. The characteristic length scale of the phenomenon is therefore the Larmor radius, $r_L = pc/qB$, of the particles, where p and q are the momentum and the charge of the particle, respectively, c is the speed of light and B the value of the magnetic field. The thickness of the shock can hence reasonably be assumed to be of the order of the Larmor radius of the thermal ions in the plasma that constitute the bulk of the fluid particles.

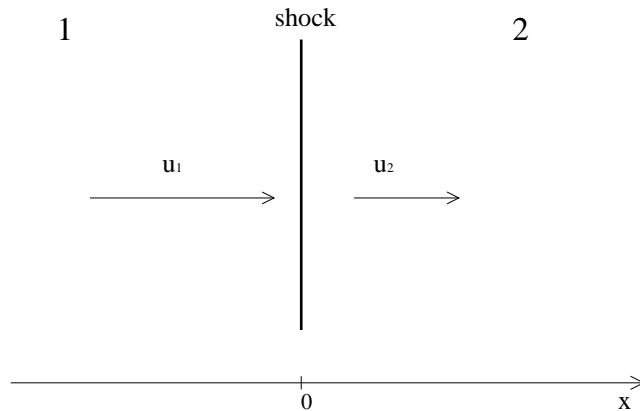


Figure 2.1: Shock rest frame: a plane infinite shock is located in $x = 0$. The fluid moves along the x -axis with velocity u_1 in the upstream region 1 (from $-\infty$ to 0) and with velocity u_2 in the downstream region 2 (from 0 to $+\infty$).

We now proceed to describe quantitatively how the macroscopic quantities of the plasma change at the shock crossing. For simplicity we consider an infinite plane shock and choose the coordinate system in which the shock is at rest and the fluid moves along the x -axis, normal to the shock surface, from $-\infty$ far upstream, to $+\infty$ far downstream and the shock is located at $x = 0$. We identify with the subscript 1 all the quantities in the upstream region and with 2 those in the downstream region, as in Fig. 2.1. To write the equations that describe the system we consider the MHD conservation equations (2.7), (2.8) and (2.11). In a steady state all the partial derivatives with respect to time are zero and the conservation of a generic flux Ψ can simply be written as $d\Psi/dx = 0$. This has to be true in the whole space, including

at the crossing of the shock because no mass, momentum nor energy is created by it. If we integrate the generic flux Ψ from a point 0_- immediately upstream of the shock and a point 0_+ immediately downstream, we obtain $\Psi_2 - \Psi_1 \equiv [\Psi] = 0$. The integration of Eq. (2.7), (2.8) and (2.11) then gives:

$$\begin{aligned} [\rho v_n] &= 0; \\ \left[\rho u_n^2 + P + \frac{1}{8\pi}(B_t^2 - B_n^2) \right] &= 0; \\ \left[\rho u_n \left(\frac{\vec{u}^2}{2} + \frac{\epsilon}{\rho} + \frac{P}{\rho} \right) + \frac{1}{4\pi}(B^2 u_n - B_n(\vec{u} \cdot \vec{B})) \right] &= 0, \end{aligned} \quad (2.20)$$

where the subscript n identifies the component parallel to the shock normal (usually referred to as parallel component) and t the one tangential to the shock surface (perpendicular component). Under the condition $B^2/8\pi \ll \rho u^2$, all the terms in B^2 can be neglected and the above equations simplify to the standard hydrodynamic ones:

$$\begin{aligned} [\rho v_n] &= 0; \\ [\rho u_n^2 + P] &= 0; \\ \left[\rho u_n \left(\frac{\vec{u}^2}{2} + \frac{\epsilon}{\rho} + \frac{P}{\rho} \right) \right] &= 0, \end{aligned} \quad (2.21)$$

which are known as Rankine-Hugoniot (or jump) conditions and describe the change in velocity, density and pressure at the shock crossing. Further equations to describe the change in the magnetic field are obtained simply by the circulation of the induced electric field $\vec{E} = -(\vec{u} \wedge \vec{B})/c$ along a closed line and the Gauss theorem for the magnetic field (remember that when we chose the coordinate system we defined $\vec{u} = u_n \hat{x}$):

$$\begin{aligned} [E_t] &= [-B_t u_n] = 0; \\ [B_n] &= 0. \end{aligned} \quad (2.22)$$

Before manipulating the jump conditions (2.21), we introduce the two main parameters that describe a shock wave: the compression ratio

$$r = \frac{\rho_2}{\rho_1}, \quad (2.23)$$

which describes quantitatively the enhancement of the plasma density after crossing the shock, and the Mach number

$$M_1 = \frac{u_1}{c_s}, \quad (2.24)$$

where the subscript 1 refers to the upstream region and the sound speed c_s has to be taken in the same region.

It is easy to correlate the two quantities just defined by means of the equation of state (2.17) and Eq. (2.18). A simple manipulation gives (e.g. Landau & Lifshitz, 1959):

$$r = \frac{(\gamma + 1)M_1^2}{2 + (\gamma - 1)M_1^2}. \quad (2.25)$$

We now notice an extremely important fact: by increasing the upstream Mach number, namely the strength of the shock, the compression ratio does not increase indefinitely. Rather the opposite, while M_1 can grow theoretically to infinity, quite soon ($M_1 \gtrsim 10$) the compression ratio converges to:

$$r = (\gamma + 1)/(\gamma - 1), \quad (2.26)$$

which, for a monoatomic non-relativistic gas, means

$$r = 4. \quad (2.27)$$

We can therefore state that for all strong shocks, which are those we are interested in here, the compression ratio can be set equal to 4.

The first one of the Rankine-Hugoniot conditions (2.21) connects the jump in density with the jump in velocity at the shock:

$$\frac{\rho_2}{\rho_1} = \frac{u_1}{u_2} = r, \quad (2.28)$$

so the bulk velocity is decreased by dissipation at the shock by at most a factor 4. We can now use the above equation together with the second of the (2.21) conditions to obtain the jump in pressure:

$$\frac{P_2}{P_1} = \frac{2\gamma M_1^2 - (\gamma - 1)}{\gamma + 1}. \quad (2.29)$$

From this relation it is straightforward to obtain also the change in temperature by means of the equation of state, obtaining:

$$\frac{T_2}{T_1} = \frac{1}{r} \frac{P_2}{P_1}. \quad (2.30)$$

Eq. (2.29) and (2.30) show an enhancement for the temperature and the pressure downstream compared to their values upstream that goes like M_1^2 , so, in the limit for strong shocks, the plasma gets strongly heated and compressed while the velocity and density are changed only by a factor of few.

The randomisation of the total energy of the system and the consequent heating up of the plasma is the basic effect of the presence of a shock, but not the only one and definitely not the most important if we are interested in high energy phenomena. In the next section we present a mechanism through which shocks are thought to be responsible for the acceleration of Cosmic Rays.

2.3 Diffusive Shock Acceleration

In 1949 Enrico Fermi proposed a model for acceleration based on the encounters and scattering of charged particles off magnetic field irregularities inside clouds of plasma in stochastic motion in the Interstellar Medium. But due to the stochasticity of the directions of movement of the clouds (and the scattering centres therein), the net acceleration turns out to be very inefficient because some of the encounters can lead to a loss of energy by the particle rather than a gain. Nevertheless, the basic idea proved to be very successful. In the late '70s a series of papers (Axford et al., 1977; Krymsky, 1977; Bell, 1978; Blandford & Ostriker, 1978) showed how the scattering off moving magnetic irregularities applied to shock waves can lead to a very powerful acceleration mechanism.

The basic idea of the process relies on the presence, downstream and upstream, of magnetic turbulence. Such a turbulence is to be expected downstream for the presence itself of the shock and upstream it is generated by the particles themselves via a process known as streaming instability (e.g. see Wentzel, 1974; Bell, 1978). We do not discuss further the origin of such turbulence, for our purpose it is enough to

assume a disordered component of the magnetic field on top of the ordered background one. In particular when the turbulence reaches the level $\delta B \simeq B$, we enter the so-called Bohm regime where the particles effectively undergo one scattering per Larmor period. This implies:

$$D(E) = \frac{1}{3} r_L(E) c, \quad (2.31)$$

where $r_L = E/qB$ is the Larmor radius of a particle of energy E and charge q . Therefore, the diffusion coefficient grows linearly with energy. In this work we assume such a configuration, justified by the consideration that an efficient acceleration naturally increases the level of turbulence, which, in turn, sustains efficient acceleration itself (see e.g. Malkov & Drury, 2001).

Given this configuration, suprathermal particles cross the shock from upstream to downstream and there scatter off the magnetic irregularities, in a process that is elastic in the rest frame of the scattering centres and results in a diffusion process of the particles that provides a non-zero probability of recrossing the shock against the bulk flow. Strictly speaking, the magnetic field turbulence, constituted by magneto-hydrodynamical waves, moves with the Alfvén velocity with respect to the plasma so that the scattering is elastic in a frame moving with velocity $u \pm v_A$, but since $v_A \ll u$, v_A can be neglected. The same diffusion mechanism acts in the upstream region so that the particles can cross back and forth the shock surface several times. The key point is that, in the act of crossing the shock, the particles see, from the upstream rest frame, the downstream plasma moving towards them with a velocity $V = u_1 - u_2$ in modulus. Once isotropised downstream, some of the particles recross the shock and, from that rest frame, they see the upstream plasma, and the magnetic field in it, coming towards them with again a velocity $V = u_1 - u_2$ in modulus. The scenario is similar to that of a ball bouncing repeatedly off converging walls. The overall effect is such that the particle gains a small amount of energy on each shock crossing (see Longair, 1997).

In the following, we always consider the so-called test particle approximation, which consists of neglecting any dynamical reaction that the accelerated particles may have on the system. In this approximation, the shock and the background

plasma are not influenced by the presence of the supra-thermal population of particles. In fact, the non-linear effects connected with the release of such an assumption have undergone many interesting studies (Drury & Völk, 1981; Kang et al., 1996; Malkov, 1997; Berezhko & Ellison, 1999; Blasi, 2002) and we refer to Jones & Ellison (1991) and Malkov & Drury (2001) for reviews, but we do not treat this problem in the present work.

2.3.1 The Bell Approach

We present here the theory of shock acceleration following the approach first used by Bell (1978) and reviewed in Gaisser (1990).

We assume an ideally infinite, plane shock expanding at non-relativistic velocity V_s in an ideal plasma. The thickness of the shock is usually assumed to be of the order of the Larmor radius of the thermal particles, therefore high energy particles (i.e. with an energy well above the bulk thermal energy) see the shock surface as a sharp discontinuity and feel its presence only as a change in the background conditions of temperature, pressure and density. This is the population of particles that can undergo acceleration. In this work we always deal with highly relativistic particles so that their energy can be written as $E = pc$. For the treatment of shock acceleration this condition is not necessary, the requirement being only that the Larmor radius of particles that undergo acceleration is larger than the shock thickness. But since it simplifies the calculations, we shall assume it from the beginning.

In the lab frame we have a fluid at rest in the upstream region (therefore our lab frame coincides with the upstream rest frame) in which a shock wave propagates at velocity V_s . A relativistic particle with energy E_1 crosses the shock at an angle θ_1 with respect to the direction of the shock velocity, as in Fig. 2.2. Upon entering the downstream region, the particle experiences subsequent deflections by the turbulence in the magnetic field and its direction of motion gets randomised by diffusion. The turbulence (the “scattering centres”) moves with the velocity $V = -u_1 + u_2$ of the background plasma. For a non-relativistic shock $V/c = \beta \ll 1$. If we now move to the downstream rest frame (we prime all quantities in such a reference frame), we

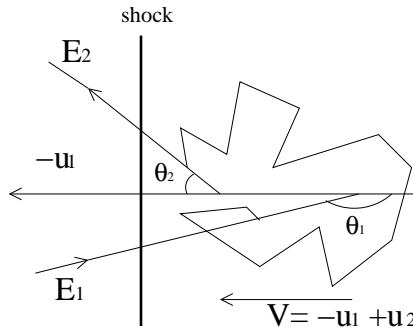


Figure 2.2: Shock moving with velocity $V_s = -u_1$ in the lab frame. In this frame, the downstream fluid moves in the same direction as the shock with velocity $V = -u_1 + u_2$. E_1 is the initial energy of a relativistic particle crossing the shock at an angle θ_1 with respect to V_s . After diffusion, it recrosses the shock at an angle θ_2 with energy E_2 .

have that our particle's motion becomes diffusive and therefore the particle has a non-vanishing probability $(1 - P_{esc})$ to return to the shock surface, where P_{esc} is the probability to be advected away and escape any further shock crossing. Since all the scatterings off the magnetic turbulence are elastic, when the particle crosses back towards the upstream region, at an angle θ'_2 with respect to V , its energy in the downstream rest frame is unchanged: $E'_2 = E'_1$. Coming from downstream, at the crossing of the shock, the fluid upstream is seen by the particle as approaching it at a velocity $V = u_1 - u_2$. Now we move back to our original frame upstream. Assuming that magnetic turbulence is present in this region too, the particle undergoes further diffusion that isotropises its motion again, before being advected back to the shock. To see what the net result of this whole cycle is in terms of energy budget, we have to evaluate $\Delta E = E_2 - E_1$ in the lab frame. For the first crossing from upstream to downstream we apply a Lorentz transformation:

$$E'_1 = \Gamma E_1 (1 - \beta \cos \theta_1), \quad (2.32)$$

where Γ is the Lorentz factor of the downstream fluid. When the particle crosses back, we apply a second Lorentz transformation in the opposite direction and obtain:

$$E_2 = \Gamma E'_2 (1 + \beta \cos \theta'_2). \quad (2.33)$$

Since $E'_2 = E'_1$, we easily find:

$$\Delta E = \xi E_1, \quad (2.34)$$

where ξ is given by:

$$\xi = \frac{1 + \beta \cos \theta'_2 - \beta \cos \theta_1 - \beta^2 \cos \theta_1 \cos \theta'_2}{1 - \beta^2} - 1. \quad (2.35)$$

The key point is that ξ is always positive for the system we are describing, leading to a net gain in energy at every cycle. The reason why $\xi > 0$ resides mathematically in the range allowed for the angles θ_1 and θ'_2 , but can be better physically understood by thinking of the system as a ball trapped between converging walls. The single encounter in the frame of the wall is elastic but the motion of the wall towards the ball kicks it at a higher energy. In this analogy the “walls” represent the magnetic field irregularities on the opposite side of the shock that, from the point of view of the particle, move towards it at a velocity V in modulus at every crossing.

If we call E_0 the energy of the particle before the first crossing of the shock, after n cycles the energy is given by:

$$E_n = E_0(1 + \xi)^n. \quad (2.36)$$

Inverting the above relation we obtain the number of cycles needed to achieve a certain energy:

$$n = \frac{\ln(E/E_0)}{\ln(1 + \xi)}. \quad (2.37)$$

If we assume that the probability $(1 - P_{esc})$ to return to the shock at every cycle remains constant, the number of particles that have reached an energy greater than a fixed value E , starting from E_0 , is:

$$N(\geq E) \propto \sum_{k=n}^{\infty} (1 - P_{esc})^k = \frac{(1 - P_{esc})^n}{P_{esc}} \quad (2.38)$$

and substituting Eq. (2.37), it results in:

$$N(\geq E) \propto \frac{1}{P_{esc}} \left(\frac{E}{E_0} \right)^{-\delta}, \quad (2.39)$$

with

$$\delta = -\frac{\ln(1 - P_{esc})}{\ln(1 + \xi)}. \quad (2.40)$$

To obtain the average gain in energy for different particles we have to average over the angles $\cos\theta_1$ and $\cos\theta'_2$ in Eq. (2.43) by simply projecting an isotropic distribution of particles onto the shock surface:

$$\frac{dn}{d\cos\theta} = 2\cos\theta. \quad (2.41)$$

In order to actually cross the shock a particle must have $0 \leq \cos\theta'_2 \leq 1$ and $-1 \leq \cos\theta_1 \leq 0$, giving: $\langle \cos\theta'_2 \rangle = 2/3$ and $\langle \cos\theta_1 \rangle = -2/3$. The resulting expression for ξ is:

$$\xi = \frac{1 + \frac{4}{3}\beta + \frac{4}{9}\beta^2}{1 - \beta^2} - 1 = \frac{\frac{4}{3}\beta + \frac{13}{9}\beta^2}{1 - \beta^2}. \quad (2.42)$$

Since $\beta \ll 1$ by construction, we can perform a Taylor expansion at the first order and obtain:

$$\xi \simeq \frac{4}{3}\beta = \frac{4}{3} \frac{u_1 - u_2}{c}. \quad (2.43)$$

As we can see, the average gain of energy per cycle is very small, being proportional to β (therefore DSA is also referred to as 1st order Fermi acceleration). Nevertheless, the mechanism is more efficient than the original model proposed by Fermi that leads to a gain in energy only of the order β^2 (2nd order Fermi process).

We now want to evaluate P_{esc} . The rate of crossings of the shock is obtained by projecting an isotropic flux onto the shock plane:

$$\int_0^{2\pi} d\phi \int_0^1 d\cos\theta \frac{nc}{4\pi} \cos\theta = \frac{nc}{4}, \quad (2.44)$$

where n is the number density of the accelerated particles. Of the particles that cross the shock once, a fraction is advected away downstream and never returns. Such a fraction is given by nu_2 . The probability of escaping further acceleration is given by:

$$P_{esc} = \frac{nu_2}{nc/4} = 4 \frac{u_2}{c}. \quad (2.45)$$

Being proportional to u_2/c , $P_{esc} \ll 1$.

If we now recall Eq. (2.40), we can expand it in Taylor series at the first order in P_{esc} and ξ and obtain:

$$\delta \simeq \frac{P_{esc}}{\xi} = 3 \frac{u_2}{u_1 - u_2}. \quad (2.46)$$

Using Eq. (2.23), we rewrite δ in terms of the shock compression ratio r as:

$$\delta = \frac{3}{r-1}, \quad (2.47)$$

giving an integral spectrum:

$$N(> E) \propto \left(\frac{E}{E_0}\right)^{-\frac{3}{r-1}} \quad (2.48)$$

and a differential spectrum:

$$\frac{dN(E)}{dE} \propto \left(\frac{E}{E_0}\right)^{-\alpha} = \left(\frac{E}{E_0}\right)^{-\frac{r+2}{r-1}}. \quad (2.49)$$

Remarkably, the spectral index depends only on the compression ratio of the shock, therefore on its Mach number, i.e. its strength, and it is totally independent of the other details of the system such as the value of the magnetic field, the injection process, the particular turbulence we assume or the form of the diffusion coefficient, all quantities generally very difficult to know in detail.

Recalling Eq. (2.27) we obtain:

$$\alpha = \frac{r+2}{r-1} \xrightarrow{M_1 \rightarrow \infty} 2. \quad (2.50)$$

For strong shocks, the acceleration mechanism naturally delivers a power law distribution $\propto E^{-2}$ of high energy particles.

2.3.2 The Transport Equation

A second approach to the problem is described in Axford et al. (1977); Krymsky (1977); Blandford & Ostriker (1978) and involves the direct solution of the transport equation for an isotropic distribution of particles in the presence of a shock wave. We recall here that the particle number density is:

$$n = 4\pi \int_0^\infty p^2 f(x, p, t) dp. \quad (2.51)$$

The transport equation reads (Skilling, 1975):

$$\frac{\partial f(x, p, t)}{\partial t} + u \frac{\partial f(x, p, t)}{\partial x} - \frac{\partial}{\partial x} \left(D(x, p) \frac{\partial f(x, p, t)}{\partial x} \right) - \frac{p}{3} \frac{\partial u}{\partial x} \frac{\partial f(x, p, t)}{\partial p} = Q(x, p). \quad (2.52)$$

The first two terms on the left-hand side represent the lagrangian derivative of f , the third term describes particles diffusion and the fourth the acceleration of particles at the shock front. On the right-hand side, $Q(x, p)$ is the injection term that describes how particles are removed from the background plasma and injected in the acceleration process. We assume that injection happens at the shock surface:

$$Q(x, p) = \tilde{Q}_0(p)\delta(x).$$

The velocity u is constant both up and downstream, even though it has different values in the two regions connected by Eq. (2.28). Its derivative is non-zero only at the shock location. In particular we can rewrite:

$$\frac{\partial u}{\partial x} = -(u_1 - u_2)\delta(x).$$

We now focus on the steady regime where $\partial f(x, p, t)/\partial t = 0$. To obtain the shape of the distribution function we integrate Eq.(2.52) over space. In the upstream and downstream regions the transport equation reduces to:

$$\frac{\partial}{\partial x} \left(D(x, p) \frac{\partial f(x, p, t)}{\partial x} \right) = u \frac{\partial f}{\partial x},$$

which can be easily integrated to give the solution

$$f(x, p) = (f_0 - f_\infty) \exp \left[\int_0^x \frac{u}{D(x', p)} dx' \right] + f_\infty, \quad (2.53)$$

where $f_0 = f(0, p)$ is the distribution function at the shock location, continuous across the shock, and f_∞ represents its value at $\pm\infty$, depending whether we are upstream or downstream.

- $x < 0$ (upstream)

Eventually all particles are advected back at the shock so that $f_{-\infty} = 0$.

Therefore the spectrum is:

$$f(x, p) = f_0 \exp \left[\int_0^x \frac{u}{D(x', p)} dx' \right]. \quad (2.54)$$

- $x > 0$ (downstream)

From Eq. (2.53) it follows that the only way for $f(x, p)$ to remain finite for increasing positive values of x is to be identically

$$f(x, p) = f_0. \quad (2.55)$$

Now we are left with the calculation of f_0 . We integrate once more Eq. (2.52) close to the shock, between 0_- immediately upstream and 0_+ immediately downstream, obtaining:

$$\frac{1}{3}(u_1 - u_2)p \frac{\partial f_0}{\partial p} = D_2 \frac{\partial f_0}{\partial x} \Big|_2 - D_1 \frac{\partial f_0}{\partial x} \Big|_1 + \tilde{Q}_0. \quad (2.56)$$

From Eq. (2.55) is $\partial f / \partial x|_2 = 0$ and from Eq. (2.54) $D_1 \partial f / \partial x|_1 = u_1 f_0$. Now the integration of Eq. (2.56) over p is straightforward and gives:

$$f_0(p) = qp^{-q} \int_0^p p'^{q-1} \frac{\tilde{Q}_0(p')}{u_1} dp', \quad (2.57)$$

where we defined the quantity $q = 3u_1 / (u_1 - u_2)$. Recalling Eq. (2.28), we can write $q = 3r / (r - 1)$. If the injection happens as a delta function in momentum as $\tilde{Q}_0 = Q_0 \delta(p - p_0)$, the integral in Eq. (2.57) results in a constant and the spectrum at the shock follows a power law in momentum of index q . For a strong shock, Eq. (2.27) implies $q = 4$. Therefore the spectrum as a function of the particle momentum is:

$$f(x, p) \propto p^{-4}. \quad (2.58)$$

To compare this result with the one obtained with the ‘‘Bell approach’’ in Section 2.3.1, we note that the total number density of particles is given, in terms of the particle energy, by the integral:

$$n = \int f'(E) dE. \quad (2.59)$$

Comparing this expression with Eq. (2.51), it gives $f'(E) dE = 4\pi p^2 f(p)$. Having made the assumption that the particles are relativistic, $E = pc$ and Eq. (2.58) leads to $f'(E) \propto E^{-2}$, which is the same result obtained with the previous approach.

2.4 The Maximum Energy

We have shown in the previous Section that the power law spectrum obtained via DSA does not depend on the details of the acceleration process, like the shape of the diffusion coefficient or the strength of the magnetic field, but rather tends to a universal value of the spectral index for strong shocks. On the other hand the maximum energy achievable by the particles does. The dependence on the specific parameters of the accelerator of this quantity and of the spectral shape around and above such an energy makes them an extremely powerful tool to explore the physical conditions of the accelerator and to diagnose the kind of mechanism at work.

The acceleration shuts off when the time scale of a competing mechanisms becomes comparable or shorter than the acceleration time scale. According to DSA, the acceleration process is due to the several crossings of the shock surface that a particle can undergo thanks to the diffusion it experiences both up and downstream. It is then natural to argue that the mean time the particle spends in each region depends on the diffusion time scale. Indeed, it can be shown that the time of a complete acceleration cycle is (see Drury (1983); Lagage & Cesarsky (1983a)):

$$T_{cycle} = \frac{4}{c} \left(\frac{D_1(E)}{u_1} + \frac{D_2(E)}{u_2} \right), \quad (2.60)$$

where we assumed again that the velocity of the particle is $\sim c$. The time needed to accelerate a particle to a certain energy can be evaluated considering $t_{acc} \simeq E/(\Delta E/T_{cycle})$. Using Eq. (2.34) and Eq. (2.60), we obtain:

$$t_{acc} = \frac{3}{u_1 - u_2} \left(\frac{D_1(E)}{u_1} + \frac{D_2(E)}{u_2} \right). \quad (2.61)$$

There are three mechanisms that compete in cutting off acceleration and the maximum energy is determined by which is the shortest of the associated time scales:

- i* Particle escape time from the accelerator: when the energy of the particle reaches a value big enough that its diffusion length exceeds the physical dimensions of the accelerator, the particle is no longer confined in the region and escapes, therefore not undergoing any further acceleration. If we call L the linear

dimension of the acceleration region, the particle escapes acceleration when its diffusion length scale is $l_D \simeq L$, where l_D is defined as $D(E)/u$. In the case of Bohm diffusion (Eq. (2.31)), the maximum energy is given by $E_{max} \simeq qBLu_1/c$.

ii Age of the accelerator: for DSA the energy a particle can achieve grows with the time it spends in the accelerator. Such time cannot exceed the age of the shock, therefore the latter sets a limit to the maximum energy. In this case, calling T_A the age of the accelerator, we have:

$$E_{max} \simeq T_A \frac{dE}{dt} \simeq T_A \frac{\xi E_{max}}{T_{cycle}}. \quad (2.62)$$

We need to assume a form of the diffusion coefficient in order to proceed. In the case of Bohm diffusion, $D(E)$ is given by Eq. (2.31) and we assume $D_1 = D_2$. Inserting the diffusion coefficient in Eq. (2.60) and using Eq. (2.43), as an estimate we then obtain:

$$E_{max} \simeq \frac{3}{20} \frac{u_1}{c} qBu_1 T_A. \quad (2.63)$$

iii Particle energy loss time: there are several possible channels of energy losses for accelerated particles. Synchrotron and inverse Compton are especially efficient in cooling electrons, while protons can undergo hadronic interactions like proton-photon pair production and meson production. These are the most efficient processes of energy losses for high energy particles in the most widely studied and observed environments.

Since energy losses are usually at work throughout the entire time of acceleration, the two processes happen simultaneously and the maximum energy is reached when the energy gain in a cycle is perfectly balanced by the energy loss in that cycle. Therefore the maximum energy can be estimated by:

$$\Delta E_{acc} = \Delta E_{loss} \quad (2.64)$$

and we rewrite the above expression as:

$$\frac{4}{3} \frac{u_1 - u_2}{c} E_{max} = \left(\frac{dE}{dt}(E_{max}) \right)_{loss} T_{cycle}. \quad (2.65)$$

All the above time scales depend on the specific combination of the values of the parameters present in the system. It implies that, as opposed to the spectrum at low energies, the maximum energy and the spectral shape of the cut-off bring important information on the accelerator. Our purpose is to study this part of the energy spectrum in the case where the scenario *iii* sets in, namely when energy losses determine the cut-off of the particle distribution.

Regarding electrons, we know that this scenario is usually dominating, causing the non-thermal radio to gamma-ray emission we observe. As an example, let us assume a nominal Supernova Remnant with fiducial values of the parameters. Keeping as a reference the observations presented in Chapter 1, we assume that the non-thermal synchrotron radiation is produced by electrons accelerated at a shock moving at velocity 3000 km/s in a magnetic field of 100 μ G. The ansatz is that the maximum energy is limited by energy losses, therefore we solve Eq. (2.65) for E_{max} , assuming a Bohm diffusion coefficient (Eq. (2.31)), and we find $E_{max} \simeq 23$ TeV. At such an energy, the time scale of synchrotron losses is about 54 yr. When compared to the age of the historical SNR, it is 1 order of magnitude smaller. Similarly, the diffusion length of the electrons results $l_D \simeq 2.5 \times 10^{16}$ cm, 1 to 2 orders of magnitude smaller than the usual size of a remnant, estimated of the order of a few up to tens of pc (Green, 2006). There is no doubt that in this class of objects the acceleration of electrons is limited by radiative losses. Indeed the case of synchrotron cooling has been studied in detail in previous works, as we discuss at the end of the next Chapter. But an analogous treatment for electrons undergoing IC in the Klein-Nishina regime is missing. This scenario, though, can be relevant in environments permeated with intense radiation fields. For objects like microquasars, for instance, the presence of a very luminous star in the system provides an energy density in the form of optical photons of the order of some hundreds of erg/cm^3 at a distance comparable to the radius of the binary system (Casares et al., 2005; Khangulyan et al., 2008). A similar value in terms of magnetic energy density would require a field value not smaller than ~ 50 G. As we noticed above, SNR appear to accelerate electrons up to tens of TeV. Synchrotron losses are often the dominant loss mechanism, but we have neglected so far the presence of background radiation. In the occurrence of a

SN explosion in a high radiation energy density environment, the contribution of IC may become relevant and even dominant. This could be the case in the innermost part of the Galaxy, where intense radiation fields have been observed (Davidson et al., 1992). Interestingly, for electrons of TeV energies, the inverse Compton process may proceed in the Klein-Nishina regime.

In the case of protons, the energy losses induced by the presence of the CMB via the production of electron-positron pairs and mesons happen on time scales of the order of a few Gyr in the energy range between 10^{18} and $\sim 5 \times 10^{19}$ eV (e.g. Kang et al., 1996). In large scale structures, protons are confined for a Hubble time. If suitable mechanisms are present, in principle they can undergo acceleration for a comparable time. Such a mechanism does exist and is shock acceleration at the external accretion shock of the structure. Energies of the order of 10^{19} or more can be reached on time scales of Gigayears, for typical values of the shock velocity $u_1 \sim 1000 - 3000$ km/s and a magnetic field of the order of a few tenths up to a few microGauss. In this case, the proton-photon interaction becomes the most efficient channel limiting acceleration. This environment is therefore very interesting in the framework of our study.

In the next Chapter we overview inverse Compton, synchrotron and proton-photon interaction mechanisms that we will later include in the DSA model.

Chapter 3

DSA in Presence of Energy Losses

While undergoing acceleration, particles can lose energy in a variety of ways in the interaction with the surrounding environment, constituted of three components: magnetic field, radiation and matter. The last one, however, is negligible in the context of this work, therefore we will deal only with the first two.

We know from observations that in many sources high energy electrons experience severe synchrotron and inverse Compton losses (see Chapter 1). We have shown in the last Chapter (Section 2.4) that the time scales involved can be so short to determine the cut-off of acceleration. The basics of the two emission processes are, thus, presented in the next section.

The same two mechanisms apply to protons. But, in many cases, they are not significant in limiting acceleration, due to the higher mass of protons compared to electrons and consequently their longer loss time scales. More interesting is a purely hadronic channel: the interaction of protons with photons producing a variety of particles that can in turn emit radiation.

After presenting synchrotron, inverse Compton and proton-photon interactions, we describe how the energy losses have been included in the model of DSA in previous works and the advantages and limitations of such methods.

3.1 Electromagnetic Interactions

Synchrotron and IC processes are very similar in the Thomson regime, but they deviate in the Klein-Nishina regime. We follow the formalism described in Blumenthal & Gould (1970) and Rybicki & Lightman (1979).

Let us consider an high energy electron (mass m and charge e) moving with Lorentz factor γ and velocity $\beta = \sqrt{1 - 1/\gamma^2}$ in an isotropic photon field. In the observer reference frame S, the electron travels along the x -axis as in Fig. 3.1. A photon of initial energy ϵ impinges into the electron at an angle θ with respect to the x -axis and gets scattered to an energy ϵ_1 . The kinematics of the scattering is more easily described in the electron rest frame S'. The initial energy of the photon in such a frame is Lorentz boosted as:

$$\epsilon' = \gamma\epsilon(1 - \beta\cos\theta). \quad (3.1)$$

In the frame S' the electron has initial and final four-momentum given by $P_{e,i} = (mc, \vec{0})$, $P_{e,f} = (E'/c, \vec{p}')$ and the photon $P_{ph,i} = (\epsilon'/c)(1, \vec{n}_i)$, $P_{ph,f} = (\epsilon'_1/c)(1, \vec{n}_f)$, where $\vec{n}_{i,f}$ are unitary vectors in the initial and final photon direction of motion. From the conservation of the four-momentum one obtains:

$$|P_{e,f}|^2 = |P_{e,i} + P_{ph,i} - P_{ph,f}|^2, \quad (3.2)$$

which leads to the condition:

$$\epsilon'_1 = \frac{\epsilon'}{1 + \frac{\epsilon'}{mc^2}(1 - \cos\Theta)} \quad (3.3)$$

for the energy of the final state of the photon, where $\cos\Theta = \cos(\theta' - \theta'_1)$ is the cosine of the angle between \vec{n}_i and \vec{n}_f . To obtain the energy of the photon in the observer frame it is enough to operate a second Lorentz transformation:

$$\epsilon_1 = \gamma\epsilon'_1(1 + \beta\cos\theta'_1). \quad (3.4)$$

In the Thomson limit $\epsilon' \ll mc^2$. Under this condition Eq. (3.3) simplifies and results in $\epsilon'_1 \simeq \epsilon'$, so that the final energy of the photon in the observer frame is:

$$\epsilon_1 \propto \gamma^2\epsilon. \quad (3.5)$$

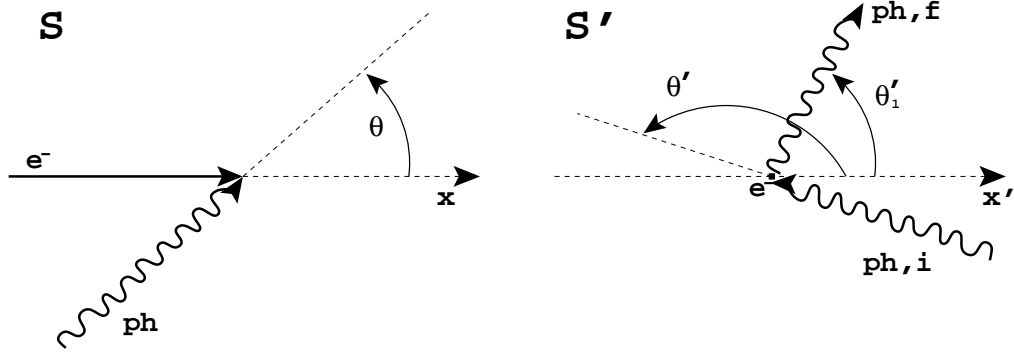


Figure 3.1: Sketch of the electron-photon interaction in the lab frame S (left) and in the electron rest frame S' (right).

As we see, the energy of the photon can be enhanced by several orders of magnitude by Compton upscattering.

It can be shown (Blumenthal & Gould, 1970) that the power emitted, i.e. the energy lost by the electron per unit time, can be related to the total energy density of the photon field in the electron rest frame as $-dE/dt = \sigma_T c U'_{rad}$, where $\sigma_T = 6.65 \times 10^{-25} \text{cm}^2$ is the Thomson cross-section defined as $\sigma_T = 8\pi e^4 / (3m^2 c^4)$. The photon energy density is defined as

$$U'_{rad} = \int \epsilon' dn', \quad (3.6)$$

dn' being the differential number density of photons. Since dn/ϵ is a Lorentz invariant, we use Eq. (3.1) to finally obtain the emitted power in the observer frame:

$$-\frac{dE}{dt} = \sigma_T c \int \epsilon'^2 \frac{dn'}{\epsilon'} = \sigma_T c \gamma^2 \int (1 - \beta \cos\theta)^2 \epsilon^2 \frac{dn}{\epsilon}. \quad (3.7)$$

For an isotropic distribution of photons, the average over the angle θ gives $\langle (1 - \cos\theta)^2 \rangle = 4/3$, where we made use of the fact that for relativistic electrons $\beta \rightarrow 1$. The average energy loss rate for a single electron in inverse Compton scattering off an isotropic distribution of photons in the Thomson regime reads:

$$-\frac{dE}{dt} = \frac{4}{3} \sigma_T c \gamma^2 U_{rad}. \quad (3.8)$$

In the case of black body radiation the energy density is expressed by the Stefan-Boltzmann law $U_{rad} = aT^4$, with $a = 7.56 \times 10^{-15} \text{erg cm}^{-3} \text{K}^{-4}$.

In the Thomson limit $\epsilon'/(mc^2) \ll 1$, which translates in the lab frame to the condition $\epsilon\gamma/(mc^2) \ll 1$ and the energy loss rate has a simple analytical expression. But in many cases of interest the maximum electron energy falls in the regime $\epsilon\gamma/(mc^2) \geq 1$. If for the CMB this implies an energy of the electrons of ~ 400 TeV, for optical photons the condition reduces to few hundreds of GeV. The simple formulae adopted so far are no longer valid and the relevant cross-section is given by the Klein-Nishina formula (Klein & Nishina, 1929) that we write here in the electron rest frame:

$$\sigma = \frac{3}{4}\sigma_T \left[\frac{1+x}{x^3} \left(\frac{2x(1+x)}{1+2x} - \ln(1+2x) \right) + \frac{1}{2x} \ln(1+2x) - \frac{1+3x}{(1+2x)^2} \right], \quad (3.9)$$

where we used the variable $x = \epsilon'/mc^2$. When $x \ll 1$, $\sigma \simeq \sigma_T$, i.e. the Thomson cross-section is recovered, as expected. A simple expression can be found also in the opposite situation, in the extreme Klein-Nishina limit $x \gg 1$:

$$\sigma \simeq \frac{3}{8}\sigma_T \frac{1}{x} \left(\ln 2x + \frac{1}{2} \right), \quad (3.10)$$

but in the intermediate regime the complete cross-section has to be used, leading to a more complex shape of the energy losses. Eq. (3.10) shows how the cross-section decreases with energy in the Klein-Nishina limit. It can be shown (Blumenthal & Gould, 1970) that in the limit $x \gg 1$ the energy loss rate of the electron in the lab frame is:

$$-\frac{dE}{dt} \propto \ln \left(\frac{\gamma\epsilon}{mc^2} \right), \quad (3.11)$$

therefore it increases much slower with the electron energy than in the Thomson regime. It is worth noticing that while the scattering rate decreases with energy, in the single encounter the electron loses a significant fraction of its initial energy. Even though generally this process should be catastrophic, nonetheless it is possible to obtain analytical fits for the energy losses in the whole energy range and treat them as continuous with an accuracy better than 20% (Khangulyan & Aharonian, 2005).

The loss time scale, that can be evaluated as $\tau_L \simeq E/(|dE/dt|)$, is:

$$\tau_L \propto E(\ln E)^{-1} \quad (3.12)$$

increasing with the electron energy, opposite to the Thomson loss time which decreases as $\tau_L^T \propto E^{-1}$.

The last piece of information we need is the energy spectrum of the emitted photons. For an initial distribution $n(\epsilon)$, the photon spectrum resulting from the scattering of photons with initial energy $\epsilon \pm d\epsilon$ off the single electron is given by (Jones, 1968):

$$\frac{dN}{dt d\epsilon_1 d\epsilon} = \frac{3 \sigma_{TC} n(\epsilon)}{4 \gamma^2 \epsilon} \left[2q \ln q + (1 + 2q)(1 - q) + \frac{1}{2} \frac{\epsilon^2}{E(E - \epsilon)} (1 - q) \right], \quad (3.13)$$

where it is useful to define the variable

$$q = \frac{\epsilon_1}{\frac{4\epsilon\gamma}{mc^2}(\gamma mc^2 - \epsilon_1)}.$$

Eq. (3.13) is general and valid both in Thomson and Klein-Nishina regimes. Considering now a whole population of electrons with spectrum $f(\gamma)$, the total emitted power at a final photon energy ϵ_1 is given by:

$$\frac{dE_{tot}}{dt dV d\epsilon_1} = \int_{\gamma} \int_{\epsilon} \epsilon_1 f(\gamma) d\gamma \frac{dN}{dt d\epsilon_1 d\epsilon} d\epsilon. \quad (3.14)$$

In particular, in the Thomson limit, the term in brackets in Eq. (3.13) reduces to

$$h(\epsilon_1) = \frac{1}{4\gamma^2\epsilon} \left[2\epsilon_1 \ln \left(\frac{\epsilon_1}{4\gamma^2\epsilon} \right) + 4\gamma^2\epsilon + \epsilon_1 - \frac{\epsilon_1^2}{2\gamma^2\epsilon} \right]. \quad (3.15)$$

Dealing with high energy particles and in particular with shock accelerated particles, we are interested in the case of electrons whose distribution follows a power law $f(\gamma) \propto \gamma^{-\alpha}$. Substituting $f(\gamma)$ and Eq. (3.15) into Eq. (3.14), the integration leads to the well known result:

$$\frac{dE_{tot}}{dt dV d\epsilon_1} \propto \epsilon_1^{-p}, \quad (3.16)$$

with

$$p = \frac{\alpha - 1}{2}. \quad (3.17)$$

In the Thomson limit, a power law distribution of electrons produces a power law distribution of photons. In the case of DSA $\alpha = 2$ and $p = 0.5$.

This is no longer the case in the Klein-Nishina regime. Not only do we expect a harder spectrum for the radiation, due to the shallower dependence on energy of the

loss rate, but interestingly when losses take place at the same time as acceleration their non power law behaviour is expected to act also on the electron spectrum and modify it. The spectral region of key interest is the one around the cut-off energy. The peak of the emission is expected at the maximum energy, therefore an accurate description of the spectral features in this energy range (the one most strongly affected by losses) appears crucial.

Synchrotron emission arises when a charged particle moves in a magnetic field. The Lorentz force exerted by the field tends to bend the trajectory of the particle in the plane perpendicular to the magnetic field lines. The modulus of the velocity is unchanged, but the trajectory is modified and radiation is emitted. The process can be described by the same interaction we have just treated, under the condition of substituting the real photons of the radiation field with the virtual photons of the magnetic field. In a static uniform magnetic field and for a monoenergetic distribution of electrons, in complete analogy with the case of inverse Compton (see Eq. (3.8)), the energy loss rate is:

$$-\frac{dE}{dt} = \frac{4}{3}\sigma_T c \gamma^2 U_{mag}, \quad (3.18)$$

where now $U_{mag} = B^2/(8\pi)$ is the energy density of the magnetic field. To obtain Eq. (3.8) it was assumed that the photon distribution was isotropic. In the case of synchrotron radiation the condition translates in having a random distribution of directions of the electrons with respect to the magnetic field lines. The second assumption is that the Thomson limit is applicable. In an inertial frame where the electron is instantaneously at rest, the energy ϵ'_1 of the emitted photon is connected to the gyration frequency ω'_c of the electron by $\epsilon'_1 \simeq \hbar\omega'_c = \hbar eB'/(mc)$. Ignoring the angle between the magnetic field lines and the velocity of the electron, we can rewrite ϵ'_1 in term of the magnetic field in the lab frame as $\epsilon'_1 \simeq \gamma\hbar eB/(mc)$.

In analogy with the inverse Compton case, the Thomson condition is given by $\epsilon'_1/mc^2 \ll 1$, which translates into the lab frame in

$$\frac{\gamma}{mc^2} \frac{\hbar eB}{mc} \ll 1. \quad (3.19)$$

The above equation can be rewritten in a more handy way by defining a critical

magnetic field value $B_{cr} = m^2 c^3 / (\hbar e) \simeq 4 \times 10^{13}$ G:

$$\gamma \left(\frac{B}{B_{cr}} \right) \ll 1. \quad (3.20)$$

The above condition is verified in all the situations we are interested in. Indeed the equivalence $\gamma \left(\frac{B}{B_{cr}} \right) = 1$ can be rewritten in terms of the electron energy E as:

$$EB = mc^2 B_{cr} \simeq 2 \times 10^7 \text{ TeV G}, \quad (3.21)$$

which implies electron energies of order 10^{15} TeV for a microGauss field, or conversely magnetic field of $\sim 10^5$ G for 100 TeV electrons.

To obtain the energy of the emitted photon in the lab frame we use Eq.(3.5) and obtain:

$$\epsilon_1 \simeq \gamma^2 \left(\frac{B}{B_{cr}} \right) mc^2. \quad (3.22)$$

We can define a critical energy ϵ_c for our assumption of monoenergetic isotropic distribution of electrons as:

$$\epsilon_c = \frac{3}{2} \hbar \gamma^2 \frac{eB}{mc}. \quad (3.23)$$

The emitted power spectrum is obtained by evaluating the retarded electric field obtained by the Liénard-Wiechart potentials. Here we report only the final result (Rybicki & Lightman, 1979):

$$\frac{dE}{dt d\epsilon_1} = \frac{\sqrt{3} e^3 B}{hmc^2} K(x), \quad (3.24)$$

with $x = \epsilon_1 / \epsilon_c$; $K(x)$ is referred to as the kernel function and it is plotted in Fig. 3.2. $K(x)$ is strongly peaked around the value 0.29, therefore the peak frequency being $\nu_{peak} = 0.29\nu_c$, and has asymptotic expressions:

$$\begin{cases} K(x) \propto x^{1/3}, & x \ll 1 \\ K(x) \propto x^{1/2} e^{-x}, & x \gg 1. \end{cases} \quad (3.25)$$

For a generic energy distribution of electrons $f(\gamma)$, still assumed isotropic, the total emitted power at an energy ϵ_1 is obtained by integrating Eq. (3.24) over $f(\gamma)$:

$$\frac{dE_{tot}}{dt dV d\epsilon_1} = \frac{\sqrt{3} e^3 B}{hmc^2} \int d\gamma f(\gamma) K(x). \quad (3.26)$$

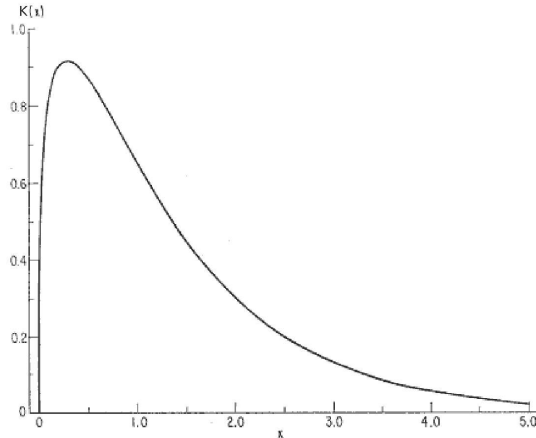


Figure 3.2: Plot of the kernel function $K(x)$ for synchrotron emission as a function of $x = \epsilon_1/\epsilon_c$, with ϵ_1 the energy of the emitted photon and ϵ_c the synchrotron critical energy. Figure from Blumenthal & Gould (1970).

As in the IC case, we are interested in the photon spectrum resulting from a power law distribution of electrons $f(\gamma) \propto \gamma^{-\alpha}$. Remembering that $x = \epsilon_1/\epsilon_c$ and that $\epsilon_c \propto \gamma^2$, the emitted spectrum in this case is given by:

$$\frac{dE_{tot}}{dt dV d\epsilon_1} \propto \epsilon_1^{-p} \int dx K(x) x^{(\alpha-3)/2}, \quad (3.27)$$

with the same slope given in Eq. (3.17).

3.2 Proton-photon Interactions

We have just described the interaction of a charged particle with a photon field (either real or virtual) via inverse Compton and synchrotron processes. The same equations we have written for electrons apply to protons, once substituted m_e with m_p . But, exactly for the difference in mass between the two particles, the energy loss rate of IC and synchrotron radiation for a proton is suppressed by a factor $(m_e/m_p)^4$, making it generally negligible.

The presence of the Cosmic Microwave Background radiation homogeneously filling the space, though, can provide two different channels that limit acceleration,

namely photonpair and photopion production:

$$\begin{aligned} p + \gamma &\rightarrow p + e^+ + e^- \\ , p + \gamma &\rightarrow N + \pi. \end{aligned} \quad (3.28)$$

The first process is also known as Bethe-Heitler process (Bethe & Heitler, 1934) and it has been discussed in detail for the case when a relativistic proton impacts on a soft photon by Blumenthal (1970); Chodorowski et al. (1992). For the second process we refer to Stecker (1968); Berezinsky & Grigoreva (1988); Mücke et al. (2000); Kelner & Aharonian (2008). We keep these authors as reference.

In order for the processes to take place, the centre of mass (CM) energy of the interaction has to be greater than the threshold for the formation of the final products which is of the order of their rest mass. To obtain the threshold energy, we focus on the pion production process. We neglect the difference in mass between charged and neutral pions as well as between proton and neutron. In the proton rest frame (all quantities primed) the four-momenta of incoming and outgoing particles are $P'_{p,i} = (mc, \vec{0})$, $P'_{ph} = (\epsilon'/c)(1, \vec{n}_{ph})$, $P'_{p,f}$ and P'_π , where \vec{n}_{ph} is the unity vector in the incoming direction of the photon. The conservation of momentum and energy reads:

$$P'_{p,i} + P'_{ph} = P'_{p,f} + P'_\pi \quad (3.29)$$

and is a Lorentz invariant, so as the scalar product. Therefore the quantity:

$$(P'_{p,i} + P'_{ph})^2 = (P'_{p,f} + P'_\pi)^2 \quad (3.30)$$

is a Lorentz invariant as well. It is convenient to express the right hand term in the centre of mass frame (all quantities starred):

$$(P'_{p,i} + P'_{ph})^2 = (P^*_{p,f} + P^*_\pi)^2. \quad (3.31)$$

By definition, at the threshold the products of the interaction in the CM frame are at rest, giving:

$$(m_p + P'_{ph})^2 = (m_p + m_\pi)^2, \quad (3.32)$$

from which we derive the threshold energy of the photon in the proton rest frame:

$$\epsilon'_{th} = m_\pi \left(1 + \frac{m_\pi}{2m_p} \right) \simeq 145 \text{ MeV}. \quad (3.33)$$

In the lab frame it translates into a proton threshold energy:

$$E_{th} = \frac{m_\pi m_p}{2\epsilon} \left(1 + \frac{m_\pi}{2m_p} \right) \simeq 7 \times 10^{16} \frac{1}{\epsilon_{eV}} \text{ eV}, \quad (3.34)$$

where ϵ_{eV} is the energy of the photon in the lab frame in eV and we have assumed head on collisions between the proton and the photon to obtain the minimum energy possible for the proton. For the pair production we can adopt the same formulae just by substituting m_π with $m_{e^+} + m_{e^-} = 2m_e$. Eq. (3.33) and (3.34) give the values $\epsilon'_{th} \simeq 1 \text{ MeV}$ and $E_{th} \simeq 5 \times 10^{14}/\epsilon_{eV} \text{ eV}$. In particular, for the CMB the mean photon energy is $\epsilon \simeq 6 \times 10^{-4} \text{ eV}$, so that the interaction channels open at proton energies:

$$E_{pair} \gtrsim 10^{18} \text{ eV}, \quad (3.35)$$

$$E_{pion} \gtrsim 10^{20} \text{ eV}. \quad (3.36)$$

The total energy loss rate of the proton is found by integrating over the initial spectrum of photons, all the possible incoming and outgoing angles and the cross-section of the process σ , including the inelasticity K , representing the amount of energy that the proton loses in every scattering with respect to its initial one. To have an estimate we can evaluate it at the threshold, resulting in $K_{th} \simeq m_f/m_p$, where m_f is the mass of the final particles produced. For the pair production $K_{th} \simeq 10^{-3}$ and for the single pion production $K_{th} \simeq 0.14$. The cross-section for pair production (also known as Bethe-Heitler cross-section) is bigger than for photomeson production, but due to the effect of inelasticity, once past the threshold energy for pion production, this process is dominant and pair production can be neglected. The general formula for the energy loss rate can be written as:

$$-\frac{dE}{dt} \propto \int d\epsilon \frac{n(\epsilon)}{\epsilon^2} \int d\epsilon' \epsilon' \sigma(\epsilon') K(\epsilon'). \quad (3.37)$$

In the second integral the cross-section is intended as already integrated over the final product energies and angles and the integral over the initial angle of the photon can be transformed into an energy integral remembering the relation $\epsilon' = \gamma\epsilon(1 - \cos\theta)$ (Eq. (3.1) with $\beta \simeq 1$). The energy loss time scale is given by $\tau_L \simeq E/(dE/dt)$. For interaction with the CMB, we obtain the curves in Fig. 3.3 where τ_L is reported

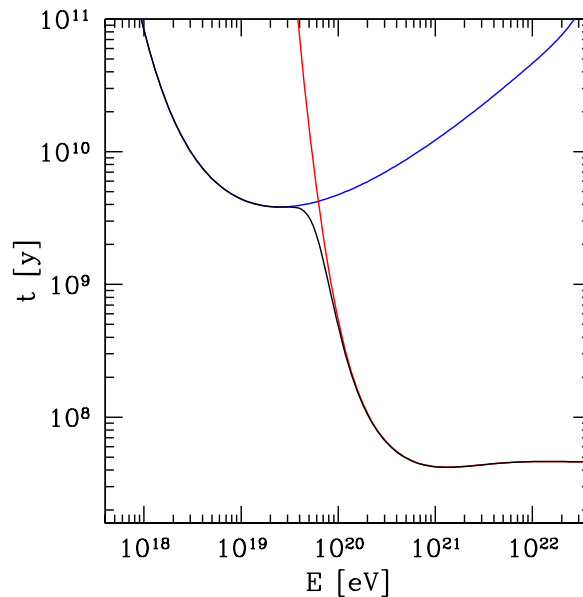


Figure 3.3: Time scales of pair (blue line) and pion production (red line) as well as their sum (black line) from protons scattering off the CMB as function of the proton energy.

as a function of the initial proton energy. The blue line refers to pair production, the red one to pion production and the black line is the total. We evaluated the corresponding threshold energies for the CMB peak energy in Eq. (3.35) and (3.36). Since the photons are not strictly monoenergetic the threshold is in fact broadened and the process starts at energies lower than those in the mentioned equations. Pion production becomes quickly the dominant process once passed the threshold energy, so that pair production is relevant in a relatively narrow energy range. Nonetheless this process can be extremely interesting for the following reason: through the interaction with photons, protons produce particles that can travel to us, namely photons and neutrinos. The pions formed decay rapidly through the main channels:

$$\begin{aligned} \pi^+ (\pi^-) &\rightarrow \mu^+ (\mu^-) + \nu_\mu (\bar{\nu}_\mu) \rightarrow e^+ (e^-) + \nu_e (\bar{\nu}_e) + \nu_\mu (\bar{\nu}_\mu) + \bar{\nu}_\mu (\nu_\mu), \\ \pi^0 &\rightarrow 2\gamma, \end{aligned} \quad (3.38)$$

so that the final stable products are gamma-rays, electron and positrons, and neutrinos. But neutrinos are extremely challenging to detect and the pion produced gamma-rays have such a high energy that they undergo significant absorption. On the other hand, the electrons produced by pair production and the decay of charged

pions can provide a better means of detection by emitting broad band radiation via synchrotron and IC.

The spectra of the final products of proton-photon interaction can be written as (Kelner & Aharonian, 2008):

$$\frac{dN}{dE} \propto \int \int \frac{dE_p}{E_p^2} f_p(E_p) f_{ph}(\epsilon) \Phi \left(\epsilon, \frac{E}{E_p} \right), \quad (3.39)$$

where E_p is the initial energy of the protons, $f_p(E_p)$ their distribution function and $f_{ph}(\epsilon)$ the initial photon spectrum. The function Φ represents the energy distribution of the particular class of particles we are interested in (photons or leptons of the different species). The values of such functions have been derived by Monte Carlo simulations using the code SOPHIA (Mücke et al., 2000) and recently analytically fitted by Kelner & Aharonian (2008).

3.3 Including Energy Losses in DSA, the Status of the Art

When facing the problem of describing the non-thermal radiation observed in astrophysical objects, it is common procedure to take as a starting point a given spectrum of the accelerated particles responsible for producing such a radiation. In particular, for simplicity an exponential cut-off is usually assumed at the high energy end of the spectrum. In the most common approach, shock acceleration is the assumed acceleration process, therefore the particle spectrum is taken of the form:

$$f_{inj}(E) = kE^{-2} \exp(-E/E_0), \quad (3.40)$$

where the cut-off energy E_0 is estimated from the parameters of the system (see Section 2.4). The effect of losses is taken into account by solving the continuity equation (see e.g. Blumenthal & Gould (1970)):

$$\frac{\partial f(E)}{\partial t} + \frac{\partial}{\partial t} \left(\frac{dE}{dt} f(E) \right) = f_{inj}(E) \quad (3.41)$$

in the steady state limit $\partial f(E)/\partial t = 0$. The final spectrum for the particles is given by:

$$f(E) = \frac{1}{dE/dt} \int_E^\infty f_{inj}(E') dE'. \quad (3.42)$$

Once obtained the cooled spectrum of particles $f(E)$, the distribution of photons is derived from the formulae we presented in this Chapter. The approach just described is useful to estimate the basic emission characteristics, but the assumed shape of the cut-off is totally arbitrary. Moreover, Eq. (3.42) is suitable only if acceleration and energy losses do not happen in the same region. On the other hand, the correct particle spectrum can only be derived from the self-consistent treatment of the acceleration process coupled with energy losses.

To appropriately take into account the presence of energy losses, an additional term has to be included in the transport equation for accelerated particles (Eq. (2.52)), that now reads:

$$\begin{aligned} \frac{\partial f(x, p, t)}{\partial t} + u \frac{\partial f(x, p, t)}{\partial x} - \frac{\partial}{\partial x} \left(D(x, p) \frac{\partial f(x, p, t)}{\partial x} \right) - \frac{p}{3} \frac{\partial u}{\partial x} \frac{\partial f(x, p, t)}{\partial p} \\ - \frac{1}{p^2} \frac{\partial}{\partial p} (p^2 L(x, p) f(x, p, t)) = Q(x, p), \end{aligned} \quad (3.43)$$

where $L(x, p)$ is the absolute value of the energy loss rate as a function of momentum and space.

For high energy electrons, synchrotron and inverse Compton losses are generally responsible for determining the maximum acceleration energy. Indeed the first attempts to self-consistently model this effect date shortly after the first appearance of Diffusive Shock Acceleration theory in 1978. Bulanov & Dogiel (1979) obtain approximate analytical expressions for the particle spectrum by inserting the energy loss term in the transport equation. However their approach presents several limitations: the diffusion coefficient D is assumed to be constant both in space and energy and the calculation is explicitly restricted to synchrotron losses.

Under similar constraints an exact analytical treatment of the problem is possible and was presented by Webb et al. (1984). The steady state transport equation is solved but the resulting analytical expression for the particle spectrum is only

achievable in the case of synchrotron losses and uniform energy independent diffusion coefficient. In an early attempt to solve the problem in a more general form, we followed the approach presented by these authors. Keeping both the energy dependence of the diffusion coefficient and of the energy loss term general, the problem requires numerical integration. We realised that the calculation, even though in principle possible, requires a substantial coding effort and presents various computational problems, due to the fact that, even though well posed mathematically, the problem presents several numerical singularities; moreover the flexibility in terms of energy range becomes very limited. In addition the obtained spectrum is strictly steady state, while a time dependent calculation is necessary to model some classes of objects of interest, like Supernova Remnants or Microquasar, as we show in Chapter 5. For all the above reasons we dismissed this approach and decided to carry out a fully numerical time dependent calculation.

A similar model to the one of Webb et al. (1984) is presented in Heavens & Meisenheimer (1987), but with the same limitations just pointed out.

We mention that a different approach to the problem in the frame of the so-called box model has also been proposed by Drury et al. (1999), but, as pointed out by Kirk (2001), the assumptions of the model fail exactly in the cut-off region, making this approach not suited for study of the spectrum around the maximum energy.

Recently, Zirakashvili & Aharonian (2007) presented a numerical solution for an arbitrary momentum dependence of the diffusion coefficient. The authors obtain also very accurate analytical fits to the numerical solution. They explicitly limit themselves, though, to synchrotron losses. Interestingly, the resulting particle spectrum is shown to have a super exponential cut-off even in this simple case, hinting to the fact that more complex spectra than the one in Eq. (3.40) have to be expected when energy losses take place during the acceleration process.

While efforts have been repeatedly made to model synchrotron emission from shock accelerated electrons, a similar treatment for IC losses in the Klein-Nishina regime is missing. The reason may be two-sided: on the one hand the bigger difficulty due to the more complex form of the loss term did not encourage a deep study

on a phenomenon that would interest very high energy emission (gamma-rays), since, on the other hand, very little observational material was available until recent years in this energy band. The situation has since changed, however, with extremely successful observational campaigns being carried out and gamma-ray astronomy being now a well-established field. The last five years have shown the crucial importance of detailed modelling of high energy radiation spectra in order to try to disentangle the different scenarios between leptonic and hadronic emission, to put better constraints on the parameters in the sources, and not least to test our models and with them our present understanding of the physics involved in high energy phenomena. Correct modelling of IC in the Klein-Nishina regime is interesting because the very different shape of the losses, as compared to Thomson regime, suggest a consequent strong modification of the expected particle spectrum.

Concerning protons, we see in Fig. 3.3 that energy losses become relevant at very high energies and on time scales of the order of Gyr (if the CMB is the main target radiation). These are the conditions present in large scale structures. As we mentioned in Chapter 1, clusters of galaxies represent a closed box for accelerated protons that remain confined there for a Hubble time (Berezinsky et al., 1997; Völk et al., 1996). Norman et al. (1995) and Kang et al. (1996) have pointed out the importance, in this case, of proton-photon energy losses in determining the maximum energy of the accelerated protons, but in those works a self-consistent calculation of the resulting spectrum has not been attempted and the simple approximation in Eq. (3.40) was adopted. A more refined version of the box model has been applied to this case by Protheroe (2004). The resulting proton spectrum presents interesting features like the appearance of a pile up around the cut-off energy, however the method presents the limitations discussed for box models. Moreover, we show in Chapter 6 that a time dependent calculation is needed in this case. If energy losses become the limiting mechanism for acceleration, we expect a relevant portion of the proton energy to be transferred to secondary particles and eventually to non-thermal radiation whose spectrum will reproduce the spectral features of the parent particles. Therefore an accurate modelling of the process is required.

In the next Chapter we present our numerical method that includes energy losses

into shock acceleration in a very general way, without any constrain on the shape of the loss term or on the energy and spacial dependence of the diffusion coefficient.

Chapter 4

The Model

We present in this Chapter our numerical method to include the presence of energy losses into the model of Diffusive Shock Acceleration.

In order to make this approach simpler, we report here only the key points of the calculation. The rigorous (but tedious) mathematical details are found in the Appendix.

As mentioned in Section 3.3, to take into account the presence of energy losses during the process of shock acceleration, an additional term has to be added in the transport equation for accelerated particles (Eq. (2.52)). We consider a plane parallel shock, where the fluid moves (in the shock rest frame) along the x -axis from $-\infty$ far upstream, to $+\infty$ far downstream and the shock is located at $x = 0$. The quantities upstream are always identified with the subscript 1 and those downstream with the subscript 2. We assume the velocity of the shock to be non-relativistic. The transport equation for the particles distribution function reads (we rewrite it here for convenience):

$$\begin{aligned} \frac{\partial f(x, p, t)}{\partial t} + u \frac{\partial f(x, p, t)}{\partial x} - \frac{\partial}{\partial x} \left(D(x, p) \frac{\partial f(x, p, t)}{\partial x} \right) - \frac{p}{3} \frac{\partial u}{\partial x} \frac{\partial f(x, p, t)}{\partial p} \\ - \frac{1}{p^2} \frac{\partial}{\partial p} (p^2 L(x, p) f(x, p, t)) = Q(x, p), \end{aligned} \quad (4.1)$$

where $L(x, p) = -dp/dt$ is the energy loss rate taken to be positive and we always

assume $p = E/c$. $Q(x, p)$ is the injection term and u represents the bulk velocity of the plasma in the shock rest frame. We assume that the diffusion coefficient up and downstream $D_{1,2}$ does not depend on x and has the following functional form in each region:

$$D(p) = D_0 p^\epsilon \quad (4.2)$$

(but any expression for $D_{1,2}(x, p)$ can be easily implemented in the code) and that injection happens at the shock surface as a delta function in energy:

$$Q(x, p) = Q_0 \delta(x) \delta(p - p_0). \quad (4.3)$$

The formulation is general so that it can be applied to both protons or electrons, plugging in the relevant energy loss channels, namely proton-gamma interactions for the hadronic channel, synchrotron and inverse Compton emission for the leptonic one. For what concerns the background radiation field, we assume it to be isotropic. We also assume that the background magnetic field has a constant value in the upstream and downstream region and the two are related by $B_2 = \xi B_1$, where ξ is the compression factor due to the presence of the shock. In accordance with Eq. (2.22) that gives the jump conditions of the magnetic field at the shock, such a parameter varies between two values: $\xi = 1$ for a pure parallel shock and $\xi = 4$ for a perpendicular shock. Under the above assumptions the loss term $L_{1,2}(p)$ up and downstream is independent of x .

4.1 The Numerical Method

As appropriate for a diffusive equation, we solve Eq. (4.1) using a finite difference numerical scheme fully implicit in space and semi-implicit in momentum. This choice implies a total independence of the time stepsize from the space one, allowing us more freedom in the time grid. Our calculation is time dependent, we look for the steady state solution by running the code until the solution converges to its equilibrium (time independent) value.

In order to solve the problem we need to insert the boundary conditions at the shock location and at upstream/downstream infinity. At the shock we impose the

standard matching condition $f_1(0, p) = f_2(0, p) \equiv f_0$. To evaluate f_0 we consider again Eq. (4.1) and integrate it between 0_- immediately upstream and 0_+ immediately downstream, obtaining:

$$\frac{1}{3}(u_1 - u_2)p \frac{\partial f_0}{\partial p} = D_2 \frac{\partial f_0}{\partial x} \Big|_2 - D_1 \frac{\partial f_0}{\partial x} \Big|_1 + Q_0 \delta(p - p_0). \quad (4.4)$$

At infinity up and downstream we set $f(x, p) = 0$. We discuss this point in more detail in the following.

It is convenient, in order to perform the numerical integration, to introduce two dimensionless variables in place of p and x . The first variable is p/p^* , where p^* is a parameter that estimates the cut-off momentum for the electron distribution¹. It is evaluated imposing equilibrium between the momentum gain and the momentum loss in one acceleration cycle, as in Eq. (2.64):

$$\Delta p_{acc} = \Delta p_{loss}. \quad (4.5)$$

The momentum gained is given by:

$$\Delta p_{acc} = \frac{4p(u_1 - u_2)}{3c} \quad (4.6)$$

and the momentum lost is:

$$\Delta p_{loss} = L_1(p)\Delta t_1 + L_2(p)\Delta t_2, \quad (4.7)$$

where the mean residence time in the up and downstream regions is $\Delta t_{1,2} = 4D_{1,2}(p)/cu_{1,2}$ (see Eq. (2.60)).

For the spatial coordinate we operate a change of variable both up and downstream. To reduce the large range in $|x|$ from 0 to ∞ to a more numerically feasible one, we use an exponential variable:

$$z = \exp \left[-\frac{|x|}{x_0} \right], \quad (4.8)$$

¹In fact the cut-off momentum is calculated self-consistently and can be different from p^* . The latter represents a parameter, whose value is close to the cut-off momentum and that we adopt for convenience to normalise the momentum variable.

where x_0 is a characteristic length scale. The new variable now conveniently ranges from 0 to 1. In the upstream region, except for energies close to the cut-off where losses become important, the spectrum is given by Eq. (2.54). The accelerated particles can propagate for a distance of the order of one diffusion length $D(p)/u_1$ ahead of the shock. At higher distances the distribution of particles goes to zero exponentially. On the other hand in the downstream region all particles are eventually advected away from the shock with the same velocity u_2 . The distribution function is $f_2(p) = f_0(p)$ (Eq. (2.55)) up to a maximum distance. The distance to which particles can actually propagate is determined, in the steady state, by their loss length given for each particle by $x_L(p) = u_2\tau_L(p)$, where $\tau_L(p) = p/L(p)$ is the loss time scale. At length scales bigger than x_L the distribution function goes to zero. We note that this discussion justifies our boundary assumptions at infinity. A reasonable choice for the length scale x_0 is:

$$x_{0,1} = \frac{D_1(p)}{u_1} \quad (4.9)$$

and

$$x_{0,2} = u_2\tau_L, \quad (4.10)$$

for upstream and downstream, respectively.

Once the solution $f(x, p)$ of Eq. (4.1) is found, we evaluate the total spectrum integrated over space, $F(p) = \int f(x, p)dx$, which is the quantity required to evaluate the radiation spectrum emitted in the shock region.

In order to check our calculation, we tested it against the analytical fits given in Zirakashvili & Aharonian (2007) in the simple case of electrons undergoing pure synchrotron losses.

Following these authors, we choose a compression ratio $r = 4$, valid for strong shocks, and $\xi = \sqrt{11}$, appropriate for a completely randomised magnetic field. The spectrum at the shock can be fit by the expression:

$$f_0(p) \propto \left(\frac{p}{\hat{p}}\right)^{-4} \left[1 + 0.523 \left(\frac{p}{\hat{p}}\right)^{9/4}\right]^2 \exp(-p^2/\hat{p}^2), \quad (4.11)$$

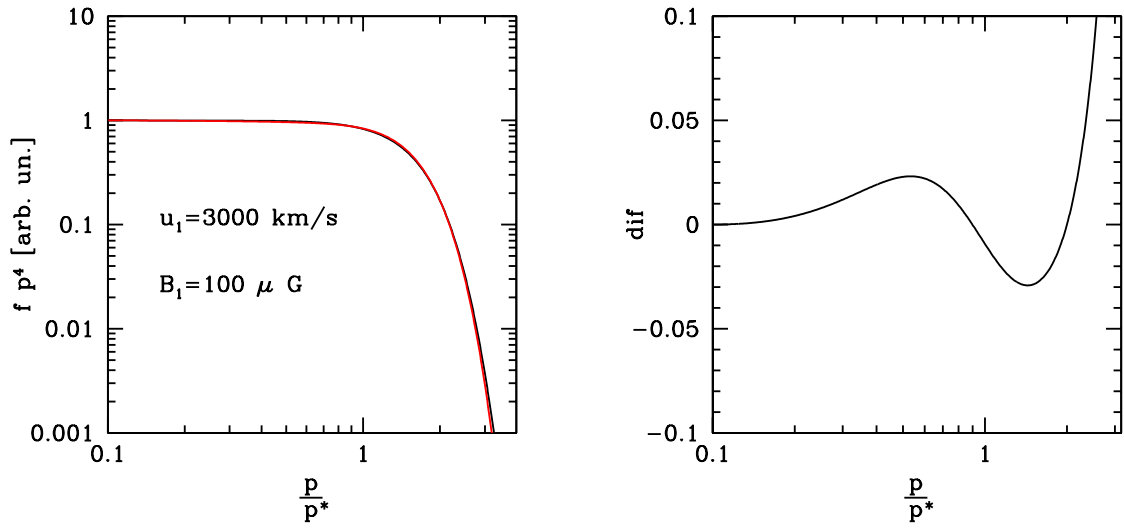


Figure 4.1: **a)** Comparison between our numerical calculation (black curve) and the analytical fit given by Zirakashvili & Aharonian (2007) (red curve) for the electron distribution at the shock. The values of the parameters are: $u_1 = 3000$ km/s, $B_1 = 100 \mu\text{G}$, $B_2 = \sqrt{11}B_1$ and $r = 4$. **b)** Percentage difference between the curves in panel **a**.

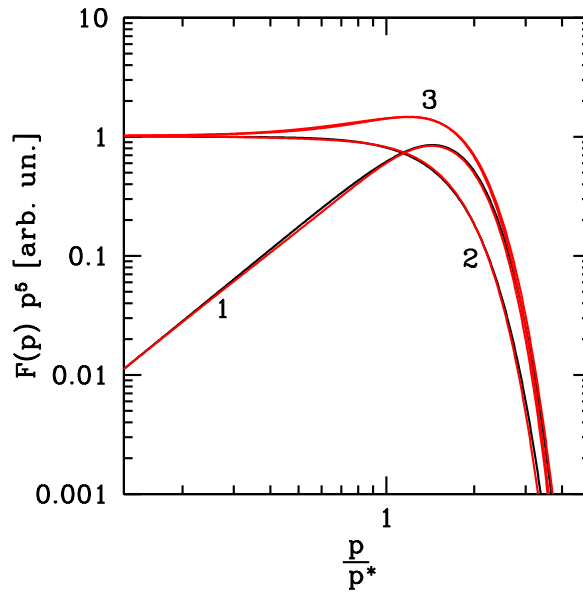


Figure 4.2: Same as in Fig. 4.1 for the spatially integrated spectra. Curve 1 is the upstream contribution, curve 2 is the downstream one and curve 3 is the sum of the two.

where \hat{p} is:

$$\hat{p} = \frac{2.86 \times 10^8}{(1 + \xi^{-1/2})} \frac{mc(r - 1)}{3r} \left(\frac{u_1}{3000 \text{ km/s}} \right) \left(\frac{B}{100 \mu\text{G}} \right)^{-1/2} \quad (4.12)$$

for Bohm diffusion. In Fig. 4.1a we show the comparison with our calculation for $u_1 = 3000 \text{ km/s}$ and $B = 100 \mu\text{G}$. The black curve represents our calculation and the red one the analytical fit, the normalisation is arbitrary. The two curves are in agreement within a 3% level of accuracy up to $p \simeq 2p^*$.

The same result is obtained for the integrated spectra $F(p)$. In Fig. 4.2 our spectra upstream (curve 1), downstream (curve 2) and the sum of the two (curve 3) are shown in black. In red are the analytical fits.

Chapter 5

Electron Acceleration Under Dominant IC Losses

In the last Chapter we presented our method to calculate self-consistently the spectrum of accelerated particles in the presence of severe energy losses. The present and following Chapters are dedicated to our results and their application to astrophysical objects.

Here we focus on the acceleration of electrons in the case where the accelerator is embedded in a strong radiation field, characterised by an energy density much bigger than that of the magnetic field. Under this circumstance, inverse Compton losses dominate over synchrotron losses and, at the highest energies, modifications to the electron spectrum are expected, with respect to the case of synchrotron/Thomson losses, due to the transition between Thomson and Klein-Nishina regimes. This, in turn, strongly affects the spectrum of the radiation emitted by accelerated particles. We calculate numerically the exact shape of the spectrum in the whole energy range and we show that in the case of Klein-Nishina losses the particle distribution at the shock has a broad cut-off, due to the shallow energy dependence of the loss rate. Another important effect of Klein-Nishina losses is to harden the downstream electron spectrum close to the maximum energy, leading to the formation of a pronounced pile up. Such a feature can be observed in the photon spectrum,

in particular for synchrotron emission. The effect on the inverse Compton emission is less pronounced due to the fact that the Klein-Nishina cross-section intervenes twice, in opposite directions, to harden the electron spectrum and to soften the photon one leading to an almost exact compensation.

In order to obtain the electron energy spectrum for the case of interest, we need to insert the appropriate energy loss rates $L(p)$ corresponding to synchrotron and IC emission (as discussed in Chapter 3) in Eq. (4.1). The missing piece of information in the model is the diffusion coefficient of particles close to the shock, which determines the acceleration rate. For a given diffusion coefficient, the problem is well defined and can be solved once the value of the magnetic field and the spectrum of the ambient radiation are specified. Although the value of this coefficient remains uncertain, as mentioned in Chapter 2 it is expected that, due to the high level of turbulence present close to the shock, the mean free path of a particle is of the order of its Larmor radius r_L . Under these circumstances diffusion proceeds close to the slowest possible (Bohm) rate with diffusion coefficient $D \sim r_L c/3$. Recalling Eq. (4.2), this corresponds to:

$$\begin{cases} D_0 = c^2/(3eB) \\ \beta = 1 . \end{cases} \quad (5.1)$$

5.1 Photon Spectra

Once we have the electron spectrum we can calculate the spectra of the radiation emitted both via synchrotron and IC.

According to Eq. (3.26), for synchrotron radiation the energy flux at an energy ϵ is given by:

$$\Phi(\epsilon) = \frac{\sqrt{3}Be^3}{hmc^2} \int p^2 dp F(p) K(\epsilon/\epsilon_c). \quad (5.2)$$

where the critical energy (Eq. (3.23)) can be written as $\epsilon_c = \hbar 3eBp^2/(2m^3c^3)$ and we always assume $p = \gamma mc$. In our case $F(p)$ is the total electron spectrum integrated along the direction of propagation of the shock up and downstream. The exact expression for the kernel function $K(\epsilon/\epsilon_c)$ in the case of a turbulent magnetic field is derived in Crusius & Schlickeiser (1986). With several percent accuracy this can

be approximated by the analytical expression obtained in Zirakashvili & Aharonian (2007):

$$K(\epsilon/\epsilon_c) = \frac{1.81e^{-\epsilon/\epsilon_c}}{\sqrt{(\epsilon/\epsilon_c)^{-2/3} + (3.62/\pi)^2}}. \quad (5.3)$$

We adopt this simpler expression.

The inverse Compton energy flux for an isotropic distribution of soft photons $n(\epsilon')$ upscattered by a population of electrons with spectrum $F(p)$ is (compare to Eq. (3.13) and (3.14)):

$$\Phi(\epsilon) = \frac{2\pi e^4 \epsilon}{c} \int dp F(p) \int \frac{n(\epsilon') d\epsilon'}{\epsilon'} \left[2q \ln q + (1 + 2q)(1 - q) + \frac{1}{2} \frac{\epsilon^2}{pc(pc - \epsilon)} (1 - q) \right]. \quad (5.4)$$

For simplicity, in the following we assume that the background radiation field is a black body, but the calculations can be easily extended to any background radiation spectrum. Depending on the environment we want to model, we consider either a single or a superposition of multiple Planck distributions, introducing a dilution factor η for each of them:

$$n(\epsilon') = \eta \frac{1}{\pi^2 \hbar^3 c^3} \frac{\epsilon'^2}{e^{\epsilon'/kT} - 1}, \quad (5.5)$$

where k is the Boltzmann constant and T the black body temperature.

5.2 Results

We present here the results of our calculation by means of an ideal case in order to illustrate the features and characteristics of the problem we are studying.

We consider a non-relativistic shock expanding in a medium where the magnetic field value is $B_1 = 10 \mu\text{G}$. For such a field, the magnetic energy density is $B^2/8\pi = 2.5 \text{ eV/cm}^3$. In order to keep the number of parameters low, in this example we assume the same value of the magnetic field upstream and downstream (i.e. $\xi = 1$). In the next section, when we apply our results to astrophysical objects, we will include the compression of the magnetic field at the shock. We assume that the accelerator is embedded in an isotropic background radiation field. We

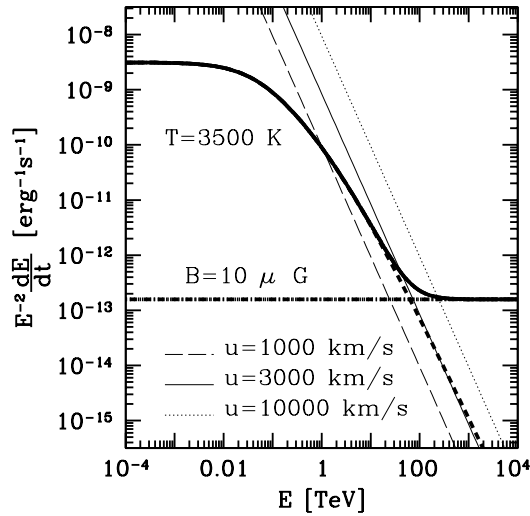


Figure 5.1: Energy loss rates and shock acceleration rates for a magnetic field $B = 10 \mu\text{G}$ and a diluted black body radiation field at a temperature $T = 3500 \text{ K}$. All curves have been multiplied by E^{-2} so that Thomson losses correspond to horizontal lines. Thick lines: synchrotron loss rate (dot-dashed), inverse Compton loss rate (dashed) and the sum of the two (solid). Thin curves: acceleration rates for $u_1 = 1000 \text{ km/s}$ (dashed), $u_1 = 3000 \text{ km/s}$ (solid) and $u_1 = 10000 \text{ km/s}$ (dotted).

further assume a diluted black body radiation spectrum (i.e. with a reduced energy density) at a temperature of $kT = 0.3 \text{ eV}$ (i.e. in the Near Infrared energy band), corresponding to $T = 3500 \text{ K}$. We then assume the radiation energy density to be $U_{rad} = 5 \times 10^4 \text{ eV/cm}^3$, a factor 2×10^4 larger than the magnetic one (as we will point out in the next section, this high value is similar to the one measured in the $\leq 1 \text{ pc}$ Galactic Centre region (Davidson et al., 1992)).

In Fig. 5.1 we plot the energy loss rates due to synchrotron losses in a magnetic field of $10 \mu\text{G}$ (thick dot-dashed line) and inverse Compton scattering off a radiation field at 3500 K (thick dashed curve), as a function of the particle energy. The sum of the two is represented by the thick solid curve. Also plotted in Fig. 5.1 are the acceleration rates for DSA in the same magnetic field and for three different values of the shock velocity ($u_1 = 1000 \text{ km/s}$, dashed line, $u_1 = 3000 \text{ km/s}$, solid line, and $u_1 = 10000 \text{ km/s}$, dotted line). In this figure all curves have been multiplied by E^{-2} so that Thomson losses correspond to horizontal lines. The intersection between the acceleration rate curve and the total energy loss rate indicates the point in the

particle energy spectrum where the acceleration due to DSA is compensated by radiative losses and therefore the cut-off sets in.

Fig. 5.1 shows how the energy dependence of energy losses changes behaviour. At low energies ($E \ll (mc^2)^2/\epsilon_{ph}$), inverse Compton proceeds in the Thomson regime ($dE/dt \propto E^2$), but at high energies the losses enter the Klein–Nishina regime and the dependence of the process on energy changes ($dE/dt \sim \ln E$). At even higher energies synchrotron losses become dominant and an E^2 law for the loss rate is recovered.

We solve the transport equation for the accelerated electrons choosing the value of 3000 km/s for the shock velocity. For such a choice of parameters, losses proceed deep in the KN regime. The shock is assumed to be strong, i.e. compression ratio $r = 4$. In this example we make the assumption that the energy loss time scale is much shorter than any other time scale in the system that could limit acceleration, at all the energies we consider. Therefore we look for the steady state spectrum. The resulting electron energy spectrum at the shock location is shown in Fig. 5.2a (solid line). The dashed line, instead, shows the spectrum expected for the same values of the parameters but suppressing the radiation energy density (i.e. when synchrotron losses dominate). For an easier comparison we rescaled the momentum scale for each curve to its cut-off value p^* . Of course the actual value of p^* is different in the two cases. Note that the normalisation on the y -axis is in arbitrary units. The solid curve shows that the shape of the spectrum is modified by the decrease of the IC cross-section at high energies: the cut-off region is broader and the decay is shallower, compared to the synchrotron case. The result may be most easily understood from the rates in Fig. 5.1, which highlight the weak dependence on energy of Klein-Nishina losses.

To obtain the overall radiation produced by this population of electrons we have to consider the spatially integrated spectra $F_1 = \int_{-\infty}^0 f(x, p) dx$ and $F_2 = \int_0^{\infty} f(x, p) dx$. Fig. 5.2b shows the total spectrum $F(p) = F_1(p) + F_2(p)$ resulting from the integration for both cases of IC dominant losses (solid line) and of synchrotron dominant losses (dashed one). As can be seen, the most pronounced feature appears in the integrated spectrum: the softer dependence on energy of the

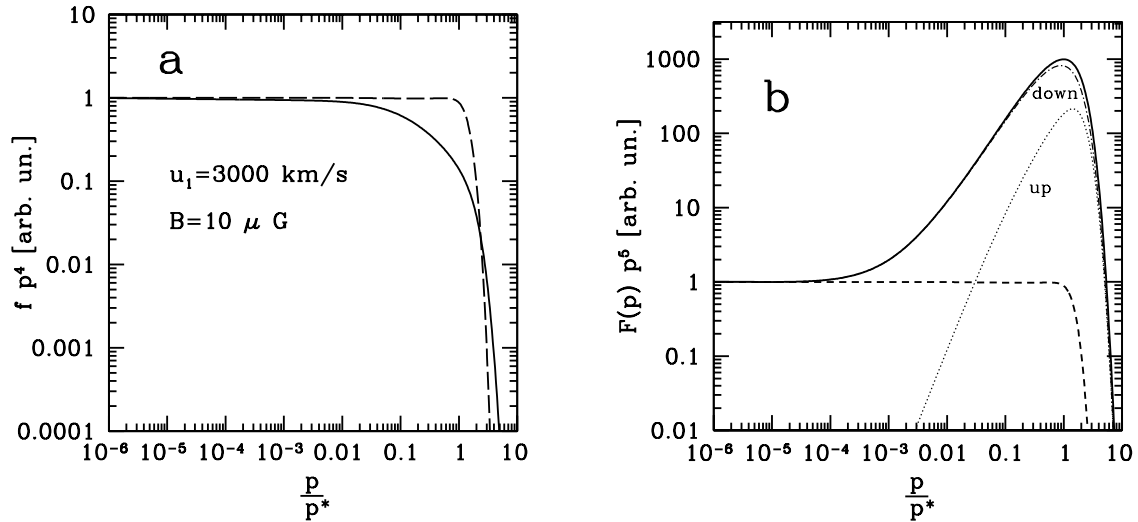


Figure 5.2: **a)** Electron spectrum at the shock location in the case of inverse Compton dominated losses (solid line) and synchrotron cooling dominated case (dashed line) for a magnetic field $B = 10 \mu\text{G}$ equal up and downstream, shock velocity $u_1 = 3000 \text{ km/s}$ and compression ratio $r = 4$. The background radiation field is assumed to be a diluted black body at $T = 3500 \text{ K}$ with energy density $U_{rad} = 5 \times 10^4 \text{ eV/cm}^3$. The momentum scale for each curve is normalised to the parameter p^* , calculated as in Section 4.1. The normalisation on the y -axis is in arbitrary units. **b)** Electron distributions integrated over space. In the case of the IC dominated case (solid line) we also show separately the two components upstream (dotted) and downstream (dash-dotted). The dashed line represents the synchrotron dominated case.

energy loss rate in the KN regime, as compared to the Thomson regime, causes a significant pile up around the cut-off energy (solid curve). For this case, we plotted also the upstream (dotted line) and downstream (dot-dashed line) distributions separately to show that the major contribution to the total spectrum is provided by the downstream distribution. In this region all particles are eventually advected away from the shock with the same velocity u_2 . As discussed in Chapter 4, the maximum distance from the shock they can reach is approximately their loss length $x_L = u_2 \tau_L$ (while upstream it is essentially determined by diffusion). For Thomson scattering $\tau_L \propto E^{-1}$, determining that the higher the particle energy the smaller the distance it can travel away from the shock before losing its energy. For this reason the integrated spectrum in momentum space downstream is $\propto p^{-\alpha-1}$. In the case of KN losses we have an opposite trend: $\tau_L \propto E/\ln E$, so that high energy particles

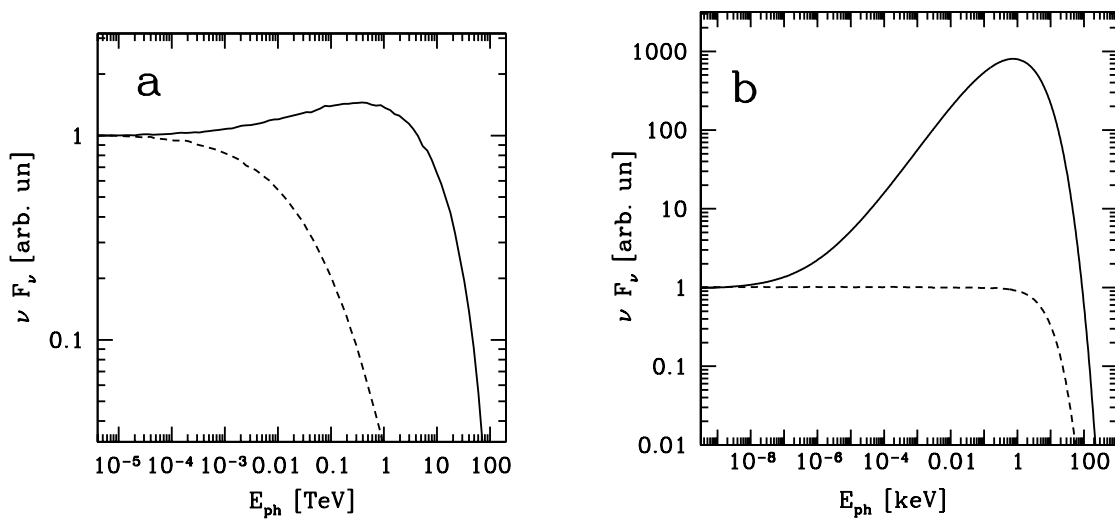


Figure 5.3: **a)** Inverse Compton photon distribution produced by the electron spectra in Fig. 5.2b on a diluted black body at $T = 3500$ K for the case of dominant IC losses (solid line) and for the case of dominant synchrotron cooling (dashed line). **b)** Synchrotron emission from the two electron distributions in Fig. 5.2b, the magnetic field value is $10 \mu\text{G}$.

can propagate further than low energy ones and the resulting spectrum is harder. This effect produces the pile up when integrating the spectrum over space. In the case we are considering in this section, we assume that the loss time scale is the limiting one at every energy in the range we consider. In real physical environments this may not be the case. At low energies, where the Thomson regime is recovered also in the IC case, the time scale of energy losses increases with decreasing energy, therefore it could at some point become larger than the age of the system itself. The maximum energy of the accelerated particles is still determined by the energy losses, but the low energy part of the spectrum does not have enough time to cool and the spectrum results in $F_2 = f_0 u_2 \tau_{Age} \propto p^{-\alpha}$.

With the total spatially integrated spectrum obtained, we calculate the radiation emitted. Our results are shown in Fig. 5.3. Panel **a** shows the inverse Compton radiation resulting from the upscattering of the background radiation, when losses are Compton dominated (solid line), compared to the dominant synchrotron losses case (dashed line). The spectrum pile up is not so remarkable in the first case because the effect of the Klein-Nishina cross-section acts twice: while hardening the

electron distribution, it softens the IC photon one, so that the two effects almost cancel each other.

On the other hand, the accelerated particle features have a sharp imprint on the synchrotron spectrum (Fig. 5.3b) which carries direct information on the electron distribution. Compared to the case of pure synchrotron cooling (dashed line), the emission due to an electron distribution shaped by IC losses (solid line) presents a pile up of three orders of magnitude around the cut-off, which, for the chosen parameters, appears at keV energies. This characteristic is a remarkable signature to distinguish the two different scenarios for electron radiative losses.

5.3 Applications

The results we obtained in the previous Section may have broad astrophysical applications. To demonstrate this, we apply the results of our calculations to three specific astrophysical environments: *i*) a Supernova Remnant in the Galactic Centre region, *ii*) a shock in a Microquasar jet and *iii*) the accretion shock surrounding clusters of galaxies. We presented the basic characteristics of the non-thermal behaviour of these classes of objects in Chapter 1, where we showed that strong non-relativistic shocks may form in such sources and the radiation energy density may dominate over the magnetic field energy density.

For each of the considered cases, we evaluate both the electron spectrum and the spectrum of the emitted radiation.

5.3.1 SNR in the Galactic Centre

We recall here that several observations in the radio and X-ray bands have confirmed Supernova Remnant (SNR) shocks as powerful accelerators of electrons up to tens of TeV. We first consider a SNR in the galactic disk. The radiation field in the Galaxy consists of three distinct components: the optical/Near-Infrared (NIR), the Far Infrared (FIR) and the Cosmic Microwave Background (CMB) radiation, with an energy density of $\sim 0.5, \sim 0.1, \sim 0.25$ eV/cm³, respectively (Mathis et

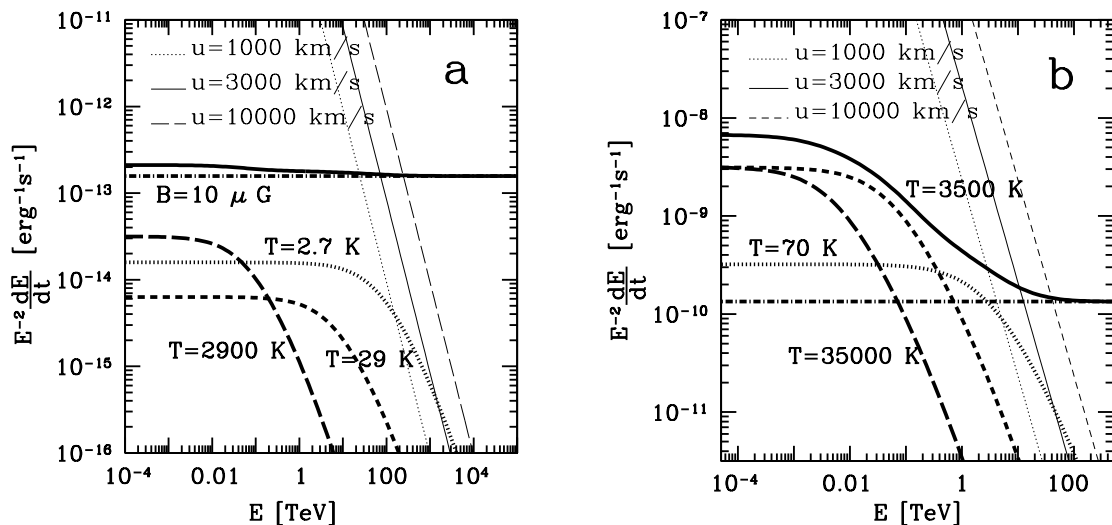


Figure 5.4: **a)** Energy loss rates and acceleration rates, multiplied by E^{-2} , as a function of the electron energy E , for a Supernova Remnant in the Galaxy. The synchrotron rate (thick dot-dashed line) corresponds to a magnetic field $B = 10 \mu\text{G}$, the IC curves are calculated for three black bodies at temperature $T = 2900 \text{ K}$ (Optical), thick long-dashed line; $T = 29 \text{ K}$ (Far Infrared), thick short-dashed line; $T = 2.7 \text{ K}$ (CMB), thick dotted line. The thick solid curve represents the sum of the four loss contributions. Thin lines: acceleration rates for $B = 10 \mu\text{G}$ and shock velocity of 1000 km/s (dotted), 3000 km/s (solid) and 10000 km/s (dashed). **b)** Same as in panel **a** but for a magnetic field $B_1 = 100 \mu\text{G}$ with $B_2 = 4B_1$ and three black bodies at $T = 35000 \text{ K}$ (UV/Optical), $T = 3500 \text{ K}$ (NIR) and $T = 70 \text{ K}$ (FIR).

al., 1983). In our calculation we evaluated an effective temperature for these fields from their peak energy and then assumed they can be approximated with a diluted black body distribution. The Galactic magnetic field has a measured value of $\sim 3 \mu\text{G}$ (see Widrow 2002 for a review), which corresponds to an energy density of $\sim 0.23 \text{ eV/cm}^3$. This implies that the average magnetic field energy density is comparable to the radiation one. Moreover, the magnetic field can be significantly amplified in the presence of a shock which is efficiently accelerating particles (Lucek & Bell, 2000), so that, in the acceleration region, $U_{mag} \gg U_{rad}$. Therefore synchrotron losses are dominant over inverse Compton (Fig. 5.4a). In this case the contribution of the IC to the energy loss rate is negligible and the cut-off energy and shape are determined by synchrotron cooling.

Things are dramatically changed, though, if we consider a SNR in the Galactic

Centre (GC) region, where both the magnetic and the radiation fields are much stronger than the average Galactic values. In analogy with what was done in Hinton & Aharonian (2007), we consider the inner 1 pc of the Galaxy, where the values of the radiation energy density are $5 \times 10^4 \text{ eV/cm}^3$ at $kT = 3.0 \text{ eV}$ (UV) and $kT = 0.3 \text{ eV}$ (NIR), and $5 \times 10^3 \text{ eV/cm}^3$ at $kT = 6 \times 10^{-3} \text{ eV}$ (FIR) (Davidson et al., 1992). To have an equal energy density in the magnetic field it is required that $B \simeq 500 \mu\text{G}$, any lower value implies the dominance of IC (KN regime) losses in determining the cut-off in the electron spectrum. We choose $B_1 = 100 \mu\text{G}$ in agreement with the magnetic field values inferred for SNR (see Chapter 1). We assume Bohm diffusion, which means that the turbulence in the magnetic field is of the order of the ordered component. To take this effect into account we choose $\xi = 4^1$, accounting for the compression of the disordered magnetic field at the shock crossing.

As shown in Fig. 5.4b, for a velocity of 3000 km/s, $B_1 = 100 \mu\text{G}$ and $B_2 = 4B_1$, the cut-off energy is $E^* \simeq 10 \text{ TeV}$.

As discussed in Section 5.2, depending on the age of the system, particles in the low energy part of the interval we consider may not have enough time to cool. Keeping as a reference the age of the historical SNR that are known to be efficient electron accelerators, we performed our time dependent calculation and present here the results for $\tau_{Age} = 100\text{yr}$, 500 yr and finally, as a comparison, the steady state case.

At the shock location steady state is reached quickly so that the three cases overlap perfectly. The result is shown in Fig. 5.5a (solid line), where we compare it with the one obtained for pure synchrotron losses, with the same values of the

¹In a completely randomised magnetic field, the field components in the three spacial directions can be considered equal, therefore the compression of the two perpendicular component at the shock crossing leads to a total compression factor $\xi = \sqrt{11}$, adopted e.g. in Zirakashvili & Aharonian (2007). In the case of magnetic field amplification upstream, the turbulent component formed by perpendicular waves is amplified to values that can exceed the assumed parallel background component, leading to a total compression of the magnetic field close to 4. In this situation the diffusion coefficient is not strictly Bohm-type anymore, however the exact expression for this quantity is not known and the assumption of Bohm diffusion seems the most appropriate guess (see e.g. Caprioli et al., 2008).

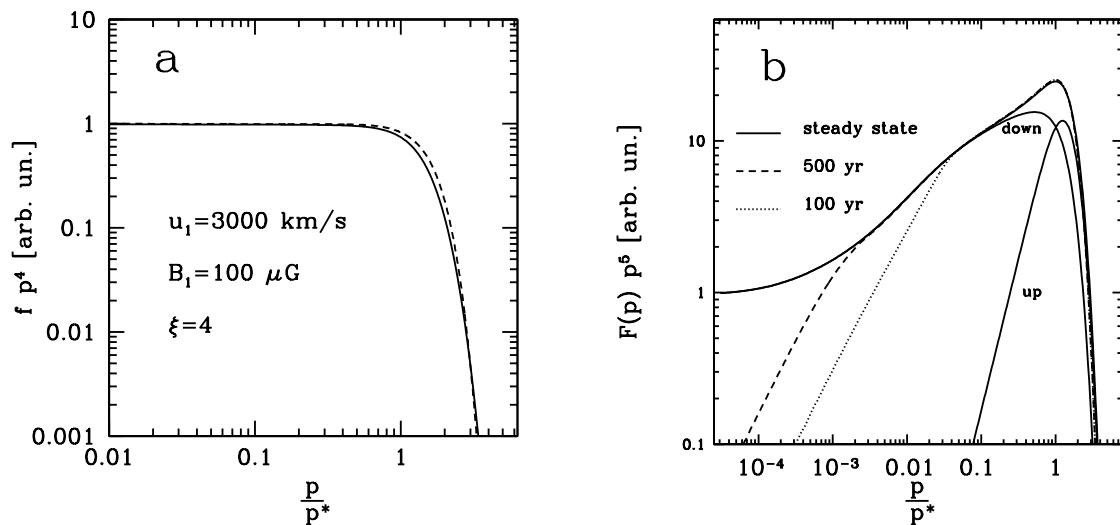


Figure 5.5: **a)** Electron spectrum at the shock for a velocity of 3000 km/s and a magnetic field $B_1 = 100 \mu\text{G}$. The solid line is obtained in the case of dominant IC losses with the same parameters as in Fig. 5.4b, the dashed line corresponds to the case when the radiation energy density is suppressed and synchrotron cooling dominates. **b)** Integrated spectra for same values of the parameters of panel **a**. The three curves correspond to different maximum times of acceleration, as reported.

other parameters (dashed line). The features are those pointed out in Section 5.2: the cut-off region is broader and the decay is less steep than for synchrotron cooled electrons. The effect, however, is less significant than in our illustrative example, due to the fact that at the cut-off energy and beyond the energy losses are close to recover their Thomson behaviour (see Fig. 5.4b).

On the other hand, the importance of the predominance of Klein-Nishina IC losses right below the cut-off is evident in Fig. 5.5b where we plot the spatially integrated spectra for the three different time scales chosen. The up and downstream contributions are also plotted for the steady state solution to enlighten the nature of the substructure present around the cut-off energy. In the integrated distribution the modification of the spectrum due to KN effects can be dramatic. In our example the hardening of the spectrum right below the cut-off causes a pile up of more than one order of magnitude, compared to the solution for Thomson losses, which would correspond to a horizontal line in the plot.

The shape of the spectrum around the cut-off is determined by losses, therefore

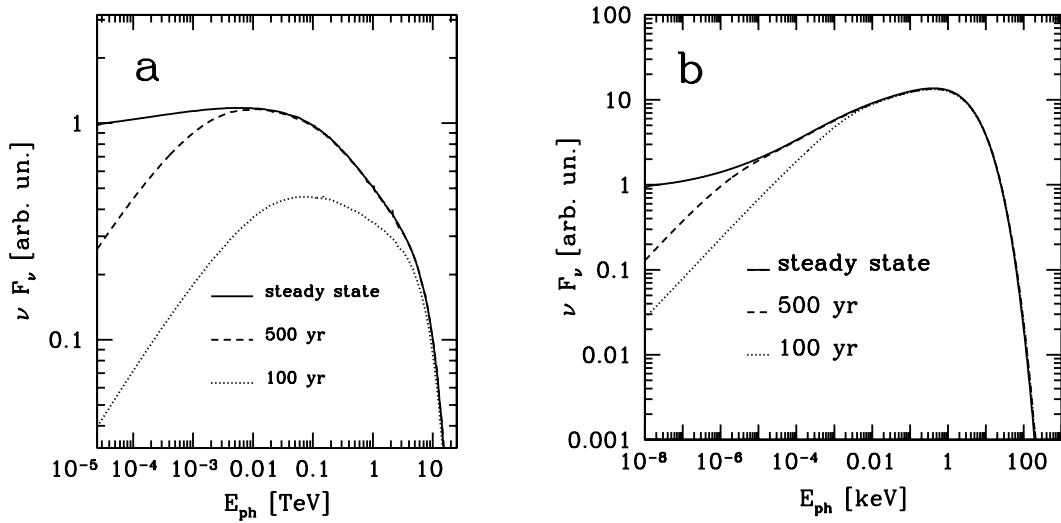


Figure 5.6: Radiation emitted by the electron distributions in Fig. 5.5b. The up and downstream components have been summed up. **a)** Total inverse Compton spectra. The contributions of the three black bodies considered have been summed up. **b)** Synchrotron radiation spectra.

being the same for the three curves. At lower energies, the point where losses set in depends on the time. For those energies where $\tau_L > \tau_{Age}$ we obtain the uncooled spectrum $F(p) \propto p^{-4}$. We plot the steady state solution as a test in order to show that our method recovers the right solution $\propto p^{-5}$ at low energies where losses proceed in the Thomson regime.

Once we have the electron spectrum we can calculate the photon distribution. Our results for IC are shown in Fig. 5.6, where we plot the spectra for the different time scale we are considering. Each of the curves represents the sum of the contributions of the three components of the seed field (FIR, NIR, UV). For the steady state solution, the overall radiation spectrum shows an almost flat profile below the cut-off due to the compensation of the “double action” of the Klein-Nishina effect. The other two curves harden in the low energy part due to the slope of the electron spectrum at low energies. In addition, we see from Fig. 5.4b that the contribution of the three radiation fields dominate in different energy ranges. The higher the temperature of the black body, the lower the energy of the electrons required to enter the KN regime. For this reason, at early stages of the evolution (100 yr, dotted curve in Fig. 5.6a) when the low energy part of the electron spectrum is not yet

contributing to the photon emission, the contribution of the two high temperature black bodies at 3500 K and 35000 K is almost zero and the total IC radiation is lower than at later times.

Fig. 5.6b shows the synchrotron emission. Here the situation is different: as expected the radiation spectrum reproduces the features of the electron one. A pronounced pile up appears around the cut-off energy for all the three cases.

5.3.2 Microquasars

Another class of objects of great interest are Microquasars, that we briefly discussed in Chapter 1. The nature of these objects is very complex and is not yet fully understood. Nevertheless the basic ingredients present in the system are a very intense stellar radiation field (e.g. for LS 5039 the luminosity of the star is $L_* \simeq 7 \times 10^{38}$ erg/s implying a radiation energy density up to $U_{rad} \simeq 1000$ erg/cm³, depending on the location, at a temperature of $T \simeq 3.8 \times 10^4$ K (Casares et al., 2005)) and a jet which is thought to be the site of particle acceleration. If blobs of plasma are emitted in the jet at slightly different velocity, internal sub-relativistic shocks can form, where electron acceleration can take place. The value of the magnetic field is not known, but it reasonably ranges between 0.01 and 1 G.

For our calculation we refer to the model used in Khangulyan et al. (2008), where the jet from the compact object is assumed to have its axis perpendicular to the orbital plane and we put the acceleration zone at a distance $Z_0 = 2 \times 10^{12}$ cm from the jet base (this corresponds to a distance equal to the mean orbital radius). At such a distance the radiation energy density becomes:

$$\frac{L_*}{4\pi c(R_{orb}^2 + Z_0^2)} \simeq 230 \frac{erg}{cm^3}. \quad (5.6)$$

In Fig. 5.7 we plot as thick lines the total energy loss rates due to IC plus synchrotron losses and as thin lines the acceleration rates for a shock velocity of 30000 km/s. The solid lines correspond to a magnetic field value upstream of 1 G, the dashed ones to $B_1 = 0.3$ G and the dotted lines to $B_1 = 0.1$ G and a downstream magnetic field $B_2 = 4B_1$. We chose $u_1 = 30000$ km/s, corresponding to 10% of the

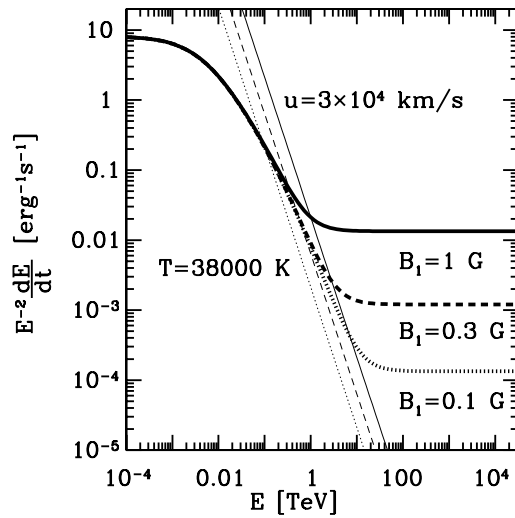


Figure 5.7: Total loss rates (thick lines) due to IC upscattering of a black body photon field at $kT \simeq 3.3$ eV plus synchrotron emission for the values of B_1 reported, feasible for a Microquasar. The shock velocity is fixed at 30000 km/s and the thin lines correspond to the acceleration rates connected to the values of the magnetic field for which we plot the loss rates.

speed of light, in order to remain consistent with the assumption of non-relativistic shock.

In this case the radiation energy density is considerably larger than the magnetic one, even for a field $B_1 = 1$ G. This is the value we consider in our calculation in order to obtain an efficient acceleration of electrons up to TeV energies. Moreover, from a theoretical point of view, this choice allows us to explore a different region of the KN losses, as compared to the other two cases presented in this Section.

The IC cooling time at the cut-off energy for the configuration described is $\tau_L \simeq 40$ s. As a rough estimate we can say that the dynamical time of the shock is $\tau_{Age} \sim Z_0/u_1 \simeq 300$ s. We therefore report on the results of our calculation for a time of 50 s, 100 s and 300 s. We also show the steady state solution for comparison. In Fig. 5.8 we plot the electron spectrum at the shock and integrated over space. The dashed line in panel **a** represents the expected spectrum for pure synchrotron cooling. The different shape of the spectrum around the cut-off energy with respect to the solid curve is very pronounced. We see that, when the age of the system is comparable to the loss time scale at the cut-off energy (50 s), the steady state is

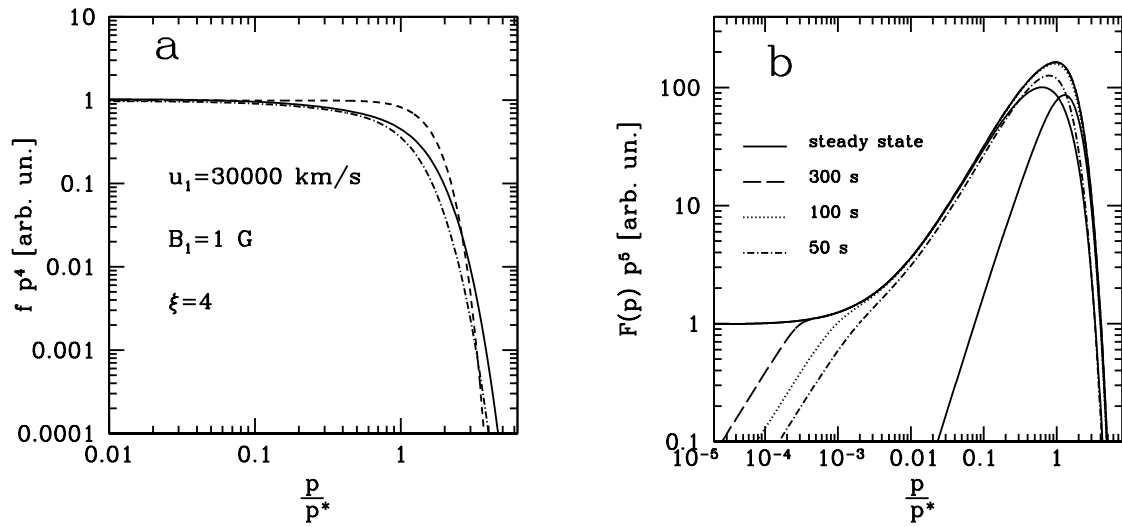


Figure 5.8: **a)** Electron spectrum at the shock for a shock velocity $u_1 = 30000$ km/s. The value of the magnetic field is $B_1 = 1$ G and $B_2 = 4B_1$. The solid line represents the case of dominant IC losses for an acceleration time ≥ 100 s, the dot-dashed one is for $t_{acc} = 50$ s, while the dashed one is obtained with pure synchrotron cooling in steady state. **b)** Integrated electron spectra for the time scales reported. In the case of steady state solution we plot also the two components up and downstream.

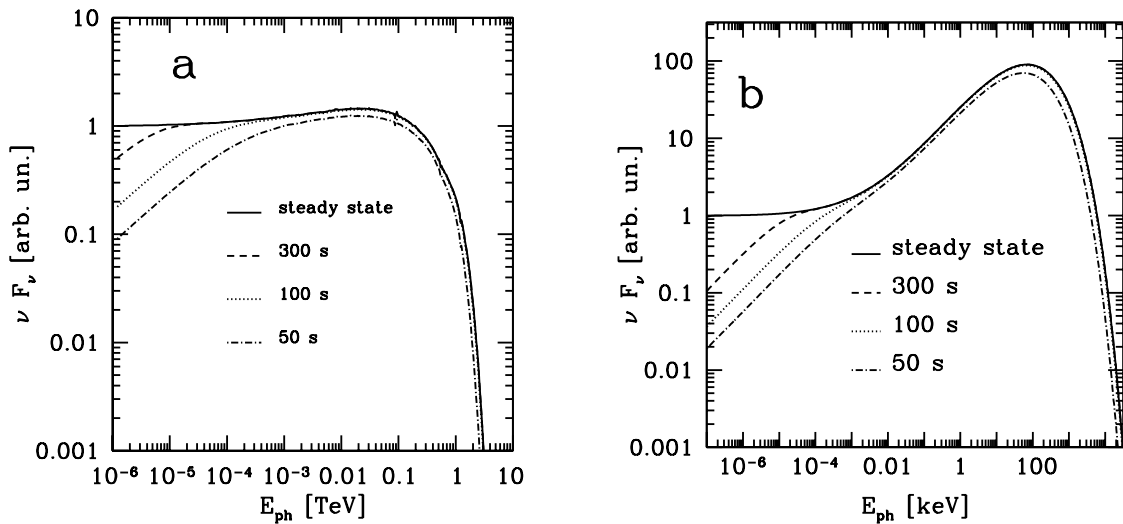


Figure 5.9: Photon spectra produced by the electron distributions in Fig. 5.8b. **a)** IC spectra for a diluted black body of temperature $T \simeq 3.8 \times 10^4$ K. **b)** Synchrotron spectra.

not reached even at the high energy end of the spectrum (dot-dashed line in Fig. 5.8, both panels). In the cases corresponding to 100 s and 300 s (dotted and dashed lines respectively in panel **b**), on the other hand, the spectrum around the cut-off reaches its steady state. Only the low energy part of the spectrum presents the characteristic uncooled slope.

In this case the predominance of the IC is such that the hardening of the integrated spectrum is very pronounced, the pile up spanning two orders of magnitude.

As in the previous cases, the IC photon spectrum does not show prominent features (Fig. 5.9a), while the synchrotron one reproduces the electron pile up (Fig. 5.9b).

5.3.3 Clusters of Galaxies

Another example of a radiation dominated environment where a shock can form is represented by clusters of galaxies. Particle acceleration is expected to happen at accretion shocks (see Blasi et al., 2007 for a review). The infalling matter crosses the shock surface at a speed roughly comparable to the free fall velocity, namely:

$$v_s \sim \sqrt{\frac{2GM_{cl}}{R_{cl}}} \approx 2000 \left(\frac{M_{cl}}{10^{15} M_{\odot}} \right)^{1/2} \left(\frac{R_{cl}}{3Mpc} \right)^{-1/2} km/s,$$

so that the shock velocities are comparable to the one found in Supernova Remnants.

In this section we treat the acceleration and energy losses of electrons. Interestingly, in these objects the energy loss time scale is smaller than the age of the accelerator also for protons. We will discuss this case in the next Chapter.

As discussed in Chapter 1, the value of the magnetic field inferred by diffuse synchrotron radio emission reveals the presence of a magnetic field of the order of few μG in the intracluster medium. In the cluster outskirts, where the accretion shock propagates, the value of the field is unknown, due to lack of radio measurements, but it is likely to be smaller or at most comparable to the one measured in the inner regions. For a magnetic field 1 μG , the magnetic energy density at the shock position is $\sim 0.025 \text{ eV/cm}^3$. This implies that at the position of the shock the main energy loss channel for relativistic electrons is inverse Compton scattering off

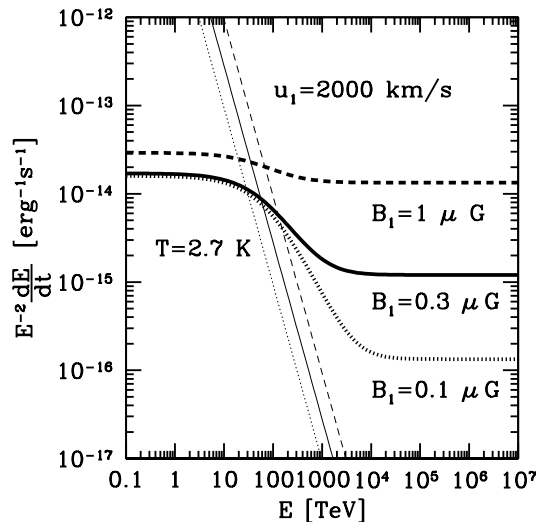


Figure 5.10: Thick lines: energy loss rates (synchrotron plus IC) for typical conditions in a galaxy cluster accretion shock. The background radiation field is provided by the CMB and the values of the magnetic field upstream are reported (downstream $B_2 = 4B_1$). Thin lines: acceleration rates for a shock velocity of 2000 km/s and the line type refers to the corresponding value of B_1 .

the Cosmic Microwave Background photon field, characterised by an energy density of $\sim 0.25 \text{ eV/cm}^3$. Optical and infrared radiation from cluster galaxies is totally negligible.

In Fig. 5.10 we plot the energy loss rates for a fiducial galaxy cluster. The thin lines represent the acceleration rates for a velocity $u_1 = 2000 \text{ km/s}$ and different values of the magnetic field. The thick lines are the total energy loss rates for inverse Compton scattering off the CMB plus synchrotron emission. Calculations are done for three values of the upstream magnetic field B_1 and $B_2 = 4B_1$: $1 \mu\text{G}$ (dashed lines), $0.3 \mu\text{G}$ (solid), $0.1 \mu\text{G}$ (dotted).

Below we consider the case of parameter values $B_1 = 0.3 \mu\text{G}$ and $u_1 = 2000 \text{ km/s}$, reasonable for an accretion shock around a rich cluster (Blasi et al., 2007). In this case, the cut-off energy falls in the KN dominated part of the total loss rate, at about 60 TeV (corresponding to the intersecting point between the thick solid line and the thin solid line in Fig. 5.10). At the cut-off energy the loss time scale is of the order of $4 \times 10^4 \text{ yr}$. The evolution times of large scale structures are of the order of several Gyr, meaning that electrons cool comparatively very rapidly. Therefore

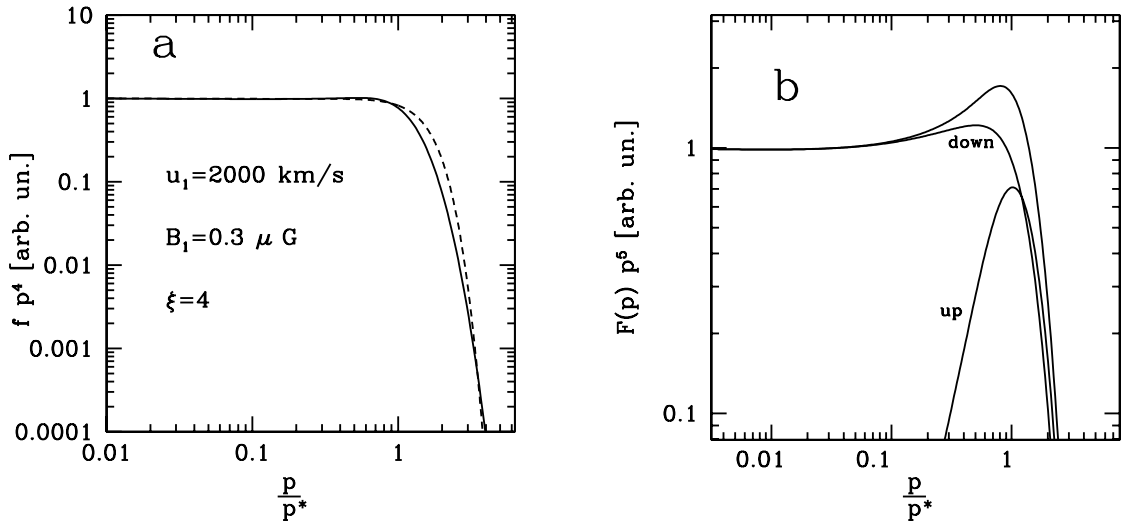


Figure 5.11: a) Electron distribution at the shock front for a shock velocity of 2000 km/s and a magnetic field $B_1 = 0.3 \mu\text{G}$ in the two cases of intense inverse Compton losses (solid line) and dominant synchrotron cooling. b) Integrated spectra for the IC dominated case. The upstream and downstream contributions are shown.

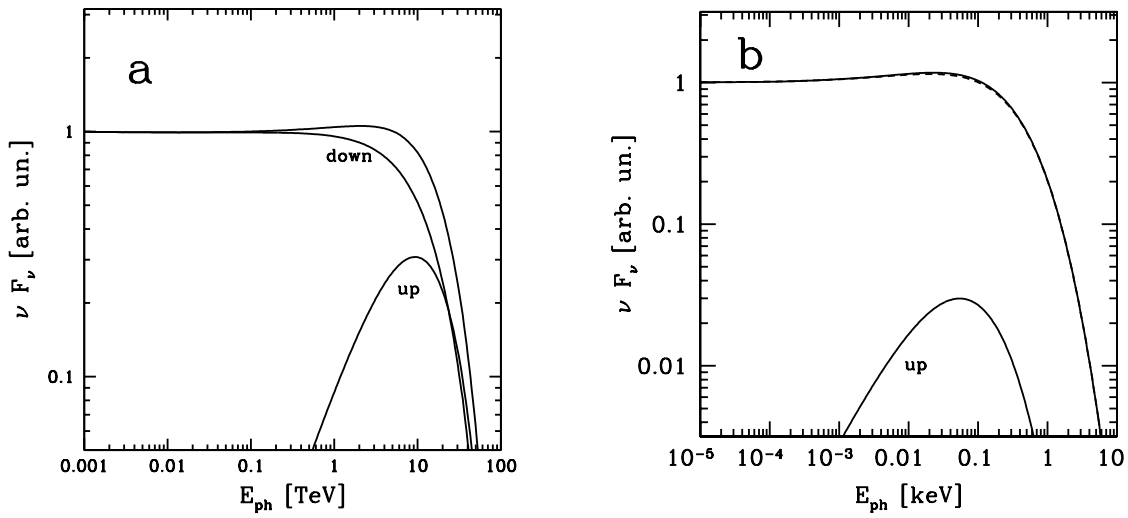


Figure 5.12: a) Inverse Compton spectrum produced by upscattering of the CMB for the distributions in Fig 5.11b. b) Synchrotron radiation emitted in the upstream region, downstream region, and their sum. The upstream contribution is negligible, so that the downstream curve (dashed) and the total one coincide.

the steady state is always reached.

In Fig. 5.11a we plot the electron spectrum at the shock (solid line), compared to the one expected for pure synchrotron losses (dashed line). The modification due to the dominant IC losses has the same characteristics noticed before: a wider and less sharp cut-off.

If we look at the effect this produces on the total spatially integrated particle spectrum, we find that a small pile up is still present around the cut-off energy (Fig. 5.11b). This feature is less pronounced in the present case because the energy losses right below the cut-off energy fall in the Thomson regime, as we can see from Fig. 5.10. The process does not happen deep enough in the Klein-Nishina regime to produce a strong feature.

The photon spectra are affected in a similar way. In Fig. 5.12a we plot the up-scattered spectrum of the CMB. We plot the two contributions to the total spectrum from the upstream and downstream regions, the latter dominating the total spectrum. Fig. 5.12b shows the synchrotron spectrum where the small pile up feature of the electron spectrum is reproduced.

Chapter 6

Proton Acceleration in Galaxy Clusters

Clusters of galaxies can be good candidates for the acceleration of protons to ultra-high energies. Indeed, according to the Hillas criterion (Hillas, 1984), they reside among the sources capable, as long as this concerns the dimensions of the structure and the value of the magnetic field, to accelerate protons up to 10^{20} eV. Moreover, clusters are cosmological structures and their lifetime is comparable to the age of the Universe, therefore, if acceleration takes place in such objects, protons acceleration can continue up to $\sim 10^{10}$ yr. On the other hand, high energy protons up to energies of the order of 10^{15} eV and possibly higher are well confined in the volume of the cluster over this time scale. For these two reasons, protons accumulate in the cluster and a population of ultrahigh particles is expected at the present time in these structures, up to a total energy of $\sim 10^{62}$ erg, comparable with that in the magnetic field, assuming $1 \mu\text{G}$ and a spherical cluster of 3 Mpc of radius.

Although the dimensions of the system and the age of the accelerator formally allow protons to be accelerated up to 10^{20} eV, the particles can in fact lose energy via pair and pion production in the interaction with the photons of the CMB. As discussed in Norman et al. (1995) and Kang et al. (1997), for a shock velocity of a few thousands km/s and a magnetic field of the order of the microGauss, the shock acceleration rate is compensated by the energy loss rate at energies around

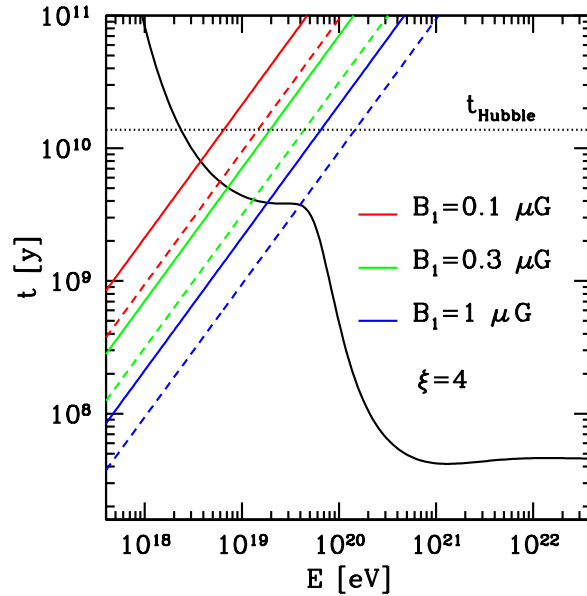


Figure 6.1: Acceleration and energy loss time scales as a function of the proton energy. Black solid line: energy loss time of proton-photon interactions (pair and pion production). Red lines: acceleration time for $B_1 = 0.1 \mu\text{G}$ and $B_2 = 4B_1$ for a shock velocity of 2000 km/s and (solid) and 3000 km/s (dashed). Green and blue lines: same as before for $B_1 = 0.3 \mu\text{G}$ and $B_1 = 1 \mu\text{G}$, respectively. As a dotted black line we report the estimated age of the Universe, for comparison.

10^{19} eV (the exact value depending on the assumed diffusion coefficient). In Fig. 6.1 the time scales for the process are plotted. We assume Bohm diffusion (Eq. (5.1)) and a magnetic field compression at the shock $\xi = 4$. We plot as solid lines the acceleration times for a shock velocity of 2000 km/s and an upstream magnetic field of $0.1 \mu\text{G}$ (red), $0.3 \mu\text{G}$ (green) and $1 \mu\text{G}$ (blue). For the same values of the magnetic field, we plot as dashed lines the acceleration times for a shock velocity of 3000 km/s. The solid black line represents the total energy loss time associated with photopair and photopion production in interaction with the CMB radiation field at the temperature of 2.7 K. Pair production dominates up to energies of about 5×10^{19} eV. Once the particle energy has passed the threshold for meson production, this process becomes rapidly dominant and the contribution by pair production is negligible. Fig. 6.1 shows that, if protons can be accelerated beyond few times 10^{18} eV, the cut-off energy as well as the shape of the particle spectrum in the cut-off region are determined by pair production. Even for extreme values of the cluster

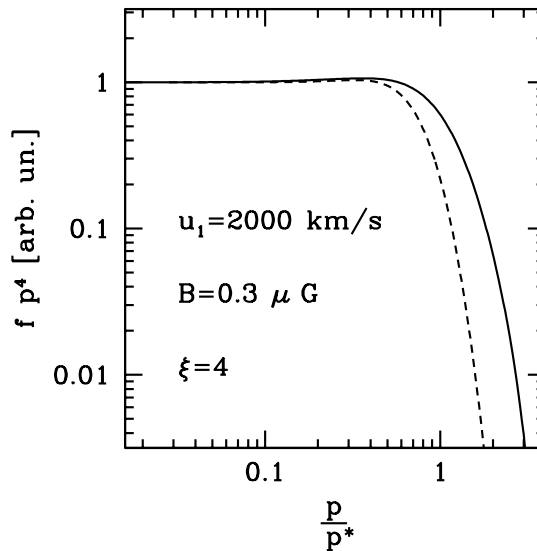


Figure 6.2: Proton spectra at the shock location for an acceleration time of 10 Gyr (solid line) and 5 Gyr (dashed) for a shock velocity of 2000 km/s and a magnetic field upstream of $0.3 \mu\text{G}$. The x-axis has been normalised to the parameter p^* defined in Chapter 5.

parameters ($u_1 = 3000 \text{ km/s}$, $B_1 = 1 \mu\text{G}$ and $B_2 = 4 \mu\text{G}$), in the case of Bohm diffusion, the energy range where pion production is dominant is never achieved.

To perform our calculation we choose conservative values of the parameters: a shock velocity of 2000 km/s and a magnetic field upstream $B_1 = 0.3 \mu\text{G}$, with $B_2 = 4B_1$ (green solid line in Fig. 6.1). We do not take into account the evolution of the CMB with redshift. The simplification is justified by the fact that the acceleration rate and the energy loss rate become comparable on a time scale of about 5 Gyr. Therefore, for local clusters, this time scale places the beginning of the acceleration process at an epoch where the redshift is $z < 1$ and we can neglect the evolution of the CMB radiation. Moreover, as discussed in Kang et al. (1996), the higher temperature and energy density of the CMB radiation at large redshifts inhibits the acceleration of protons to ultrahigh energies at early epoch.

6.1 Primary and Secondary Particle Spectra

In Fig. 6.2 we plot the calculated proton spectra at the shock location. We perform our calculation for an age of the system of 5 Gyr and 10 Gyr. The difference between

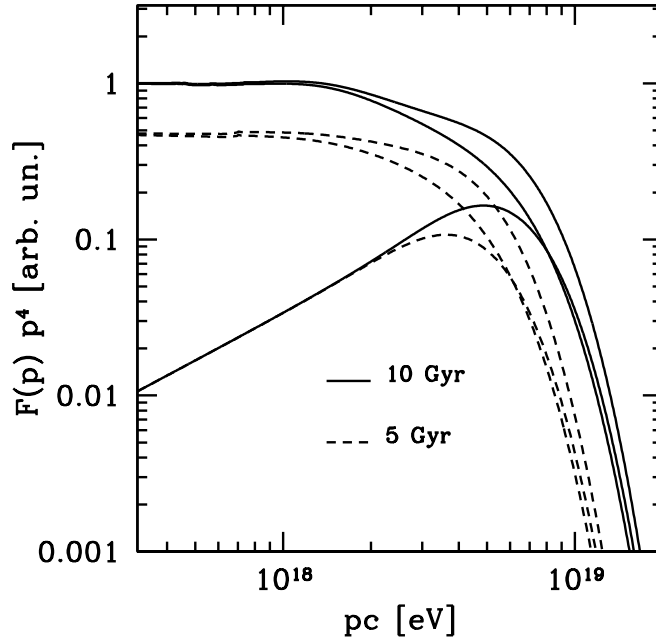


Figure 6.3: Spectra integrated over the upstream and downstream regions for the proton distributions in Fig. 6.2. The solid lines correspond to an accelerator age of 10 Gyr and the dashed one to an age of 5 Gyr.

the spectra at the two ages demonstrates that the system does not reach steady state. Therefore, a time dependent calculation is essential in order to accurately model the particle spectrum. The momentum scale on the x -axis in the figure is normalised to p^* , defined as in Chapter 5, and corresponding to an energy $E^* = 7 \times 10^{18}$ eV. A small bump is present in the spectra around the cut-off energy, due to the flattening of the energy loss time scale in that energy range. The prominence of the feature increases with time.

The spectral features are more evident in the spatially integrated spectra reported in Fig. 6.3. As discussed in Chapter 5, the upstream spectral shape below the cut-off is determined by diffusion, while downstream the spectrum is shaped by energy losses. In this component, a bump forms around 10^{18} eV due to the fact that around that energy (close to the threshold of the process) the pair production loss rate changes behaviour from a very steep dependence on the particle energy to an almost flat distribution. Therefore, particles at slightly lower energies are only marginally affected by losses, as we can see from the fact that, below 10^{18} eV, a

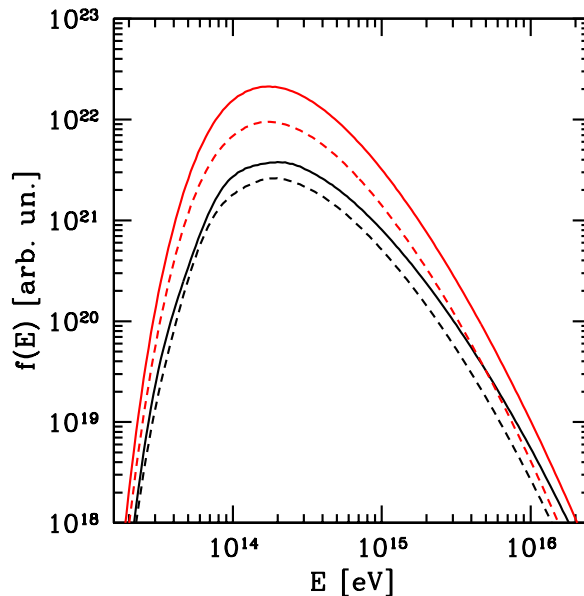


Figure 6.4: Production spectra of pairs. Red lines: downstream spectra for 10 Gyr (solid) and 5 Gyr (dashed); black lines: upstream spectra for the same cases.

power law spectrum $\propto p^{-4}$ is recovered, as expected for an uncooled spectrum; on the other hand, particles at slightly higher energies experience a very fast cooling so that there is an effect of accumulation around the threshold. The effect is analogous to the one discussed in Berezhinsky & Grigoreva (1988), explaining the appearance of a bump in the ultrahigh energy Cosmic Ray spectrum due to meson production during propagation. Even more interestingly, as a consequence of the shallow dependence on energy of the loss time scale at the cut-off energy and above it, the spectrum in the cut-off region is less steep than an exponential. At energies around 10^{20} eV, a second steepening is in fact present (not shown in figure), due to the effect of pion production, however at that energy the flux is suppressed by several orders of magnitude with respect to the cut-off value and pair production results negligible in shaping the proton spectrum.

It is worth stressing that, even though the contribution from the downstream region is dominant at low energies (due to the effect of diffusion and advection upstream, as discussed in Chapter 5), around the cut-off the contribution of the two components differ only by a factor of few.

From the proton spectra, the electron-positron pair production spectrum are

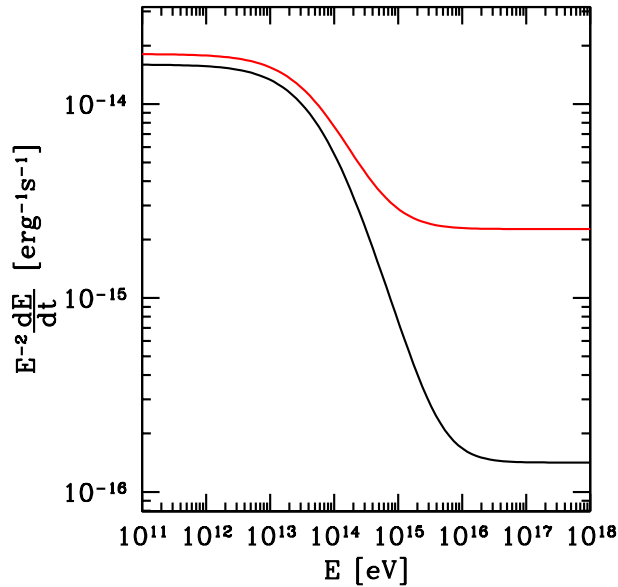


Figure 6.5: Energy loss rates for pairs due to synchrotron and IC processes, in red downstream (magnetic field value $B_2 = 1.2 \mu\text{G}$) and in black upstream (magnetic field of $B_1 = 0.3 \mu\text{G}$).

calculated using the formalism proposed by Kelner & Aharonian (2008). Since the magnetic field is assumed to be homogeneous and the CMB field is highly homogeneous, the spatially integrated proton spectra can be correctly used to calculate the secondary particle distributions. The results are reported in Fig. 6.4. The solid curves are the downstream (red) and upstream (black) pair spectra for an accelerator lifetime of 10 Gyr. The dashed curves are the spectra for a lifetime of 5 Gyr (downstream in red and upstream in black).

In the following we present our results for the case of a system age of 5 Gyr.

Once produced, the electrons (hereafter the term “electrons” has to be intended as referring to both electrons and positrons), lose energy in the interaction with the CMB field and the background magnetic field. The energy loss rates for these two processes are plotted in Fig. 6.5. The curves have been multiplied by E^{-2} in order to obtain horizontal lines for Thomson-like losses. The red curve corresponds to the sum of synchrotron and IC energy loss rates in the downstream region and the black one refers to the upstream region. In both cases the target photon field for IC is the CMB radiation at 2.7 K. The magnetic field downstream is 4 times bigger than the value upstream, therefore leading to a stronger contribution of synchrotron cooling

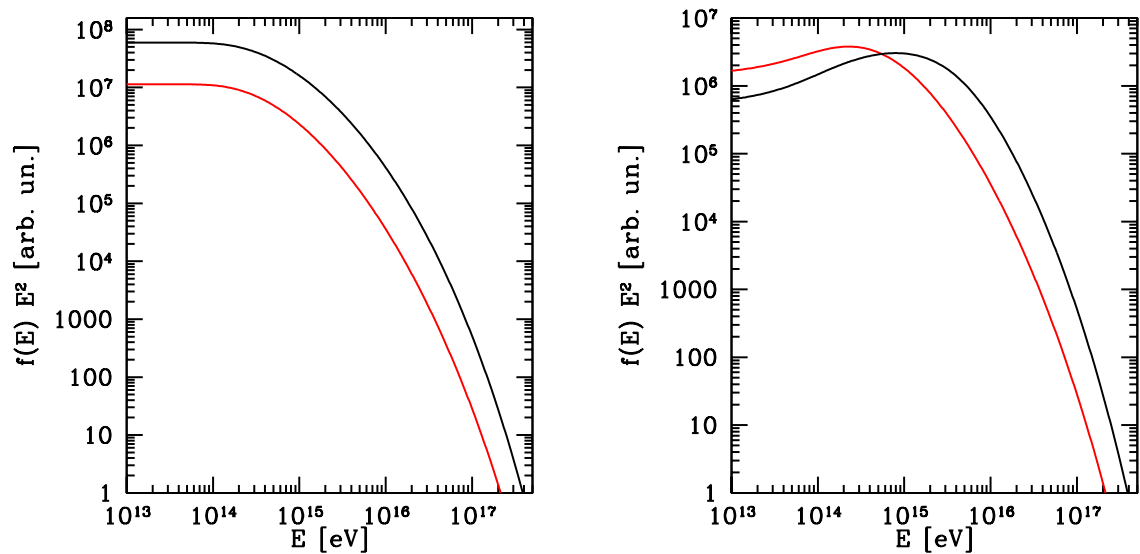


Figure 6.6: Electron spectrum after taking into account energy losses. The red and black lines refer to the downstream and upstream regions respectively. **a)** Spectra obtained considering pure synchrotron cooling in a magnetic field $B_1 = 0.3 \mu\text{G}$ upstream and $B_2 = 1.2 \mu\text{G}$ downstream. **b)** Same as in panel **a** but with the realistic combination of IC and synchrotron losses as in Fig. 6.5

in the first region. At low energies IC is the dominant energy loss channel and the transition between Thomson and Klein-Nishina regimes takes place around 10 TeV. Due to the steepening in energy of the KN loss rate, at higher energies synchrotron cooling becomes the limiting channel. Interestingly, from Fig. 6.4 we see that the peak of the electron distribution (~ 100 TeV) interacts with the CMB in the KN regime.

To obtain the cooled spectrum of electrons we use Eq. (3.42), assuming that the particles do not undergo any further acceleration during their lifetime. The use of the steady state equation is justified by the short time scale of radiative losses: at an energy of 100 TeV, the synchrotron cooling time in a $0.3\mu\text{G}$ magnetic field is $\tau_L \simeq 10^6$ yr and shorter when including the presence of IC losses. Hence, the time scale of electron energy losses is much shorter than the evolution time of the spectrum of the parent protons, of the order of 10^9 yr, therefore justifying a steady state treatment. The two panels in Fig. 6.6 show the cooled spectra of electrons downstream (red) and upstream (black) in the two cases of pure synchrotron losses (panel **a**) and synchrotron plus IC on the CMB field (panel **b**). The case in panel

a is not realistic, but it allows to understand the effects introduced by KN losses. At low energies, the energy losses are negligible in both cases and the spectrum tends to its uncooled steady state power law behaviour $\propto E^{-2}$. At higher energies, in the synchrotron dominated case, the spectrum has a featureless cut-off. Due to the fact that the production of pairs up and downstream happens at almost the same level, the more intense synchrotron losses downstream suppress the particle spectrum in that region. The effect of IC losses in the KN regime, instead, produces a hardening of the electron distribution below the cut-off (panel **b**). The pile up results in a factor of few. Since these energy losses affect the two sides of the shock in the same way, the slightly higher level of production downstream is reproduced in the cooled spectrum at low energies. Above the cut-off, when synchrotron losses become dominant (see Fig. 6.5), they determine the spectral shape.

6.2 Radiation spectra

We can now move to the calculation of the emitted radiation spectra from the electron distributions in Fig 6.6b. The broadband Spectral Energy Distribution (SED) of photons produced via synchrotron and IC emission is shown in Fig. 6.7. The red line corresponds to the downstream component and the black line to the upstream component. The synchrotron emission is enhanced by a factor of 10 downstream, as compared to upstream, due to the higher value of the magnetic field. The peak of the SED downstream is located at an energy slightly smaller than 100 keV, while upstream it is at an energy slightly larger than 100 keV. Note that, since the target radiation for IC scattering is the same up and downstream, the resulting gamma-ray emission spectra mimic the electron spectra. The maximum of the emission, both upstream and downstream, occurs between 100 and 1000 TeV.

Unlike other calculations of proton spectra in clusters of galaxies (e.g. Inoue et al., 2005), we do not assume an *a priori* spectrum, e.g. of the “standard” form $E^{-2}exp[-E/E^*]$, but rather calculate its shape within the model of DSA, taking into account energy losses. Interestingly, our self-consistent calculation shows a less steep fall off in the final emitted radiation spectrum above the cut-off energy. The

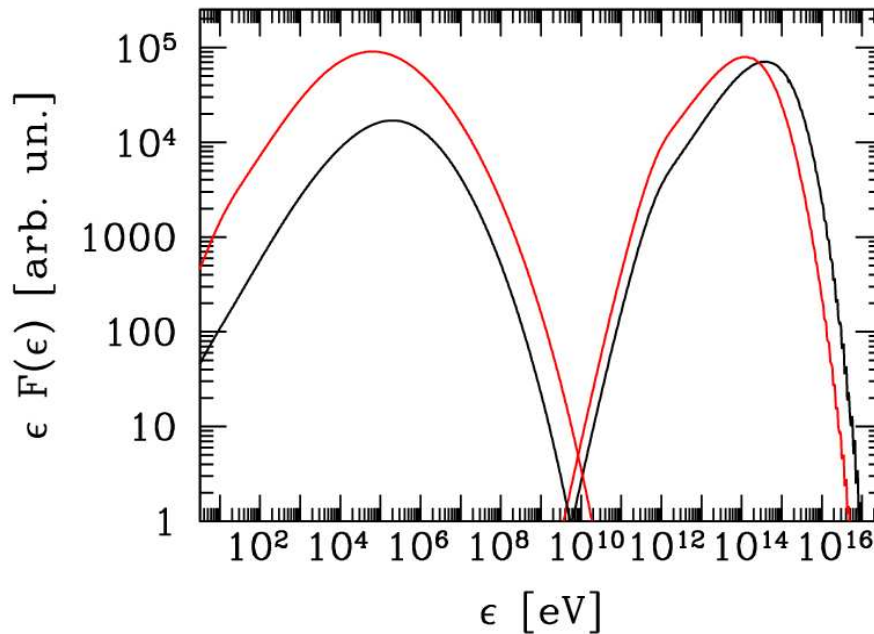


Figure 6.7: Broadband electromagnetic emission produced via synchrotron and IC cooling by the electron distributions in Fig. 6.6b. In red is the downstream component and in black the upstream component.

effect is the result of the combination of two factors: *i*) the accurate treatment of DSA correctly taking into account energy losses, *ii*) the accurate calculation of the shape of the produced electron spectrum ¹.

While we have evidence of hard X-ray emission from some clusters of galaxies (e.g. Fusco-Femiano et al, 1999; Enßlin et al., 2005), these objects have not yet been detected in gamma-rays. From our calculations, we can infer that the emission from clusters may be probed in the X-ray and gamma-ray bands in the near future. In fact the results presented in Fig. 6.7 are in arbitrary units, but when normalised to a total energy of protons in the cluster of 10^{62} erg, they result in a luminosity in each component (synchrotron and IC) of the emission of $L \sim 10^{42}$ erg/s. To estimate the expected flux, $F_E = L/(4\pi D^2)$, one has to fix the distance to the object. For example, in the case of the Coma cluster, $D = 100$ Mpc (Dressler, 1980). The energy flux for the synchrotron component appears to be of the order of 10^{-12} erg cm⁻² s⁻¹

¹The results from Kelner & Aharonian (2008) show that the commonly used delta approximation significantly deviates from the results of the accurate calculation.

and, for the IC, approximately one order of magnitude less, below 10 TeV (see Fig. 6.7). Note that, above 10 TeV, the effect of photon absorption on the background Infrared radiation field has to be taken into account as it strongly suppresses the flux of arriving gamma-rays (for present limits on Extragalactic Background Light see e.g. Aharonian et al., 2006c). It should also be noted that, in both the X-ray and gamma-ray bands, the detection of the emission from extended sources is very difficult. Nevertheless the above mentioned fluxes can hopefully be detected by future hard X-ray and gamma-ray instruments.

As a side remark, we note that the high energy gamma ray data from EGRET have shown the existence of a diffuse gamma background radiation at energies between a few MeV and about 100 GeV (Sreekumar et al., 1998). A contribution to this emission from galaxy clusters has been studied in the literature, but previous theoretical calculations have focus on the effect of IC radiation from primary electrons (Loeb & Waxman, 2000; Gabici & Blasi, 2003) and proton-proton processes (Colafrancesco & Blasi, 1998). Here we propose a mechanism that appears effective in all its three stages: *i*) if acceleration take place on time scales comparable to the age of the cluster, protons can be easily accelerated to energy of the order of 10^{18} eV and beyond; *ii*) once reached these energies, protons effectively interact with the CMB radiation to produce electron-positron pairs; *iii*) the electrons undergo a fast cooling, on time scales much smaller than the age of the source, and release all their energy in the form of synchrotron X-ray and IC gamma-ray emission. Therefore the contribution of this mechanism to the diffuse gamma background could be more significant than that of the mechanisms mentioned above.

Chapter 7

Conclusions

Overwhelming observational evidence exists that particles are accelerated to very high energies in several classes of astrophysical objects. To trace the presence of high energy particles, we rely on the non-thermal radiation they produce through interactions with the ambient matter, as well as with radiation and magnetic fields.

The same processes responsible for the emission of the observed electromagnetic radiation can limit acceleration, due to the energy losses the particles experience. In this scenario, energy losses determine the maximum energy of particles and contribute to the deformation of the spectrum in the region around the cut-off. The spectral shape of particles can, in turn, be imprinted on the radiation they emit and thus be carried to the observer. Therefore, an accurate modelling of the interplay between acceleration and energy losses, and the effect it has on both the particle and the radiation spectra appears essential. In particular, the spectral region around the cut-off energy is of primary importance in providing information on the specific characteristics of the environment under study.

Among the mechanisms that have been proposed in order to explain the acceleration of particles, Diffusive Shock Acceleration (Axford et al., 1977; Krymsky, 1977; Bell, 1978; Blandford & Ostriker, 1978) occupies a prominent place and has undergone intense theoretical study (e.g. see Drury, 1983; Malkov & Drury, 2001 for reviews). The problem of particle acceleration at non-relativistic shocks in the presence of strong energy losses has been addressed in the literature and solutions

have been found only in the special case of electrons undergoing synchrotron losses (Bulanov & Dogiel, 1979; Webb et al., 1984; Heavens & Meisenheimer, 1987; Zirakashvili & Aharonian, 2007). However, a general and self-consistent approach was missing.

In this work I developed a general approach to solve numerically the complete transport equation with the inclusion of an energy loss term and I calculate self-consistently the particle distribution function $f(x, p)$ and the resulting radiation spectra. This approach provides a general tool, independent of the species of particles accelerated (electrons and protons), the type of losses and the choice of the diffusion coefficient.

I applied my method specifically to the case where the background radiation energy density dominates over the magnetic energy density. I studied the case of accelerated electrons undergoing synchrotron and inverse Compton losses, in environments where the latter dominates. For high energy electrons, with energy $E \geq (mc^2)^2/\epsilon_{ph}$, inverse Compton scattering enters the Klein-Nishina regime where the cross-section decreases with energy. I evaluated the particle spectrum at the shock and found that, compared to the case of Thomson losses, the KN effect results in a broadening of the cut-off region and a hardening of the spectrum around the cut-off energy. The latter effect is more evident in the spatially integrated spectrum, which exhibits a pronounced pile up feature just below the cut-off energy. Such a feature can be significant, with an enhancement of the spectrum up to a few orders of magnitude, depending on the ratio of energy densities U_{rad}/U_{mag} , the magnetic field strength and the shock velocity.

The features present in the electron spectrum are reflected in the synchrotron emission resulting in a pile up below the cut-off energy. The impact on the IC distribution is less evident due to the compensation between the two actions of the KN cross-section on the electron spectrum and on the photon emission.

The importance of this effect was demonstrated for three astrophysical source populations in which the energy density of the radiation field dominates over the magnetic field energy density, namely in a Supernova Remnant located in the Galactic Centre region, in Microquasars and in galaxy clusters. For realistic values of the

parameters in these objects, the IC peak falls in the TeV energy band and the synchrotron peak is located in the keV range.

In this work I have presented, for the first time, accurate particle and photon spectra obtained taking into account simultaneously acceleration and radiative losses, and showed that this is of greatest importance around the spectral cut-off. A detailed modelling can be critical in understanding features in the high resolution broadband observations. In particular, in the case of radiation dominated environments, I demonstrate the impact of the KN cross-section on the electron spectrum and consequently on the synchrotron and IC components of the emission, the main feature being a pile up at the X-ray peak.

Proton acceleration in galaxy clusters was also studied in the framework of the proposed model. A population of very high energy protons is likely to be accelerated and accumulated over cosmological times inside these structures. While accelerating at external accretion shocks, protons can interact with the CMB radiation and lose energy via pair and pion production. For realistic values of the shock velocity of a few thousand km/s and a background magnetic field of the order of microGauss, the maximum energy achievable by protons is determined by the energy losses associated with pair production and ranges from a few times 10^{18} eV to a few times 10^{19} eV.

I performed the calculations assuming that acceleration takes place on time scales comparable to the age of the cluster. Since steady state is not reached in this type of situation, an accurate time dependent calculation is required. The spectra of the particles, when calculated correctly including the effect of energy losses, exhibit interesting features. The decay of the spectrum above the cut-off energy is not exponential. Its dependence on energy is shallower due to the flat profile of pair production time scales in the cut-off energy range. The spectra of the produced electron-positron pairs were accurately calculated numerically starting from the proton spectrum. Such a population of particles cools rapidly via synchrotron and IC processes in the background magnetic and radiation fields. In particular, the IC scattering proceeds in the KN regime. The effect of the hardening induced by the KN cross-section is visible in the IC radiation spectra both in the upstream and downstream regions of the shock. For the typical characteristics of galaxy clusters,

the synchrotron and IC peaks of the electron broadband emission are at comparable levels and the associated flux from a source at the distance of a 100 Mpc is expected at the level of 10^{-12} erg cm $^{-2}$ s $^{-1}$ in the X-rays and an order of magnitude lower for TeV gamma-rays. Note that the maximum of the gamma-ray emission is located above 100 TeV, which unfortunately cannot be observed due to severe absorption in the Extragalactic Background Light. The expected emission in gamma-rays from clusters of galaxies is at the limit of the sensitivity of present generation instruments, however it may be detectable with the future generation of detectors. In this regard, an accurate modelling of the radiation spectra like that presented in this work appears essential to provide an insight into the emission mechanisms and the physical processes in the high energy non-thermal sources.

Appendix A

We present here the details of our numerical calculation.

In the up and downstream regions, the transport equation for the particle distribution function reads:

$$\frac{\partial f(x, p, t)}{\partial t} + u \frac{\partial f(x, p, t)}{\partial x} - \frac{\partial}{\partial x} \left(D(p) \frac{\partial f(x, p, t)}{\partial x} \right) - \frac{1}{p^2} \frac{\partial}{\partial p} (p^2 L(p) f(x, p, t)) = 0. \quad (\text{A.1})$$

We know from the theory of DSA that, when energy losses are not important, the solution has a power law dependence on momentum as $f \propto p^{-4}$, we find therefore more convenient to work with the function $g = p^4 f$. Eq. (A.1) for g results:

$$\frac{\partial g(x, p, t)}{\partial t} = -u \frac{\partial g(x, p, t)}{\partial x} + D(p) \frac{\partial^2 g(x, p, t)}{\partial x^2} + p^2 \frac{\partial}{\partial p} (p^{-2} L(p) g(x, p, t)). \quad (\text{A.2})$$

To carry on the calculation, we treat separately the upstream and downstream region.

Upstream

As pointed out in Chapter 4, it is convenient to operate a change of variable from (x, p) to (z, y) defined as:

$$\begin{cases} z = \exp \left[x \frac{u_1}{D_1(p)} \right] \\ y = \ln p, \end{cases} \quad (\text{A.3})$$

which, inserted in Eq. (A.2), give:

$$\frac{\partial g}{\partial t} = -\frac{u_1^2}{D_1} z \frac{\partial g}{\partial z} + \frac{u_1^2}{D_1} z \frac{\partial}{\partial z} \left(z \frac{\partial g}{\partial z} \right) - \ln z \frac{e^{-y}}{D_1} \frac{\partial D_1}{\partial y} L_1 \frac{\partial g}{\partial z} + e^y \frac{\partial}{\partial y} (e^{-2y} L_1 g). \quad (\text{A.4})$$

If the diffusion coefficient is of the form $D(p) = D_0 p^\epsilon$ (Eq. (4.2)) we can write the term $\frac{1}{D_1} \frac{\partial D_1}{\partial y} = \frac{d \log D_1}{d \log p} = \epsilon$. Inserting in Eq. (A.4):

$$\frac{\partial g}{\partial t} = \frac{u_1^2}{D_1} z^2 \frac{\partial^2 g}{\partial z^2} - \frac{z \ln z}{e^y} \epsilon L_1 \frac{\partial g}{\partial z} + e^y \frac{\partial}{\partial y} (e^{-2y} L_1 g). \quad (\text{A.5})$$

We find convenient to rescale the time variable to a significant time scale of the system, therefore we define $\tau_0 = D_1^*/u_1^2$ as the diffusion time upstream at the momentum p^* defined as in Chapter 4, Eq. (4.6) and Eq. (4.7). The new time variable is:

$$\hat{t} = \frac{t}{\tau_0}. \quad (\text{A.6})$$

Substituting t we finally get:

$$\frac{\partial g}{\partial \hat{t}} = \frac{D_1^*}{D_1} z^2 \frac{\partial^2 g}{\partial z^2} - \frac{D_1^*}{u_1^2} \frac{z \ln z}{e^y} \epsilon L_1 \frac{\partial g}{\partial z} + \frac{D_1^*}{u_1^2} e^y \frac{\partial}{\partial y} (e^{-2y} L_1 g). \quad (\text{A.7})$$

In order to solve the problem numerically the quantities need to be discretised in a triple grid in \hat{t} , z and y . We identify with the index n the time steps, with j those in space and with k the steps in momentum. In particular, j ranges from 0 to $J+1$ and by construction $z_0 = 0$ is the point at infinity and $z_{J+1} = 1$ represents the shock location.

We adopt an implicit scheme in \hat{t} , appropriate for a diffusive equation as the one we are dealing with. Thanks to such a choice the stability of the solution is guaranteed independently of the choice of the step size in time. The implicit scheme prescribes that we consider the space derivatives at the new time step rather than at the previous one at which the solution is already known:

$$\begin{aligned} \frac{g_{j,k}^{n+1} - g_{j,k}^n}{\Delta \hat{t}} &= \frac{D_1^*}{D_{1,k}} z_j^2 \left[\frac{g_{j+1,k}^{n+1} - 2g_{j,k}^{n+1} + g_{j-1,k}^{n+1}}{(\Delta z)^2} \right] - \frac{D_1^*}{u_1^2} \frac{z_j \ln z_j}{e^{y_k}} \epsilon L_{1,k} \left[\frac{g_{j+1,k}^{n+1} - g_{j,k}^{n+1}}{\Delta z} \right] + \\ &\quad \frac{D_1^*}{u_1^2} e^{y_k} \left[\frac{e^{-2y_{k+1}} L_{1,k+1} g_{j,k+1}^n - e^{-2y_k} L_{1,k} g_{j,k}^{n+1}}{\Delta y} \right]. \end{aligned} \quad (\text{A.8})$$

Multiplying both sides of the equation by $\Delta\hat{t}$ and rearranging the terms, we obtain:

$$g_{j,k}^{n+1} = g_{j,k}^n + \frac{D_1^*}{D_{1,k}} z_j^2 \frac{\Delta\hat{t}}{(\Delta z)^2} [g_{j+1,k}^{n+1} - 2g_{j,k}^{n+1} + g_{j-1,k}^{n+1}] - \frac{D_1^*}{u_1^2} \frac{z_j \ln z_j}{e^{y_k}} \epsilon L_{1,k} \frac{\Delta\hat{t}}{\Delta z} [g_{j+1,k}^{n+1} - g_{j,k}^{n+1}] + \frac{D_1^*}{u_1^2} e^{y_k} \frac{\Delta\hat{t}}{\Delta y} [e^{-2y_{k+1}} L_{1,k+1} g_{j,k+1}^n - e^{-2y_k} L_{1,k} g_{j,k}^{n+1}]. \quad (\text{A.9})$$

It is convenient to define the coefficients:

$$\alpha_{1,j,k} = \frac{D_1^*}{D_{1,k}} z_j^2 \frac{\Delta\hat{t}}{(\Delta z)^2}, \quad \beta_{1,j,k} = \frac{D_1^*}{u_1^2} \frac{z_j \ln z_j}{e^{y_k}} \epsilon L_{1,k} \frac{\Delta\hat{t}}{\Delta z}, \quad (\text{A.10})$$

$$\delta_k = \frac{D_1^*}{u_1^2} e^{y_k} \frac{\Delta\hat{t}}{\Delta y}.$$

We move on the lefthand side the terms at the time step $n + 1$ and leave on the righthand side those at the time step n , already known. Eq (A.9) now reads:

$$g_{j,k}^{n+1} - \alpha_{1,j,k} [g_{j+1,k}^{n+1} - 2g_{j,k}^{n+1} + g_{j-1,k}^{n+1}] + \beta_{1,j,k} [g_{j+1,k}^{n+1} - g_{j,k}^{n+1}] + \delta_k \frac{L_{1,k}}{e^{2y_k}} g_{j,k}^{n+1} = g_{j,k}^n + \delta_k \frac{L_{1,k+1}}{e^{2y_{k+1}}} g_{j,k+1}^n, \quad (\text{A.11})$$

that can be rewritten in the form:

$$a_{1,j,k} g_{j+1,k}^{n+1} + b_{1,j,k} g_{j,k}^{n+1} + c_{1,j,k} g_{j-1,k}^{n+1} = d_{1,j,k}, \quad (\text{A.12})$$

with:

$$\begin{cases} a_{1,j,k} = -\alpha_{1,j,k} + \beta_{1,j,k}, \\ b_{1,j,k} = 1 + 2\alpha_{1,j,k} - \beta_{1,j,k} + \delta_k \frac{L_{1,k}}{e^{2y_k}}, \\ c_{1,j,k} = -\alpha_{1,j,k}, \\ d_{1,j,k} = g_{j,k}^n + \delta_k \frac{L_{1,k+1}}{e^{2y_{k+1}}} g_{j,k+1}^n. \end{cases} \quad (\text{A.13})$$

Downstream

In the downstream region we define:

$$\begin{cases} z = \exp\left[-\frac{x}{l_L}\right] \\ y = \ln p, \end{cases} \quad (\text{A.14})$$

where $l_L = u_2 \tau_L = u_2 p / L_2(p)$. For clarity we carry on the calculation on the derivatives before inserting them into the transport equation:

$$\frac{\partial}{\partial x} = -\frac{1}{l_L} z \frac{\partial}{\partial z}$$

$$\frac{\partial}{\partial p} = -\frac{\ln z}{l_L} \frac{\partial l_L}{\partial p} z \frac{\partial}{\partial z} + e^{-y} \frac{\partial}{\partial y}, \quad (\text{A.15})$$

with:

$$\frac{\partial l_L}{\partial p} = l_L \left[\frac{1}{p} - \frac{1}{L_2} \frac{\partial L_2}{\partial p} \right]. \quad (\text{A.16})$$

We now operate the change of variables in Eq. (A.2):

$$\frac{\partial g}{\partial t} = \frac{u_2}{l_L} z \frac{\partial g}{\partial z} + \frac{D_2}{l_L^2} z \frac{\partial}{\partial z} \left(z \frac{\partial g}{\partial z} \right) - \frac{\ln z}{l_L} \frac{\partial l_L}{\partial p} L_2 z \frac{\partial g}{\partial z} + e^y \frac{\partial}{\partial y} (e^{-2y} L_2 g). \quad (\text{A.17})$$

With some more manipulation and substituting the expression for l_L , the equation results:

$$\frac{\partial g}{\partial t} = \frac{D_2}{u_2^2} \frac{L_2^2}{e^{2y}} z^2 \frac{\partial^2 g}{\partial z^2} + \frac{L_2}{e^y} \left[1 + \frac{D_2 L_2}{u_2^2 e^y} \right] z \frac{\partial g}{\partial z} - \frac{L_2}{e^y} z \ln z \left[1 - \frac{\partial \ln L_2}{\partial y} \right] \frac{\partial g}{\partial z} + e^y \frac{\partial}{\partial y} (e^{-2y} L_2 g). \quad (\text{A.18})$$

Again we change variable from t to \hat{t} defined in Eq. (A.6) and rewrite the above equation as:

$$\begin{aligned} \frac{\partial g}{\partial \hat{t}} &= \frac{D_1^* D_2}{u_1^2 u_2^2} \frac{L_2^2}{e^{2y}} z^2 \frac{\partial^2 g}{\partial z^2} + \frac{D_1^* L_2}{u_1^2 e^y} \left[1 + \frac{D_2 L_2}{u_2^2 e^y} \right] z \frac{\partial g}{\partial z} \\ &\quad - \frac{D_1^* L_2}{u_1^2 e^y} z \ln z \left[1 - \frac{\partial \ln L_2}{\partial y} \right] \frac{\partial g}{\partial z} + \frac{D_1^*}{u_1^2} e^y \frac{\partial}{\partial y} (e^{-2y} L_2 g). \end{aligned} \quad (\text{A.19})$$

Proceeding to discretisation, it results:

$$\begin{aligned} \frac{g_{j,k}^{n+1} - g_{j,k}^n}{\Delta \hat{t}} &= \frac{D_1^* D_{2,k}}{u_1^2 u_2^2} \frac{L_{2,k}^2}{e^{2y_k}} z_j^2 \left[\frac{g_{j+1,k}^{n+1} - 2g_{j,k}^{n+1} + g_{j-1,k}^{n+1}}{(\Delta z)^2} \right] + \frac{D_1^* L_{2,k}}{u_1^2 e^{y_k}} \left[1 + \frac{D_{2,k} L_{2,k}}{u_2^2 e^{y_k}} \right] \times \\ &\quad z_j \left[\frac{g_{j+1,k}^{n+1} - g_{j,k}^{n+1}}{\Delta z} \right] - \frac{D_1^* L_{2,k}}{u_1^2 e^{y_k}} z_j \ln z_j \left[1 - \frac{\ln L_{2,k+1} - \ln L_{2,k}}{\Delta y} \right] \left[\frac{g_{j+1,k}^{n+1} - g_{j,k}^{n+1}}{\Delta z} \right] + \\ &\quad \frac{D_1^*}{u_1^2} e^{y_k} \left[\frac{e^{-2y_{k+1}} L_{2,k+1} g_{j,k+1}^n - e^{-2y_k} L_{2,k} g_{j,k}^{n+1}}{\Delta y} \right]. \end{aligned} \quad (\text{A.20})$$

We multiply both sides of the equation by $\Delta \hat{t}$ and define the coefficients:

$$\begin{aligned} \alpha_{2,j,k} &= \frac{D_1^* D_{2,k}}{u_1^2 u_2^2} \frac{L_{2,k}^2}{e^{2y_k}} z_j^2 \frac{\Delta \hat{t}}{(\Delta z)^2}, & \beta_{2,j,k} &= \frac{D_1^* L_{2,k}}{u_1^2 e^{y_k}} z_j \ln z_j \frac{\Delta \hat{t}}{\Delta z} \left[1 - \frac{\ln L_{2,k+1} - \ln L_{2,k}}{\Delta y} \right], \\ \gamma_{2,j,k} &= \frac{D_1^* L_{2,k}}{u_1^2 e^{y_k}} z_j \frac{\Delta \hat{t}}{\Delta z} \left[1 + \frac{D_{2,k} L_{2,k}}{u_2^2 e^{y_k}} \right], & \delta_k &= \frac{D_1^*}{u_1^2} e^{y_k} \frac{\Delta \hat{t}}{\Delta y}. \end{aligned} \quad (\text{A.21})$$

Rearranging the terms, the equation is reduced again to the form:

$$a_{2,j,k} g_{j+1,k}^{n+1} + b_{2,j,k} g_{j,k}^{n+1} + c_{2,j,k} g_{j-1,k}^{n+1} = d_{2,j,k}, \quad (\text{A.22})$$

where:

$$\begin{cases} a2_{j,k} = -\alpha2_{j,k} + \beta2_{j,k} - \gamma2_{j,k} , \\ b2_{j,k} = 1 + 2\alpha2_{j,k} - \beta2_{j,k} + \gamma2_{j,k} + \delta_k \frac{L_{2,k}}{e^{2y_k}} , \\ c2_{j,k} = -\alpha2_{j,k} , \\ d2_{j,k} = g_{j,k}^n + \delta_k \frac{L_{2,k+1}}{e^{2y_{k+1}}} g_{j,k+1}^n . \end{cases} \quad (\text{A.23})$$

Instead of directly solving the tridiagonal matrix resulting from Eq. (A.22), we approach the problem in a numerically less costly way: we put an ansatz on the form of g and write it at every step as:

$$g_j^n = H_{j,k} g_{j+1}^n + K_{j,k}. \quad (\text{A.24})$$

It has to be noted that H and K also depend on time, but since they always appear in the equations at the same time step, we can keep this dependence implicit in terms of indices to have a lighter formalism. Substituting Eq. (A.24) into Eq. (A.22), once for g_j and twice for g_{j-1} , we obtain:

$$a2_{j,k} g_{j+1}^{n+1} + b2_{j,k}(j) [H_{j,k} g_{j+1}^{n+1} + K_{j,k}] + c2_{j,k}(j) H_{j-1} [H_{j,k} g_{j+1}^{n+1} + K_{j,k}] + c2_{j,k}(j) K_{j-1} = d2_{j,k}(j), \quad (\text{A.25})$$

which reduces to:

$$[a2_{j,k} + b2_{j,k}(j) H_{j,k} + c2_{j,k}(j) H_{j,k} H_{j-1}] g_{j+1}^{n+1} + [b2_{j,k}(j) + c2_{j,k}(j) H_{j-1}] K_{j,k} = d2_{j,k}(j) - c2_{j,k}(j) K_{j-1}. \quad (\text{A.26})$$

For the above relation to be always true we need to satisfy at the same time both the conditions:

$$\begin{aligned} a2_{j,k} + b2_{j,k}(j) H_{j,k} + c2_{j,k}(j) H_{j,k} H_{j-1} &= 0, \\ [b2_{j,k}(j) + c2_{j,k}(j) H_{j-1}] K_{j,k} &= d2_{j,k}(j) - c2_{j,k}(j) K_{j-1}, \end{aligned} \quad (\text{A.27})$$

giving:

$$\begin{aligned} H_{j,k} &= -\frac{a2_{j,k}}{b2_{j,k}(j) + c2_{j,k}(j) H_{j-1}}, \\ K_{j,k} &= \frac{d2_{j,k}(j) - c2_{j,k}(j) K_{j-1}}{b2_{j,k}(j) + c2_{j,k}(j) H_{j-1}}. \end{aligned} \quad (\text{A.28})$$

At every time step we can evaluate all the H and K coefficients once we know H_0 and K_0 which are obtained from the boundary conditions at infinity. As discussed in Chapter 4, such boundaries are $f(|\infty|, p) = 0$, both up and downstream. Therefore $H_0 = 0$, $K_0 = 0$. Once obtained H and K for every j from 0 to J (i.e. from $\pm\infty$ to 0 in x), we can calculate the value of g backwards from the shock to infinity, using the boundary condition at the shock: $g_{J+1,k} = g(0, p)$ for every n . Such boundary is given by Eq. (4.4). Once again we pass from $f(x, p)$ to $g(x, p) = p^4 f(x, p)$. Recalling that $Q = Q_0 \delta(p - p_0)$, the boundary condition reads:

$$p \frac{\partial g_0}{\partial p} = 4g_0 + \frac{3}{u_2(r-1)} \left[D_2(p) \frac{\partial g}{\partial x} \Big|_2 - D_1(p) \frac{\partial g}{\partial x} \Big|_1 + Q_0 \delta(p - p_0) p^4 \right]. \quad (\text{A.29})$$

Changing variables from (x, p) to (z, y) defined as in Eq. (A.3) and (A.14), we obtain the expression:

$$\frac{\partial g_0}{\partial y} = 4g_0 - \frac{3D_2 L_2}{u_2^2(r-1)e^{y_2}} z \frac{\partial g}{\partial z} \Big|_2 - \frac{3r}{r-1} z \frac{\partial g}{\partial z} \Big|_1 + \tilde{Q}_0. \quad (\text{A.30})$$

We proceed now to discretise the equation to solve it numerically. Since the injection term is non-zero only for $p = p_0$, it can be written as:

$$Q = \begin{cases} 0 & \forall k \neq 0 \\ \tilde{Q}_0 & k = 0. \end{cases}$$

We therefore remove this term from the equation and then put it as a boundary on $g(p_0)$. The Eq. (A.30) becomes:

$$\frac{g_{J+1}^k - g_{J+1}^{k-1}}{\Delta y} = 4g_{J+1}^k - \frac{3D_{2,k} L_{2,k}}{u_2^2(r-1)e^{y_k}} z_{J+1} \frac{g_{J+1}^k - g_{2,J}^k}{\Delta z} - \frac{3r}{r-1} z_{J+1} \frac{g_{J+1}^k - g_{1,J}^k}{\Delta z}, \quad (\text{A.31})$$

where we adopt an explicit scheme in p , no diffusion. By construction:

$$z_{J+1} = 1$$

and

$$\begin{cases} g_{1,J}^k = H_{1,J} g_{J+1}^k + K_{1,J} \\ g_{2,J}^k = H_{2,J} g_{J+1}^k + K_{2,J} \end{cases}$$

Plugging these expressions in Eq. (A.31) and after some manipulation, the equation for g_{J+1}^k reads:

$$g_{J+1}^k \left[1 - 4\Delta y + \frac{3D_{2,k}L_{2,k}}{u_2^2(r-1)e^{y_k}} \frac{\Delta y}{\Delta z} (1 - H_{2,J}) + \frac{3r}{r-1} \frac{\Delta y}{\Delta z} (1 - H_{1,J}) \right] = g_{J+1}^{k-1} + \frac{3}{r-1} \frac{\Delta y}{\Delta z} \left[\frac{D_{2,k}L_{2,k}}{u_2^2 e^{y_k}} K_{2,J} + rK_{1,J} \right]. \quad (\text{A.32})$$

Renaming B the parenthesis on the lefthand side, we simply obtain:

$$g_{J+1}^k = \frac{g_{J+1}^{k-1}}{B} + \frac{3}{r-1} \frac{\Delta y}{\Delta z} \frac{(K_{2,J} + rK_{1,J})}{B}. \quad (\text{A.33})$$

The equation is solved with the condition $g_{J+1}^0 = \tilde{Q}_0/\Delta y$.

Once we have the value of g_{J+1} for every p , we can reconstruct back the space dependence from the shock to infinity by means of Eq. (A.24), therefore obtaining the complete expression for the distribution function at every time step.

Bibliography

- Aharonian, F.A. 2004, *Very High Energy Cosmic Gamma Radiation*, World Scientific Publishing
- Aharonian, F., Akhperjanian, A., Barrio, J. 2001, *A&A*, 370, 112
- Aharonian, F.A., Akhperjanian, A.G., Aye, K.M. et al. 2004, *Nature*, 432, 75
- Aharonian, F.A., Akhperjanian, A.G., Aye, K.M. et al. 2005, *Science*, 309, 746
- Aharonian, F.A., Akhperjanian, A.G., Aye, K.M. et al. 2006a, *A&A*, 449, 223
- Aharonian, F.A., Akhperjanian, A.G., Aye, K.M. et al. 2006b, *A&A*, 460, 43
- Aharonian, F.A., Akhperjanian, A.G., Aye, K.M. et al. 2006c, *Nature*, 440, 1018
- Albert, J., Aliu, E., Anderhub, H. et al. 2006, *Science*, 312, 1771
- Albert, J., Aliu, E., Anderhub, H. et al. 2007a, *A&A*, 474, 937
- Albert, J., Aliu, E., Anderhub, H. et al. 2007b, *ApJ*, 665, 51
- Allen, G.E., Keohane, J.W., Gotthelf, E.V. 1997, *ApJ*, 487, 97
- Armstrong, J.W., Rickett, B.J., Spangler, S.R. 1995, *ApJ*, 443, 209
- Axford, W.I., Leer, E., Skadron, G. 1977, *ICRC Proceedings*, 11, 132
- Baars, J.W.M., Genzel, R., Pauliny-Toth, I.I.K., Witzel, A. 1977, *A&A*, 61, 99
- Bamba, A., Yamazaki, R., Ueno, M., Koyama, K. 2003, *ApJ*, 589, 827

Bamba, A., Yamazaki, R., Yoshida, T., Terasawa, T., Koyama, K. 2005, *ApJ*, 621, 793

Bell, A.R., 1978, *MNRAS*, 182, 147

Berezhko, E.G., Ellison, D.C. 1999, *ApJ*, 526, 385

Berezhko, E.G., Völk, H.J. 2004, *A&A*, 419, 27

Berezinsky, V.S., Grigoreva, S.I. 1988, *A&A*, 199, 1

Berezinsky, V., Blasi, P., Ptuskin, V.S. 1997, *ApJ*, 487, 529

Berezinsky, V., Gazizov, A.Z., Grigorieva, S.I. 2005, *Phys. Lett. B*, 612, 147

Bertschinger, E 1985, *ApJ Suppl.*, 58, 39

Bethe, H.; Heitler, W. 1934, *Roy. Soc. Lon. Proceedings S. A*, 146, 83

Blandford, R.D., Ostriker, J.P. 1978, *ApJ*, 221, 29

Blasi, P. 2002, *Astrop. Ph.*, 16, 429

Blasi, P., Gabici, S., Brunetti, G. 2007, *Int. J. of Modern Phys. A*, 22, 681

Blumenthal, G.R. 1970, *Phys. Rev. D*, 1, 1596

Blumenthal, G.R., Gould, R.J. 1970, *Rev. Mod. Phys.*, 42, 237

Borgani, S., Guzzo, L. 2001, *Nature*, 409, 39

Bosch-Ramon, V., Khangulyan, D. 2008, [arXiv:astro-ph/0805.4123v2](https://arxiv.org/abs/0805.4123v2)

Bulanov, S.V., Dogiel, V.A. 1979, *Sov. Astron. Lett.*, 5, 278

Caprioli, D., Blasi, P., Amato, E., Vietri, M. 2008, [arXiv:astro-ph/0807.4261v1](https://arxiv.org/abs/0807.4261v1)

Carilli, C.L., Taylor, G.B. 2002, *ApJ*, 577, 22

Casares, J., Ribó, M., Ribas, I., Paredes, J.M., Martí, J., Herrero, A. 2005, *MNRAS*, 364, 899

- Cassam-Chenaï, G., Decourchelle, A., Ballet, J., Hwang, U., Hughes, J.P., Petre, R. 2004, *A&A*, 414, 545
- Chodorowski, M.J., Zdziarski, A.A., Sikora, M. 1992, *ApJ*, 400, 181
- Clark, N., Tadhunter, C. 1997, *Greenbank Workshop Proceedings*, 15
- Colafrancesco, S., Blasi, P. 1998, *Astrop. Ph.*, 9, 227
- Crusius, A., Schlickeiser, R. 1986 *A&A*, 164, L16
- Davidson, J.A., Werner, M.W., Wu, X., Lester, D.F., Harvey, P.M., Joy, M., Morris, M. 1992, *ApJ*, 387, 189
- Decourchelle, A., Sauvageot, J.L., Audard, M., Aschenbach, B., Sembay, S., Rothenflug, R., Ballet, J., Stadlbauer, T., West, R.G. 2001, *A&A*, 365, 218
- Dickel, J.R., van Breugel, W.J.M., Strom, R.G. 1991, *Astron. J.*, 101, 2151
- Dressler, A. 1980, *ApJ Suppl.*, 42, 565
- Drury L.O'C. 1983, *Rep. on Prog. in Phys.*, 46, 973
- Drury, L. O'C., Völk, H. J. 1981, *ApJ*, 248, 344
- Drury, L.O'C., Duffy, P., Eichler, D., Mastichiadis, A. 1999, *A&A*, 347, 370
- Ellison, D.C., Slane, P., Gaensler, B.M. 2001, *ApJ*, 563, 191
- Enomoto, R., Tanimori, T., Naito, T. et al. 2002, *Nature*, 416, 823
- Enßlin, T., Vogt, C., Pfrommer, C. 2005, *The Magnetized Plasma in Galaxy Evolution, Conf. Proceedings*
- Favata, F., Vink, J., dal Fiume, D., Parmar, A.N., Santangelo, A., Mineo, T., Preite-Martinez, A., Kaastra, J.S., Bleeker, J.A.M. 1997 *A&A*, 324, 49
- Fermi, E., 1949, *Phys. Rev.*, 75, 1169

- Forman, W., Jones, C., Markevitch, M., Vikhlinin, A., Churazov, E. 2002, Lighthouses of the Universe: The Most Luminous Celestial Objects and Their Use for Cosmology, Conf. Proceedings
- Fusco-Femiano, R., dal Fiume, D., Feretti, L., Giovannini, G., Grandi, P., Matt, G., Molendi, S., Santangelo, A. 1999, ApJ, 513, 21
- Gabici, S., Blasi, P. 2003, Astrop. Ph., 19, 679
- Gaisser, T. K. 1990, *Cosmic Rays and Particle Physics*, Cambridge University Press
- Ginzburg, V.L., Syrovatskii, S.I. 1964, *The Origin of Cosmic Rays*, Pergamon Press
- Govoni, F., Feretti, L. 2004, Int. J. Modern Phys. D, 13, 1549
- Green D.A. 2006, "A Catalogue of Galactic Supernova Remnants (2006 April version)", Cambridge, Mullard Radio Astr. Obs. (available at "<http://www.mrao.cam.ac.uk/surveys/snrs/>").
- Heavens, A.F., Meisenheimer, K. 1987, MNRAS, 225, 335
- Heiles, C. 1976, ARA&A, 14, 1
- Hillas, A.M. 1984, ARA&A, 22, 425
- Hinton, J.A., Aharonian, F.A. 2007, ApJ, 657, 302
- Hwang, U., Decourchelle, A., Holt, S.S., Petre, R. 2002, ApJ, 581, 1101
- Inoue, S., Aharonian, F.A., Sugiyama, N. 2005, ApJ, 628, 9
- Jones, F.C. 1968, Phys. Rev., 167, 1159
- Jones, F.C., Ellison, D.C. 1991, Space Science Rev., 58,259
- Kang, H., Cen, R., Ostriker, J.P., Ryu, D. 1994, ApJ, 428, 1
- Kang, H., Ryu, D., Jones, T.W. 1996, ApJ, 456, 422
- Kang, H., Rachen, J.P., Biermann, P.L. 1997, MNRAS, 286, 257

- Kelner, S.R., Aharonian, F.A. 2008, arXiv:astro-ph/0803.0688v2
- Khangulyan, D., Aharonian, F. 2005, AIP Conf. Proceedings, 745, 359
- Khangulyan, D., Aharonian, F.A., Bosch-Ramon, V. 2008, MNRAS, 383, 467
- Kirk, J.G. 2001, ICRC Proceedings, 6, 2043
- Kirshner, R., Winkler, P.F., Chevalier, R.A. 1987, ApJ, 315, 135
- Klein, O., Nishina, T. 1929, Zeitschrift für Physik, 52, 853
- Koyama, K., Petre, R., Gotthelf, E.V., Hwang, U., Matsuura, M., Ozaki, M., Holt, S.S. 1995, Nature, 378, 255
- Koyama, K., Kinugasa, K., Matsuzaki, K., Nishiuchi, M., Sugizaki, M., Torii, K., Yamauchi, S., Aschenbach, B. 1997, Publ. Astron. Soc. Japan, 49, 7
- Kraft, R.P., Vazquez, S.E., Forman, W.R., Jones, C., Murray, S.S., Hardcastle, M.J., Worrall, D.M., Churazov, E. 2003, ApJ, 592, 129
- Krall, N.A., Trivelpiece, A.W. 1973, *Principles of Plasma Physics*, MacGraw-Hill
- Krymsky, G.F. 1977, Soviet Physics-Doklady, 234, 1306
- Kulsrud, R.M., Zweibel, E.G. 2008, Rep. Prog. Phys., 71, 6901
- Landau, L.D., Lifshitz, E.M. 1959, *Course of Theoretical Physics; Fluid Mechanics*, Pergamon Press
- Lagage, P.O., Cesarsky, C.J. 1983a, A&A 118, 223
- Lagage, P.O., Cesarsky, C.J. 1983b, A&A 125, 249
- Laming, J.M., Hwang, U. 2003, ApJ, 597, 347
- Lee, M.A. 1982, J. Geophys. Rev., 87, 5063
- Loeb, A., Waxman, E. 2000, Nature, 405, 156

- Longair, M.S. 1997, *High Energy Astrophysics*, Cambridge University Press
- Lucek, S.G., Bell, A.R. 2000, MNRAS, 314, 65
- Malkov, M. A. 1997, ApJ, 485, 638
- Malkov, M.A., Drury L.O'C. 2001, Rep. Prog. Phys., 64, 429
- Mathis, J.S., Mezger, P.G., Panagia, N. 1983, A&A, 128, 212
- Mirabel, I.F., Rodriguez, L.F. 1999, ARA&A, 37, 409
- Mücke, A., Engel, R., Rachen, J.P., Protheroe, R.J., Stanev, T. 2000, Comp. Phys. Comm., 124, 290
- Ness, N.F., Searce, C.S., Seek, J.B. 1964, J. Geophys. Rev., 69, 3531
- Norman, C.A., Melrose, D.B., Achterberg, A. 1995, ApJ, 454, 60
- Peebles, P.J.E. 1980, *The Large-scale Structure of the Universe*, Princeton Univ. Press
- Pierre Auger Collaboration 2007, Science, 318, 938
- Protheroe, R.J. 2004, Astrop. Ph., 21, 415
- Rybicki, G. B., Lightman, A. P. 1979, *Radiative Processes in Astrophysics*, Wiley
- Sarazin, C.L. 1988, "X-ray Emission from Clusters of Galaxies", Cambridge University Press, i-x,1-252
- Schlickeiser, R. 2002, *Cosmic Ray Astrophysics*, Springer
- Shu, F.H. 1992, *The Physics of Astrophysics; Gas Dynamics*, University Science Books
- Skilling, J. 1975, MNRAS, 172, 557
- Slane, P., Gaensler, B.M., Dame, T.M., Hughes, J.P., Plucinsky, P.P., Green, A. 1999, ApJ, 525, 357

- Sreekumar, P., Bertsch, D.L., Dingus, B. L. et al., 1998, ApJ, 494, 523
- Stecker, F.W. 1968, Phys. Rev. Lett., 21, 1016
- Swordy, S.P. 2001, Space Science Rev., 99, 85
- Swordy, S.P., Mueller, D., Meyer, P., L'Heureux, J., Grunsfeld, J. M. 1990 ApJ, 349, 625
- Uchiyama, Y., Aharonian, F.A., Tanaka, T., Takahashi, T., Maeda, Y. 2007, Nature, 449, 576
- Vallée, J. P. 2004, New Astr. Rev., 48, 763
- Vannoni, G., Gabici, S., Aharonian, F.A. 2008, arXiv:astro-ph/0803.1138v1
- Vannoni, G., Aharonian, F.A., Gabici, S., Kelner, S.R., Prosekin A. in preparation
- Vietri, M. 2006, *Astrofisica delle Alte Energie*, Bollati Boringhieri
- Vink, J. 2008, arXiv:astro-ph/0803.4011v1
- Vink, J., Laming, J.M. 2003, ApJ, 584, 758
- Völk, H.J., Aharonian, F.A., Breitschwerdt, D. 1996, Space Science Rev., 75, 279
- Warren, J.S., Hughes, J.P., Badenes, C., Ghavamian, P., McKee, C.F., Moffett, D., Plucinsky, P.P., Rakowski, C., Reynoso, E., Slane, P. 2005, ApJ, 634, 376
- Webb, G.M., Drury, L.O'C., Biermann, P. 1984, A&A, 137, 185
- Wentzel, D.G., 1974, ARA&A, 12, 71
- Widrow, L.M. 2002, Rev. Mod. Phys., 74, 775.
- Zirakashvili, V.N., Aharonian, F.A. 2007, A&A, 465, 695

Acknowledgements

First of all I would like to thank my supervisor Prof. Felix Aharonian for the great opportunity of these three years of work together, for the incredible amount of things I could learn from him, for those that I managed to and also for the many more still left to learn.

I also thank Dr. Stefano Gabici. Stefano, you know that none of this would have been possible without you. You'll make a wonderful group leader and teacher one day and I really wish you it will be soon (I think I contributed the maximum I could to your CV!). It will be weird, after 5 years, without you.

I would like to thank Prof. Werner Hofmann for accepting to be my referee and as director of the Division of Particle Physics and Astroparticle Physics at the Max-Planck-Institute für Kernphysik, one of the best places to be in our field.

I would like to thank also Prof. Matthias Bartelmann and Dr. Christian Fendt for being in my committee, and for the patience!

I acknowledge support from the International Max-Planck Research School (IMPRS) Heidelberg. I would like to thank especially Christian for the amazing job he did with us, thank you!

I would like to thank Dr. Zirakashvili and Prof. Kelner. A due and sincere thank you to my group for teaching me how a bunch of passionate scientists becomes a unity. It's been great to be around you, guys. A special thank to Andrew Taylor, Mitya Khangulyan and Valenti Bosch-Ramon for constant help and support. Together with my group it is my pleasure to thank Prof. Völk, Prof. Kirk (thank you for all the help), Prof. Tuffs, Dr. Resconi and all their groups for providing an incredibly stimulating scientific environment and a pleasant place to work. I am grateful for the opportunity of working with such brilliant physicists. I believe that all "our corridor" is indeed quite a special place...

Cara mamma, caro babbo, c'è stato un tempo in cui ho creduto di aver fatto l'errore più grande della mia vita a venire qui e a non essere con voi nel momento più difficile che abbiamo mai vissuto. Grazie per non avermi fatto desistere e per l'infinito appoggio che mi date sempre.

There are four people I would have never survived this PhD without and I'll take a minute to thank them personally.

Claudia, "I'm your sister, I'm your daughter"... We've shared the Heidelberg spleen, the Heidelberg blues... the Heidelberg jazz, for what matters! Don't even

make me start or I'd need a hundred more pages. But I guess a thank you will do. We'll still walk together sulla strada del destille.

Giovi, my sunshine, for all that you're quiet and shy, no one is able to make me laugh like you do about everything. In my dark moments, and you know if I have of those, I would always turn to you. Thanks. Oh, and watch out for the patterns!

Probably the one I learnt more about myself from is you, Isabel. We can be so different and yet just the same. I would have never imagined not to have you by my side in this last part of... the thing! still you are here and will always be.

My little sabbath got completed when Viviana joined us, giving me a safe corner to hide in. You've always given me your time, even when you didn't have it and I was honestly unbearable!

Girls, you know that I expect you to take me for the "Grand Tour" now, right?!

And since special friends always come to me in groups of four, I'd like to thank here Guia, Laura, Maura and Scilla (alphabetical order, no other being possible!) for taking the time to come here and understand what this was all about. Being far from you has clearly shown how close we'll always be. A great thank to all my friends in Florence for never giving up on me. And of course I acknowledge here the support of "Gruppospacca"!

A great thank you to all the gang of amazing friends I managed to meet: Matteo and Ale above all, Brian (thanks man, you're great!), Olga, Giovanni, and all the others. It's been simply fantastic. Dan, Anan, we still have to do that volcano thing. Thanks to you and all the "bio bunch" for the crazyness. My dearest, "il Listone"! I will never thank you enough for these years together and for reassuring me of the fact that the best part of Italy is safely living abroad! I can't name you all and it's a shame, but it makes me feel grateful to think how many wonderful people I've met! Clearly, I'm including in the best part of Italy all the French, and in "the French" the Japanese and Scots! Anna, Julien and Jerome, I have to thank you especially for being just like you are. To all the IMPRS fellows, it's been fun, keep on fighting for a better system. And guys, the "first generation", it's been great to share these years with you (...will I get my farewell present?!).

Many people have come and gone in HD and in my life in these few years, more than you'd expect in a lifetime! They've all taken something and left me a lot. It's unbelievable how somebody you barely know can change your world. So, thank you all. Speaking of which... guys you there, my "neutrino friends", I'm talking to you. You're one of the best things that these years left me. And, man, if you changed my life! Look where I'll be next.

I've gone through the toughest years of my life in Heidelberg and I hated this place... all to realise one day I was exactly where I wanted to be. I'll miss these crazy years. I feel home now, and this is what I thank you all for.

But it seems I've become some sort of gypsy so now it's time to move on, to the next stop of the journey.

Amore mio, here we are finally. And we're still here. We promised each other we would be stronger than anything else. Only you know how tough it was. But we have been. I can't wait for Paris! with you.